PHD THESIS

Phase Diagram of a Correlated *d*-electron System: Experimental Study of $BaVS_3$

István Kézsmárki

Supervisor: Prof. György Mihály

Budapest University of Technology and Economics
Institute of Physics
Department of Physics

BUTE
2003

Contents

Chapter 1

Introduction

The present work investigates the "magnetic field – pressure – temperature" phase diagram of a vanadium based correlated d-electron compound, the BaVS$_3$.

The effect of strong electron-electron interaction, which leads to a tendency towards the formation of various broken symmetry ground states, has been a central problem of the solid state physics in the last half century. Our transport and optical studies have demonstrated that electron correlations play a crucial role in each phase of BaVS$_3$. The correlations are not extremely strong, rather, U/t is close to unity (where U and t are the usual parameters of the Hubbard model).

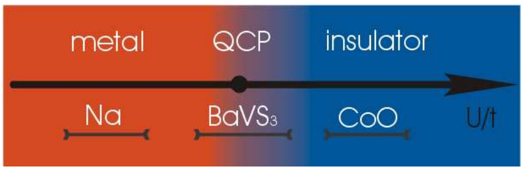

Figure 1.1: *The relative strength of electron correlation in BaVS$_3$ is on intermediate scale between normal metals and large gap insulators.*

At ambient pressure this material undergoes a metal to insulator transition at $T_{MI} = 70\,\mathrm{K}$. Although its onset has been known for almost three decades, the driving force of the transition and the nature of the neighbouring phases have not been clarified yet. We have determined the "magnetic field–temperature" phase boundary by magnetotransport experiments and shown that the transition is of second order. We have proposed a mechanism in which the transition from the high-temperature paramagnetic metal to the singlet insulator is induced by orbital ordering and the order parameter of the phase transition is the spin gap.

The metal-insulator transition is highly sensitive to the applied hydrostatic pressure and the insulating phase can be completely suppressed at $p = 22.5\,\mathrm{kbar}$ as we observed both by means of dc transport and optical conductivity experiments. The pressure induced low-temperature metallic state is a non-Fermi liquid, the electron-electron scattering is largely enhanced by quantum fluctuations. Such a quantum critical behaviour has been known to be present both in weakly ferromagnetic and antiferromagnetic materials but has not been reported for singlet insulators so far.

Finally, we have explored the complete “magnetic field–pressure–temperature” phase boundary between the paramagnetic metal and the singlet insulator.

Chapter 2

Overview of experimental studies and related models

2.1 Crystal structure and symmetry

At room temperature $\mathrm{BaVS_3}$ has a hexagonal crystal structure [1] with space group $P6_3/mmc$ and two formula units per unit cell. The valence state of the components are Ba^{2+}, V^{4+} and S^{2-}. Such crystalline structure assumes only one crystallographic position of vanadium atoms: each of them is surrounded by six sulfur atoms forming $\mathrm{VS_6}$ octahedron elongated in the c direction. (In case of perfect octahedra we would have a perovskit structure.) Along the c-axis linear chains are built up of face sharing octahedra while in the perpendicular plane these chains are organized into a triangular lattice. The crystal structure is suggestive of a quasi-one-dimensional compound. Due to the barium spacers, in the $a-b$ plane the interchain vanadium-vanadium separation, $l_{inter} = 6.73\,\text{Å}$ is three times larger than their intrachain bondlength, $l_{intra} = 2.81\,\text{Å}$ which is near to the lattice constant of the metallic vanadium. The crystal structure of the high-temperature hexagonal phase is shown in Fig. 2.1.

At $T_s = 250\,\mathrm{K}$ $\mathrm{BaVS_3}$ undergoes a structural phase transition which reduces further the crystal symmetry to orthorhombic with space group $Cmc2_1$ [2, 3] and still two formula units per unit cell. At this transition the dynamical distortion of the vanadium atoms freezes out and a static order of the vanadium sublattice

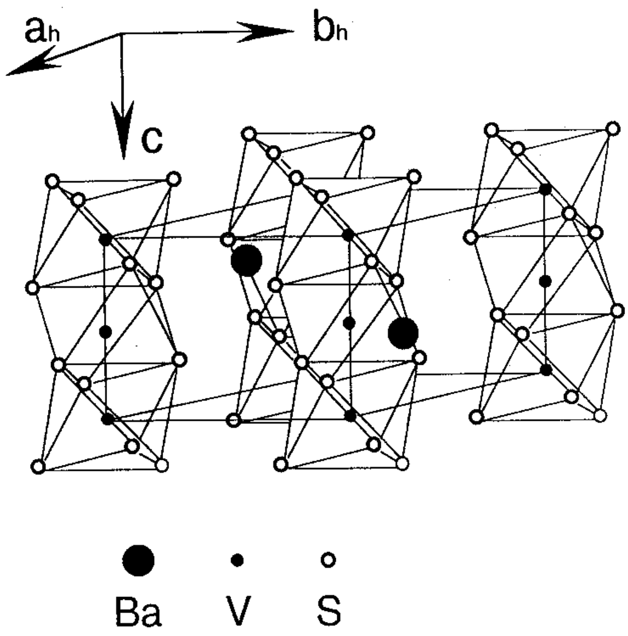

Figure 2.1: *Crystal structure of BaVS$_3$. Sulfur octahedra are bound into face sharing chains running along the c-axis and form triangular lattice in the $a-b$ plane.*

appears in such a way that they remain equally spaced along the c-axis but the chains become zigzag. Although this distortion (visualized in the last stage of Fig. 2.3) gradually increases with decreasing temperature and seems to saturate only below $\sim 20\,\mathrm{K}$ the crystal symmetry remains the same all the way down in temperature. The temperature dependence of the lattice parameters in the plane perpendicular to the chains, **a** and **b** are studied by x-ray scattering. The size of the orthorhombic distortion is reflected in a difference between **a** and $\mathbf{b}/\sqrt{3}$ which develops below T_s since in the hexagonal phase they are equal by definition (see Fig. 2.2).

2.2 Phase transitions of the system

BaVS$_3$ goes through successively three phase transitions below room temperature: a structural transition occuring at $T_s = 250\,\mathrm{K}$, a metal to insulator transition at

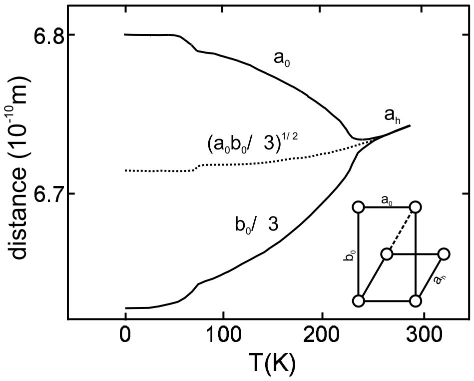

Figure 2.2: *Temperature dependence of the $a - b$ plane lattice parameters from Ref. [3]. Orthorhombic distortion appears at $T_s = 250\,K$, raises with cooling down and shows a sharp change at $T_{MI} = 70\,K$.*

$T_{MI} = 70\,\mathrm{K}$ and a third transition at $T_x = 30\,\mathrm{K}$ thought to be associated with magnetic and orbital order.

We just had an insight (in section 2.1) into the crystal symmetry of the system in the different phases. The only noticeable aspect of the $T_s = 250\,\mathrm{K}$ transition has not been mentioned yet that beyond the structure identifying methods the only property in which it is manifested is the resistivity. There is a slight change in the slope of the $R(T)$ curve at that temperature.

Now we turn to the metal-insulator transition. In sense of transport properties the high-temperature phase ($T > T_{MI}$) of the material is metallic: both resistivity and thermoelectric power are decreasing towards lower temperatures. However, the resistivity is quite high (close to the Ioffe-Regel limit[1]) and shows an upturn below $T_{min} = 140\,\mathrm{K}$. In contrast to the electronic transport, the Curie-Weiss type magnetic susceptibility, $\chi = C/(T - \Theta)$ rather indicates the charge carriers being localized.[2] The effective moment, $p_{eff} \approx 1.4\,\mu_{Bohr}$ is smaller than $1.73\,\mu_{Bohr}$ which would correspond to a spin-$\frac{1}{2}$ sitting at each vanadium site.

The sharp cusp in the magnetic susceptibility gives the clearest evidence for the transition happening at $T_{MI} = 70\,\mathrm{K}$. The continuous decrease of susceptibility in

---

[1] When the mean free path is in the range of the lattice constant.

[2] $C = \frac{N}{V}\frac{p_{eff}^2\mu_{Bohr}^2}{3k_B}$ is the Curie constant, where $p_{eff} = g\sqrt{S(S+1)}$ and Θ is the Weiss temperature which is close to zero varying in the range of $10 - 40\,\mathrm{K}$ from experiment to experiment.

the low-temperature phase suggests the freezing out of the spin degrees of freedom. Further anomalies are observed in two other thermodynamic properties: specific heat shows a discontinuity and thermal expansion coefficient has remarkable peak at the same temperature. Concerning the transport properties this phenomenon is a metal to insulator transition. The logarithmic derivative of the resistivity shows a sharp peak while the thermoelectric power changes sign at 70 K and both of them go through a dramatic increase below it.

Inside of the insulating phase, at $T_x = 30\,\mathrm{K}$ neutron scattering and diffraction experiments suggest the onset of a magnetic transition. The observed increase of inelastic scattering intensity below 30 K indicates the presence of a hyperfine field while the appearance of new magnetic Bragg peaks directly reveals an antiferromagnetic order with a propagation vector of $Q = (0.226, 0.226, 0)$ and with an ordered magnetic moment $\sim 0.5\,\mu_{Bohr}$. (The propagation vector is expressed in the hexagonal index.) In ^{51}V nuclear quadruple resonance (NQR) measurements the inverse of the spin-spin relaxation time, $1/T_2$ (proportional to the integrated susceptibility) was found to diverge at T_x. The quadruple resonance spectra was explained in terms of huge and extraordinary asymmetric electrical field gradient (EFG) developing at the V sites below T_x. Since vanadium is embedded in an octahedral configuration of the neighbouring sulfurs, the EFG cannot be attributed to the environment but it probably comes from the non-spherical charge distribution of the vanadium $3d$ wavefunctions. This is an indirect evidence of the presence of orbital order in the ground state of $\mathrm{BaVS_3}$.

A detailed list of experiments detecting either of these transitions is given in Table 2.1. In those cases when large number of the possible references is available just the three reliable ones are quoted.

2.3 Vanadium ion in orthorhombic crystal field

Except of V^{4+} which has a single electron on its $3d$ levels the other components have fulfilled electron shells. In the picture of perfect charge transfer, i.e. in the lack of hybridization between bands of the different ions, this single d electron of vanadium is responsible for electrical and magnetic properties of $\mathrm{BaVS_3}$. Thus, at first we focus our attention to the crystal field splitting of $3d$ levels.

Table 2.1:

	Structure		Magnetic prop.			Transport prop.			Thermal prop.	
	X-ray	Neutron diffr.	Susceptibility	NMR/ NQR	Neutron scatt.	Resistivity	IR spect.	Thermopower	Specific heat	Thermal expansion
T_s	[1, 3]	[2]				[11, 21]				
T_{MI}	[3]		[10, 11, 21]	[8]		[11, 21, 22]	[37]	[38, 39]	[20]	[11]
T_x			[21]	[8]	[9, 15]					

In isotropic space d shell is 5 fold degenerated which splits in an octahedral environment to a low lying 3 fold degenerated $t_{2g}(xy, xz, yz)$ level and a $e_g(3z^2 - r^2, x^2 - y^2)$ doublet at higher energy. (The x, y, z axes point to the corners of the octahedron with negative sulfur ions sitting there.[3] Thus t_{2g} orbitals with smaller overlapping are energetically favourable.) From now on, in the discussion of the three lowest orbitals we choose another coordinate system which matches better to the crystal structure. The new axes are parallel with the main crystallographic directions (labelled as a, b and c in Fig. 2.1): z points along the trigonal axis and x, y lie in the perpendicular plane. After rotating the coordinate system, the three lowest energy wavefunctions have the following form: $d_{z^2} = (3z^2 - r^2)/\sqrt{12}$, $d_x = (x^2 - y^2)/\sqrt{6} - xz/\sqrt{3}$ and $d_y = xy/\sqrt{2/3} + yz/\sqrt{3}$.[4] At room temperature the site symmetry of vanadium is trigonal instead of cubic as the octahedron is stretched along the c-axis which further splits the t_{2g} orbitals to one d_{z^2} and a remaining 2 fold degenerated $e(t_{2g})$, formed by d_x and d_y. At $T_s = 250\,\mathrm{K}$, where a zigzag develops along the vanadium chain, the site symmetry of vanadium is further reduced from hexagonal to orthorhombic. The whole sequence of the level splitting is shown in Fig. 2.3.

The order of the d_{z^2} level and the $e(t_{2g})$ doublet is arbitrary at the present state. The shape and the orientation of the lobes of these orbitals are illustrated in Fig. 2.4. It is obvious that d_{z^2} orbits have large direct overlap along the chains while $e(t_{2g})$ orbits, (d_x, d_y) can overlap only through sulfurs with their neighbours in the surrounding chains. If d_{z^2} was occupied, i.e. it was the low-lying level this

---

[3] This is the usual choice of the coordinate system.

[4] d_x and d_y are the ± 1 eigenstates of the orbital angular momentum L_z.

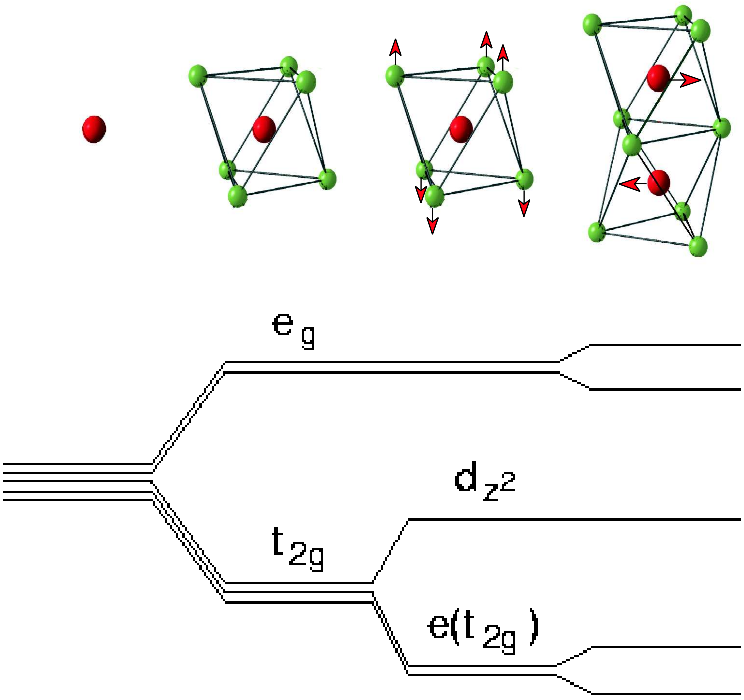

Figure 2.3: *Stages of site symmetry reduction of* V^{4+} *and the corresponding splittings of* 3*d levels: isotropic→octahedral→ trigonal→orthorhombic.*

fact should result in a very anisotropic conductivity with the *c*-axis as the good conducting direction. However, this picture is not supported at all by our electrical conduction anisotropy measurement [21] which rather suggest an isotropic electron system by the ratio of $\sigma_c/\sigma_{a-b} \approx 3.4$.

2.4 Band calculations

The previous crystal field approach on the basis of group theory gives information about the level structure only at the origin of the Brillouin zone (BZ) and does not reveal the energy dispersion of the levels. However, it can happen that orbits with higher energy near the zone center cross the Fermi level at certain points of the BZ, taking part in the distribution of charge carriers in this way. Band calculation is a possible candidate to explore these details and also to verify our apriori consideration that a simple ionic picture gives appropriate description of

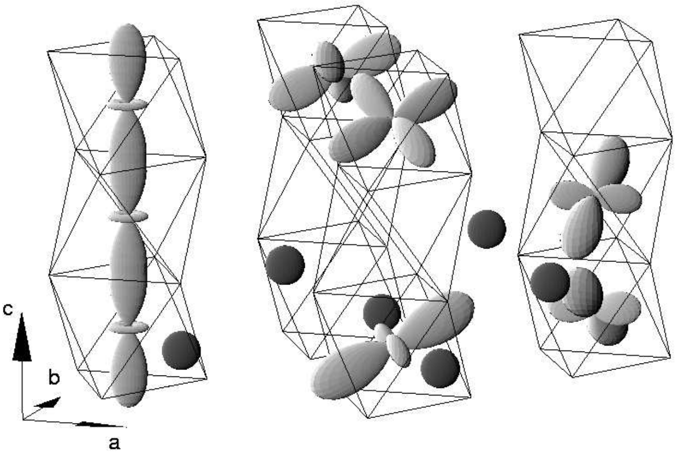

Figure 2.4: *Orientation of the low-lying orbitals relative to the crystal structure.*

$BaVS_3$.

Results of linear augmented-plane-wave (LAPW) method applied for both crystallographic phases of $BaVS_3$ in the local density approximation by L. F. Mattheiss in Ref. [4] is presented below. In the hexagonal phase lattice parameters at room temperature while in the orthorhombic phase those at $T = 100\,\mathrm{K}$ were utilized. In this study the two outer shells of each components[5] were treated as valence electrons and the remaining ones are included in a frozen-core approximation. With two formula unit per unit cell we have 10 levels belonging to vanadiums and 38 levels in total.

The Fermi level turns out to be located at the lower edge of the t_{2g} manifold while e_g subbands lying at higher energy are unoccupied. (Though $S(3p)$ is slightly hybridized with t_{2g}, sulfur and barium essentially have neither valence nor conduction bands.) The widest one of the t_{2g} complex are d_{z^2} conduction bands whose $\sim 3\,\mathrm{eV}$ width originates both from large direct $V - V$ overlap along the chain and indirect overlap via $S(3p)$ obitals. Levels of $e(t_{2g})$ are about 4 times narrower with a value of $\sim 0.7\,\mathrm{eV}$.[6] The band filling of the lowest $e(t_{2g})$ is 0.93 (close to the fulfilled situation) which means $2 \times 0.07\,$holes/unit cell. Together with the compensating electrons populating the next member of $e(t_{2g})$ the overall

---

[5] $Ba(5p^6 6s^2)$, $V(3d^4 4s^1)$, and $S(3s^2 3p^4)$

[6] They have the same symmetry properties than the low-lying $d_x - d_y$ doublet of the single vanadium, but in this case, since two vanadiums form the unit cell, we have four of them.

carrier concentration is 0.28 charge/unit cell. LAPW predicts $BaVS_3$ to be metallic with rather low carrier density and compensated conductor with equal number of electrons and holes.

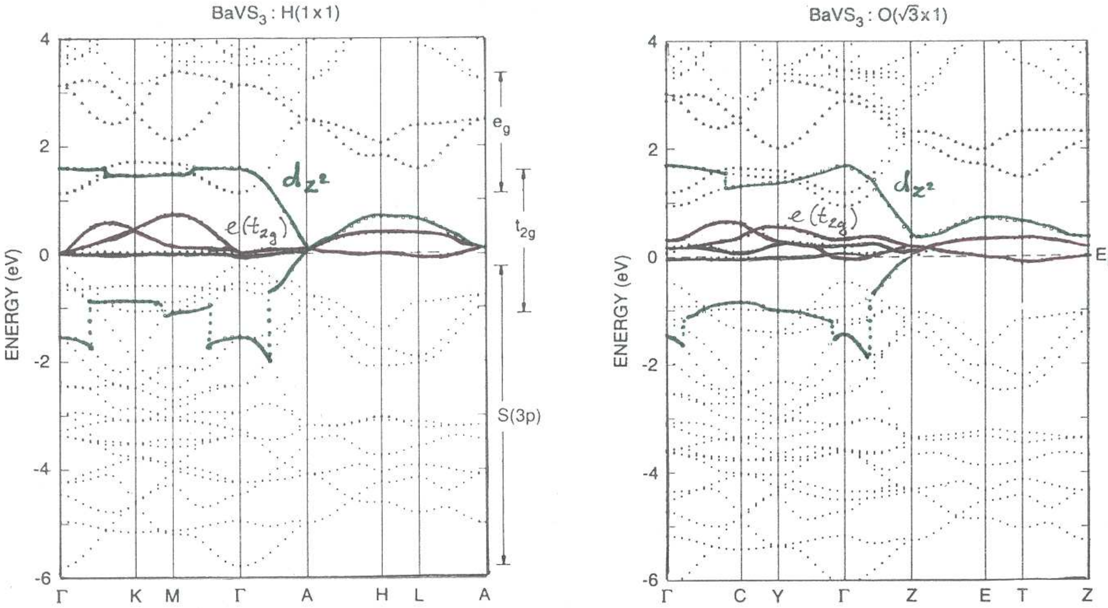

Figure 2.5: *Energy band results for hexagonal and orthorhombic $BaVS_3$ along the symmetry lines of the Brillouin zone from Ref. [4].*

After having a look at the band structure of the orthorhombic phase in the right panel of Fig. 2.5 we can notice that the structural transition at $T_s = 250\,\mathrm{K}$ are accompanied with no radical changes. Each of the $e(t_{2g})$ remains two fold degenerated in an extended region of the BZ (in the ETZ plane) and the most remarkable effect is that, the carrier concentration doubles. (We have 0.3 holes/unit cell and 0.3 electrons/unit cell from now on.) The first statement all alone guarantees – concerning the author – "that hexagonal $BaVS_3$ metallic properties will persist in the orthorhombic phase." Though the orthorhombic distortion is not saturated at all at $T = 100\,\mathrm{K}$ the above argument is valid at any lower temperature since an additional symmetry change would be required to remove the degeneracy of $e(t_{2g})$ subbands. Thus, the metal-insulator transition observed at $T_{MI} = 70\,\mathrm{K}$ cannot be deduced from band calculations, ergo $BaVS_3$ at low temperatures is not a simple band insulator but probably correlation effects drive the system towards the insulating phase.

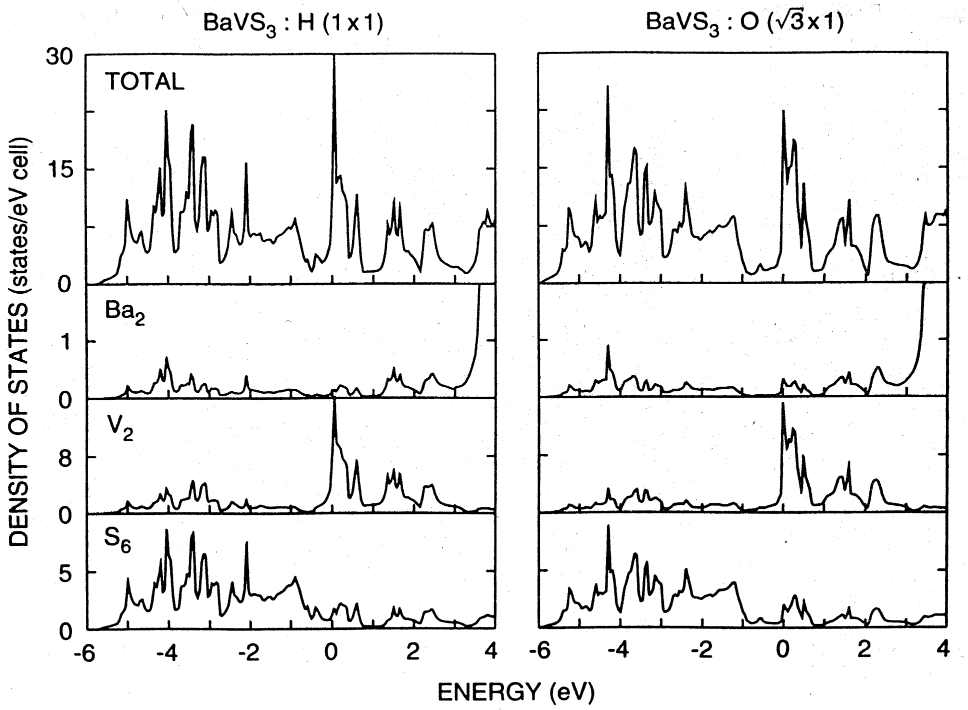

Figure 2.6: *Total and muffin-tin-projected density of states for hexagonal and orthorhombic* $BaVS_3$ *from Ref. [4].*

The previous section was strongly based on the hypothesis that perfect charge transfer happens in the material and the components are in the following valence states: V^{4+}, Ba^{2+} and S^{2-}. This picture is supported by the above band structure calculation whose conclusion is that “an ionic model is a reasonable starting point for describing the electronic properties of both hexagonal and orthorhombic $BaVS_3$” [4]. It has to be mentioned here that in photoemission studies of Itti et al. [5] different valences were concerned for the components: 3.41+, 2.21+ and 1.87− for V, Ba and S, respectively. However, the authors emphasize themselves that it can be considered as a qualitative result rather based on the so-called bond-valence-sum method than the XPS data. In this method the valence of an atom can be calculated from its interatomic distances with surrounding atoms which is a rude approximation relative to the band structure theory.

2.5 Nature and order of the phase transitions

The $T_s = 250\,\mathrm{K}$ structural transition does not seem to have strong influence on the electronic states as proved by either the lack of its sign in thermodynamic properties or the band structure calculations. Thus, we will focus on the other two transitions which surely involve different electronic degrees of freedom and whose nature has not been clarified yet.

The most robust phase transition of the system is the metal to insulator transition. It appears in almost each quantity which has been measured so far and it has been identified to be of various kinds and orders.

In the early work of O. Massenet at al. [6], they concluded that in the insulating phase quasi-1D antiferromagnetic order sets in along the vanadium chains. This suggestion was based on the AF-like cusp of the magnetic susceptibility below 70 K and the impressive chain-like structure of the compound. Their two-band model which could explain both the contradictory high-temperature phase and the vanishing susceptibility of the insulator is as follows: the d_{z^2} orbitals, oriented along the chain direction, form a wide conduction band which incorporates the narrow bands (related to the two lowest d levels) partly occupied. The former is responsible for the metallic conductivity while the narrow bands cause the Curie susceptibility of localized moments. The scenario for the magnetic aspect of the 70 K transition is that a gradual electron transfer from the localized magnetic states to the non-magnetic states occurs. It is driven by the modification of the band structure due to the decrease of the c-axis parameter with lowering the temperature. However, $p_{eff} \approx 1.4\ \mu_{Bohr}$ suggests that the most part of the electrons belongs to the narrow magnetic band, therefore the wide conduction band is far from half-filling. Furthermore, the susceptibility starts to freeze out just below the transition. This does not allow such a large charge redistribution which could be the direct reason for a transition towards the insulating phase. Additionally, their Mössbauer spectroscopy measurement allows only to consider the presence of a dynamical, short range order and the frozen 3D order, if it exists, could step in at lower temperature. Static magnetic ordering is also excluded by neutron diffraction data and no static local fields are observed in NMR [7], NQR

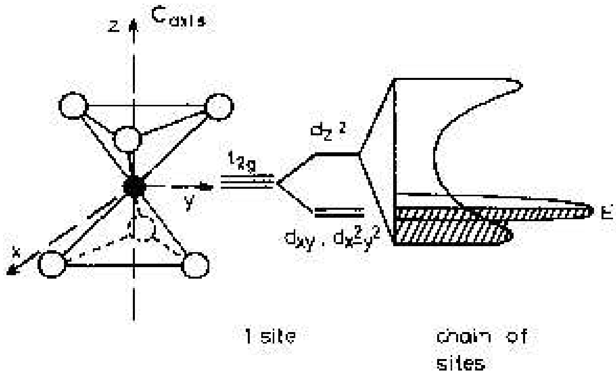

Figure 2.7: *The local environment of vanadium responsible for the crystal field splitting and the two band model of Massenet et al.*

[8] and spin-flip scattering experiments [9].[7]

The picture of gradual pairing of magnetic V ions, i.e. a spin-Peierls transition (proposed by Ref. [7]) was also a candidate to be responsible for the vanishing susceptibility. Its existence is also ruled out, since such pairing should be accompanied by lattice distortion which has not been detected by X-ray diffraction studies [2, 3].

In the model of Nakamura et al. [10] the roles are distributed differently between the orbitals. The band associated with the d_{z^2} levels is unoccupied, since it is situated well above the Fermi level and does not overlap with the low lying doublet. Below $T_s = 250\,\mathrm{K}$ the doublet is split by the orthorhombic distortion (shown in Fig. 2.2) which gradually increases down to 70 K, resulting in a charge transfer to the energetically favourable orbital. At T_{MI} the distortion has a discontinuous component and almost saturates below suggesting the complete transfer of carriers to the low lying orbital. “At this stage, the lowest one of the $e(t_{2g})$ is half filled, and a Mott-Hubbard gap opens at the Fermi energy.” On the basis of their photoemission study they also emphasize the 1D character of the electron system[8] and argue that long range magnetic order is prevented by the

---

[7] At least the ordered moment is predicted to be smaller than $0.1\,\mu_{Bohr}$ which could not explain the large reduction in the susceptibility.

[8] “High resolution UPS spectra near the Fermi level in the metallic phase exhibit a power-low dependence of the electron binding energy, indicating that the conduction electrons in $\mathrm{BaVS_3}$ form a Luttinger liquid.”

large fluctuation effects in one dimension and can be established at $T_x = 30\,\mathrm{K}$. The evolution of their valence-band spectra with temperature is continuous without abrupt change at the metal-insulator transition. This behaviour is attributed to the opening of the band gap above the transition. This kind of precursor effect could be also manifested in the upturn of the resistivity below $\sim 140\,\mathrm{K}$. If the one band Mott-Hubbard scenario of Nakamura et al. is true the orbital degeneracy is quenched by the metal-insulator transition. This would rule out the onset of orbital order at lower temperatures, thus contradicts the observation of the NQR measurement.

Graf et al. in Ref. [11] try to identify the order of the transition by combining their results with earlier observations. At first, they explore a continuous line of the metal-insulator phase boundary in a wide range of pressure ($p = 0 - 15\,\mathrm{kbar}$) by measuring the resistivity. The transition turns out to be suppressed at a rate of $\sim 3.5\,\mathrm{K/kbar}$. In linear extrapolation one would expect the metallic phase to be extended down to zero temperature under 20 kbar. Then, they investigate the thermal expansion of the system from 4 K up to 120 K and find a sharp peak in the thermal expansion coefficient and a slight volume contraction ($\Delta V/V = 0.019\%$) on warming through T_{MI}. The existence of a continuous $p - T$ phase boundary, the very slight volume change near the transition and the lack of hysteresis in measured quantities are all against a first order transition. The possibility for the transition to be of second order is argued to be improbable since basic order parameters which could be adequate for the system, like magnetic order or further crystal symmetry reduction, are experimentally excluded. Since the symmetry above and below T_{MI} is not broken, i.e. the transition is isomorphic. In their proposal this phenomenon is nothing else but a continuous transition just beyond a first-order critical point at ambient pressure and further beyond at higher pressures. In order to prove their proposal they separate a term in the thermal expansion related to the transition which shows smooth evolution in the vicinity of 70 K without any sign of criticality.

2.6 Strength of the electron correlation

It is a common believe that electron correlations play an important role in either phases of $BaVS_3$. The interaction energy between two electrons can be different depending on their spin and orbital quantum number which allows the system to exhibit collective behaviour either in spin or in orbital sector.

The leading term of the correlation energy is the on-site Coulomb interaction which for the $3d$ shell is $U \approx 1\,\mathrm{eV}$.[9] Though the overall bandwidth is $W \approx 3\,\mathrm{eV}$ due to the wide d_{z^2} as shown in Fig. 2.5, the total occupation of this level is poor, restricted in k-space to the close vicinity of the A point of the Brillouin-zone. Along the $\Gamma - K - M - \Gamma - A$ line its energy is much higher than that of the $e(t_{2g})$ levels and they become comparable only along the $A - H - L$ line. Thus, the effective bandwidth must be closer to $W_{eff} \approx 0.7\,\mathrm{eV}$ characteristic to the $e(t_{2g})$. In sense of the U/W_{eff} ratio the system is found to be on an intermediate scale. The relative strength of the interaction, all alone, would not unambiguously compel an insulating ground state.

---

[9] It can be slightly different for electrons occupying the same or two different orbitals.

Chapter 3

Experimental methods and setups

3.1 Sample preparation

Single crystals of $BaVS_3$ were grown by Tellurium flux method.[1] Powders of $BaVS_3$ and sublimated tellurium 99.99% Vetron were mixed in a molar ratio $1 : 50$ and heated up to 1050° C in an evacuated silica ampoule. Then it was slowly cooled down to 55°C at a rate of 1° C/hour. The crystals, obtained from the flux by sublimation, have typical dimensions $0.5 \times 0.5 \times 2\,\mathrm{mm}^3$.

Both the transport and the low-temperature magnetic properties of the material strongly depend on the stoichiometry, especially on the sulfur content [6]. The crystals used in our experiments were previously qualified by dc conductivity. The criteria for a good sample are discussed in 4.1.1.

3.2 Electrical conductivity measurements under pressure and in magnetic field

The application of hydrostatic pressure is a useful tool which gives us the possibility to continuously increase the bandwidths of a material by decreasing the lattice constant. While the overlap integral depends exponentially on the distance of the neighbouring atoms, the on-site electron-electron interaction is insensitive

---

[1] The samples were prepared by H. Berger in Prof. László Forró's laboratory at the EPFL in Lausanne.

of it. Thus, the application of pressure usually drives the systems towards a more delocalized state. In systems with anisotropic crystal structure the stiffness of the lattice may be very different in the various crystallographic directions. In these cases the application of pressure also changes the anisotropy of the overlap integrals. In $BaVS_3$ the chain direction has the highest compressibility, therefore the pressure induced reduction of the anisotropy is expected.

The resistivity measurements have been performed using the standard four-probe method in the temperature range of $T = 1.2 - 300\,\mathrm{K}$. (At ambient pressure the investigations were extended up to 700 K.) The contacts were made by evaporating thin gold pads on the crystal. Then $20\,\mu$m thin gold wires were fixed on these pads by silver paint. For illustration, a $BaVS_3$ crystal in the typical four-probe arrangement is shown in Fig. 3.1B. For the measurements under hydrostatic pressure the crystals were inserted into a non-magnetic copper-berilium cell with kerosene as pressure medium. The pressure was monitored in situ by an InSb sensor. During cooling down the cell a slight pressure loss occurs due to the different thermal expansion of the pressure medium and the body of the cell, however, its influence on the temperature dependence of the resistivity is negligible. Above 15 kbar the pressure is stable within 0.2 kbar in the whole temperature range.

The self-clamping pressure cell and its accessories are shown in Fig. 3.1A. The delrin capsule with CuBe plugs at both ends and filled with kerosene embeds the sample. One of the plugs serves also as electrical leadthrough. The rings covered with indium are against leaking. The whole arrangement is put into the hole in the cell body and fixed on one side by the solid screw while on the other side a piston enters the hollow screw and transmits the force to the capsule.

The magnetoresistance (MR) has been investigated in two ways: by magnetic field sweeps up to 12 T at various temperatures and by measuring the temperature dependence of the resistivity in constant fields, usually in $H = 120\,\mathrm{kG}$. During the field sweeps a Cs-403 capacitive thermometer was used to stabilize the temperature, eliminating any temperature drift arising from the magnetoresistance characteristic of resistive thermometers. During the constant field measurements the temperature was monitored by a CGR-500 thermometer having relative temperature error due to the magnetic field, $\Delta T/T \leq 2\%$ in $H = 120\,\mathrm{kG}$ from $T = 30\,\mathrm{K}$ up to 90 K. Even this small deviation was corrected by calibrating the

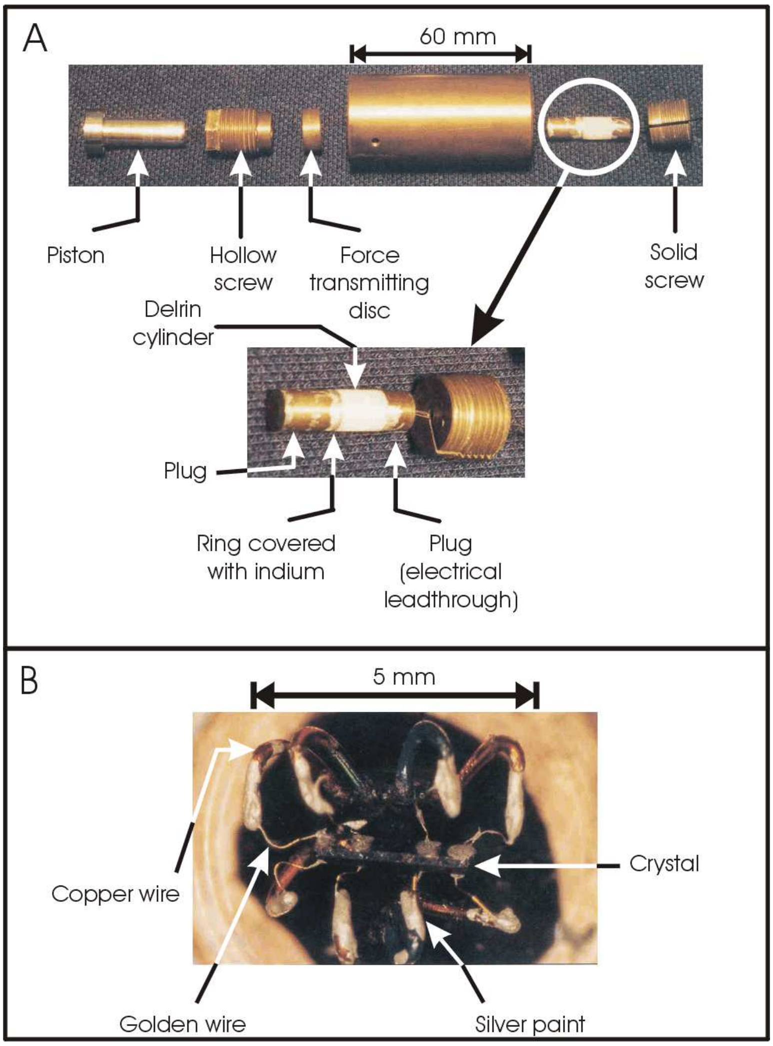

Figure 3.1: *The self clamping pressure cell and its accessories.*

magnetoresistance of the CGR-500 at every 5 K in the interesting temperature interval maximum using the capacitive sensor. Thus the overall uncertainty of the temperature is smaller than ±0.05 K in the whole region.

At ambient pressure the conduction anisotropy of the system has also been measured using Montgomery method [12].

Though the conductivity has mainly been investigated using dc technique, under high pressures and at low temperatures the phase diagram has been explored by low-frequency lock-in detection. Its application was necessary because of the very small resistance of the samples (in the range of 100 MΩ) and the high ratio of the contact and sample resistance (often as large as $\sim 10^5 - 10^6$). Since the pressure medium applied in the experiments is not a good heat-conductor, lock-in detection was also required for low-power measurements keeping the heat dissipated on the contact resistances below few μW.

3.3 Thermoelectric power measurements under hydrostatic pressure

Transport coefficients can be divided into two classes, those being associated with "primary flows" under the action of "primary forces" and those relating "primary flows" with "coupling forces". The formers are the diagonal, while the latters are off-diagonal elements in the formulation of the Onsager transport equations. In contrast to the electrical conductivity which relates the electric current density to potential gradient, the thermoelectric power (TEP) is an off-diagonal coefficient, which couples the electric current to the temperature gradient. The Onsager relations for particle and heat current density, J and J_Q, in presence of chemical potential and temperature gradient are:

$$J = -\frac{\sigma}{e^2}\nabla\overline{\mu} + \frac{S\sigma}{\mid e \mid}\nabla T \quad , \tag{3.1}$$

$$J_Q = \frac{ST\sigma}{\mid e \mid}\nabla\overline{\mu} - (\kappa + TS^2\sigma)\nabla T \quad , \tag{3.2}$$

where σ, κ, S are the electrical, the heat conductivity and the TEP, respectively. If no electric current flows than the Seebeck coefficient is defined by the two forces:

$$S \mid e \mid \nabla T = \nabla\overline{\mu} \quad . \tag{3.3}$$

Instead of the gradient of the temperature and the chemical potential their changes on a finite length scale are measured, i.e. they are integrated between two points. Usually the thermal isolation of the sample from its environment is not perfect. How does it influence the measured value of the thermoelectric power? Since the result of integration of Eq. 3.3 does not depend on the path – the integrands are rotationless vector fields – one can always choose a path inside of the sample. Thus the integrated quantity is solely characteristic of the sample and it is not influenced by the surrounding material:

$$\Delta\overline{\mu} = \int_{\underline{x}_1}^{\underline{x}_2} S(T(\underline{x}))\nabla T(\underline{x})d\underline{x} = \int_{T}^{T+\Delta T} S(T')dT' = S\Delta T + \frac{\partial S}{\partial T}\frac{(\Delta T)^2}{2} + \cdots \quad (3.4)$$

It has a great importance in our TEP measurements where the sample is embedded in a pressure medium. In first order the thermoelectric power can be written as the following:

$$S = \frac{1}{\mid e \mid}\frac{\Delta\overline{\mu}}{\Delta T} \quad . \quad (3.5)$$

According to Eq. 3.5 the voltage and the temperature difference should be detected between the same two points of the sample. Since the typical dimensions of the $BaVS_3$ single crystals are $0.5 \times 0.5 \times 2\,\mathrm{mm}^3$ it is not evident to measure the temperature and the voltage at the same place (within a distance which is negligible compared to the length of the crystal). Due to this possible error of the contact positions there is some uncertainty in the absolute value of the TEP. In order to eliminate this kind of systematic error we measured the TEP of a few large crystals (with typical length of $\sim 4\,\mathrm{mm}$) in vacuum. This room temperature value ($S = -25 \pm 2\,\mu\mathrm{V/K}$) served as a standard for the later measurements performed in the pressure cell. Apart from the deviation in the absolute values, the temperature dependence of the thermoelectric power measured on small crystals at ambient pressure inside of the pressure cell (filled with liquid) is in good agreement with those measured on large crystals in vacuum.

The arrangement used in the TEP experiments is shown in Fig. 3.2. The sample lies on a ceramic pad with heaters at both ends. E-type ($chromel-constantan$) differential thermocouple with the two junctions fixed on the ceramic close to the ends of the sample was used to monitor the temperature difference. This ensures a good thermal contact to the ends of the crystal but the junctions remained electrically isolated from the crystal. The voltage drop due to the thermal gradient

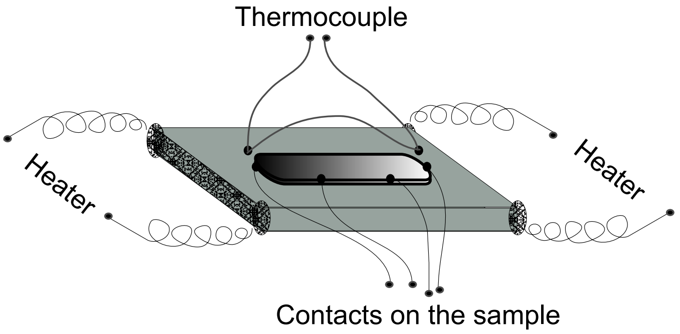

Figure 3.2: *Line drawing of the arrangement used in TEP measurements.*

is measured on the outer contacts, while the inner contacts are only used for the simultaneous four-probe detection of the resistivity.

All wires are connected to the copper wires of the sample holder. In order to eliminate the additional voltage drop introduced by these second junctions they are thermalized to a common temperature. In this arrangement the measured quantity is not the absolute thermoelectric power of the crystal but that relative to the gold. However, the absolute TEP of the gold is at least one order of magnitude lower than that of $BaVS_3$ so we do not take it into correction in our results. At room temperature $S_{Au} \approx 2\,\mu$V/K while $S_{BaVS_3} \approx -25\,\mu$V/K. For a detailed temperature dependence of the thermoelectric power of gold, see Ref. [13].

The heating power is equidistantly stepped up to a maximum value and then decreased to zero while the temperature difference and the corresponding voltage drop are measured simultaneously. The slope of the line fitted to the data is the Seebeck coefficient (see Fig. 3.3).

It is evident that higher heating power results in larger signal. Do we have any limitations for the temperature difference along the sample? Eq. 3.4 shows that the sample is not overheated (i.e. the measured difference in the chemical potential is proportional to the temperature change) as far as $\partial S/\partial T \Delta T \ll S$. If the TEP is strongly temperature dependent, the proportionality of the voltage drop with temperature difference has to be checked. In case of nonlinearity the heating power has to be decreased until the effect of the higher order terms becomes negligible. According to Eq. 3.4 the linear term vanishes when the thermoelectric power zero

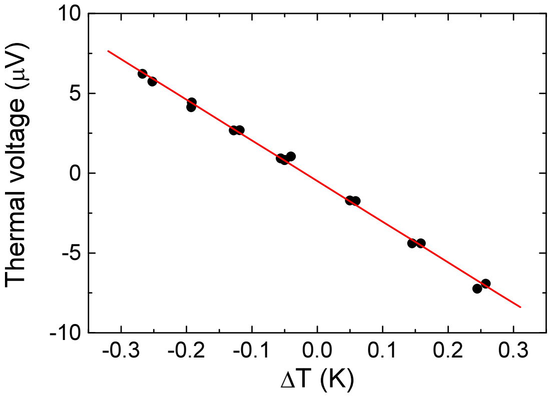

Figure 3.3: *Representative cycle of TEP measurement on* $BaVS_3$.

and higher order terms appear. The graph in Fig. 3.4 shows remarkable deviation from the linearity due to the sign change in the Seebeck coefficient at the MI transition of $BaVS_3$.

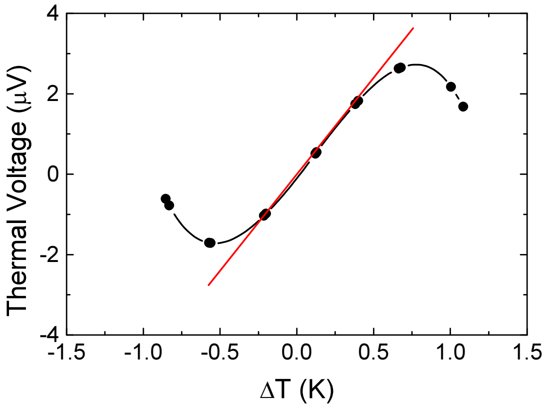

Figure 3.4: *The effect of overheating appearing in* $\Delta\overline{\mu}$ *vs.* ΔT *curve.*

If the junctions of the thermocouple are not heat-linked well to the end of the sample it gives rise to a difference between the slopes measured with opposite temperature gradients.

The TEP of an insulator is usually hard to measure when its resistance is higher than 10 MΩ. As the conductivity of the sample decreases the heat conductance of the contacts becomes worse and the time needed for the thermalization (between the sample and the thermocouple) can be as large as a few seconds. The resulting

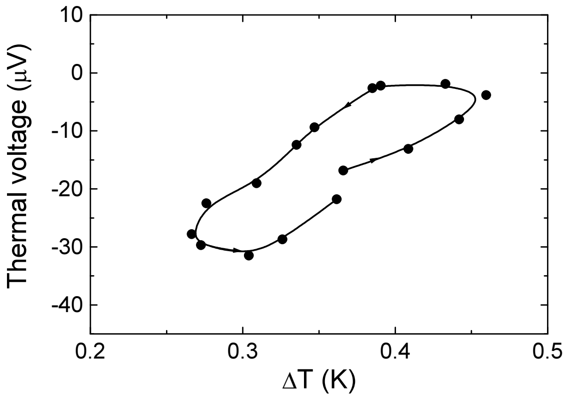

Figure 3.5: *Hysteresis in $\Delta\overline{\mu}$ vs. ΔT curve due to the slowing down of the relaxation inside of the insulating phase.*

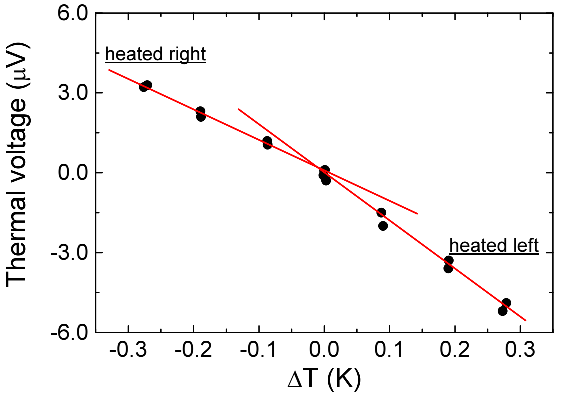

Figure 3.6: *Break in the slope of $\Delta\overline{\mu}$ vs. ΔT graph related to the application of heaters on different side of the sample.*

hysteresis is clearly shown in Fig. 3.5.

In case of TEP measurements under pressure the differential thermocouple is also inside of the cell. The pressure dependence of its thermoelectric power may cause a systematic error in the measured temperature difference. However, the commonly used thermocouples are composed of metals with wide conduction bands, thus they are insensitive to the pressure. A detailed overview of the topic is given in [14]. For example, the sensitivity of our E-type thermocouple at room temperature is $\partial S/\partial p \approx 0.03\,\mu$ VK^{-1}kbar^{-1} while its absolute value at ambient pressure is $S = 60\,\mu$V/K. In the range of the highest pressure applied in our experiments ($p = 22\,\text{kbar}$) this corresponds to a systematic error $\lesssim 1\%$.

3.4 Optical conductivity measurements in the infrared region

Infrared (IR) spectroscopy is a useful tool to study the excitations accompanied with electrical polarization in the range of $1\,\text{meV}-10\,\text{eV}$. Since the wavelength of the light in the above frequency range $\lambda = 10^{-5} - 10^{-1}\,\text{cm}$ is much larger than the lattice constant, the electromagnetic field can be considered homogeneous on the scale of the atomic distances. Due to the small wave number of the light no momentum transfer occurs during the scattering. Only "vertical processes" are allowed and the dispersion relation of the excitations cannot be directly revealed by this method. The typical excitations studied by optical spectroscopy include IR active phonon scattering, two-phonon processes of acoustic branches, as well as several kinds of electronic excitations, like polarization of atomic electron shells, single electron excitation through a charge gap, or conduction of propagating carriers.

In order to determine the complex electronic susceptibility of a system, two real quantities of the light scattering have to be simultaneously detected. The common choice is the measurement of the absolute value of the reflectance and the transmittance (instead of detecting either of them together with its phase). If only one of them can be measured, the complex susceptibility is obtained by Kramers-Kronig transformation. In our case, in the metallic phase of $BaVS_3$ the penetration depth ($\delta \sim 1\mu\,\text{m}$) is much smaller than the sample width ($w \sim 1\,\text{mm}$), thus only the reflectance can be detected.

3.4.1 Along the optical path: light source, sample, spectrometer and detector

Our IR measurements have been performed at the National Synchrotron Light Source (NSLS) of the Brookhaven National Laboratory. The basic features of the synchrotron light are the high brightness and the large bandwidth (from far IR up to UV). Its brightness is 10 times larger than the brigthness of other commonly used internal sources in the $1-400\,\mathrm{cm}^{-1}$ range ($1cm^{-1} \approx 1.4\,\mathrm{K}$). This is the energy scale which is characteristic of the low energy excitations in correlated systems where collective phenomena appear.

The intensity of the light reflected back from the sample has to be measured relative to a reference signal for several reasons. The white light coming from the synchrotron has no uniform power spectra and its frequency distribution has to be eliminated from the results. Further reasons are the time dependent power of the synchrotron light, the dispersion of the optical elements (filters, beamsplitters) and the frequency dependent sensitivity of the detectors. The reference signal is usually obtained by replacing the sample with a perfectly reflecting metallic mirror. However, in the low-frequency range ($1-100\,\mathrm{cm}^{-1}$), which we focus on, where the typical sample size (1 mm) becomes comparable to the wavelength the intensity of the collimated part of the light scattered back from the crystal is more and more damped. This diffraction also influences the frequency dependence of the reflectivity. Therefore using a simple metallic mirror is not sufficient to get the proper reference signal and one has to in-situ evaporate gold directly on the sample and measure its reflectance, too. This supplies the reference signal which can be used to normalize the measured intensities.

If he surface of the sample is not absolutely flat, i.e. its roughness is around a few $\mu\,\mathrm{m}$, than the components of the light having the same or smaller wavelength are reflected diffusively. This error is eliminated by the above choice of the reference signal, moreover it appears at frequencies higher than $10^4\,\mathrm{cm}^{-1}$ which range is out of our interest.

The sketch of the main chamber of the spectrometer (Bruker IFS113v) is shown in Fig. 3.7. The drawing is oversimplified and focuses on the arrangement of mirrors.

The incoming light arrives to a parabolic mirror ($PM\#1$) whose focus is set to the center of the first diaphragm ($D\#1$). Since the beam is not perfectly collimated a finite size spot appears there. The more closed the blende is the bigger part of the divergent light is cut off, i.e. the beam is more collimated and the images of this focus become better defined. On the other hand, $D\#1$ is situated in a distance of R from the first spherical mirror (where R is the radius

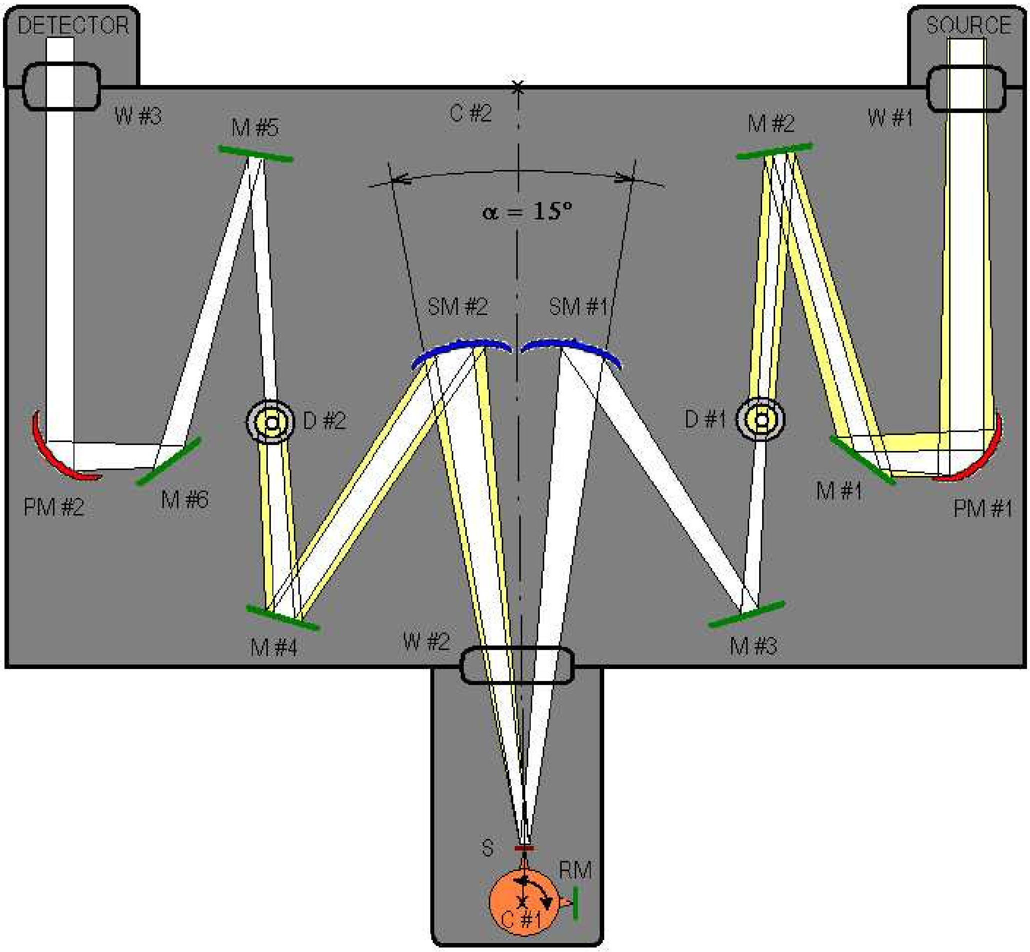

Figure 3.7: *Simplified picture of the main chamber of the spectrometer, where* ***M****,* ***PM*** *and* ***SM*** *mean flat, parabolic and spherical mirror,* ***D*** *is diaphragm and* ***W*** *is vacuum proof transparent window,* ***S*** *and* ***RM*** *label the sample and the reference mirror, respectively.*

of the mirror) but weakly rotated out from its origin. Thus, the image of the focus appears in the same distance but tilted out by double angle. This is the place of the sample. If the arrangement of the mirrors is symmetric to the line connecting $C\#1$ with $C\#2$ and the surface of sample perpendicular to it, the light directly goes into the detector. The symmetric path is not a necessary restriction, because the flat mirrors are movable and rotatable and give some freedom to choose between various equivalent paths. The purpose of the first diaphragm is to reduce the spotsize at the focus below the sample size while the second blende only lets that part of the light pass through which is reflected back from the crystal and eliminates those coming from out of focus reflections (for example: from $W\#2$). The application of the two diaphragms is even more important in the case of high-pressure experiments. The reference signal is recorded under the same circumstances by 90° rotation of the sample holder when the reference mirror (RM) is moved to the sample position.

In our measurements the $20 - 4000\,\mathrm{cm}^{-1}$ range has been investigated. This interval cannot be covered with a single detector. A composite bolometer is used for long wavelengths ($20 - 700\,\mathrm{cm}^{-1}$), while in the middle infrared, MIR ($400 - 4000\,\mathrm{cm}^{-1}$), a photoconductor detector is applied. The large overlap between the two sensors is necessary because their sensitivity drop down close to the edges of the range of applicability. Fig. 3.11 shows typical spectra detected in both ranges.

The frequency of the light in the IR region ($>$ terahertz) is usually too high to permit the signal to be detected in the time domain. In order to determine the reflectance as a function of frequency we used a Fourier transform spectrometer based on a Michelson interferometer (see Fig. 3.8). Next we discuss the principles of its operation.

The measured quantity is the time autocorrelation function of the light:

$$G(\tau) = \langle E^{\star}(t)E(t+\tau)\rangle \equiv \lim_{T\to\infty} \frac{1}{2T}\int_{-T}^{T} E^{\star}(t)E(t+\tau)dt \quad , \tag{3.6}$$

where $G(\tau = 0)$ is the time averaged intensity. In this method a beamsplitter divides the beam into two parts which go along two arms with different length. Both arms have a mirror at the end. By moving one of these mirrors the optical path difference, $2\Delta x$ can be changed. Since the time delay is related to the path difference ($\tau = 2\Delta x/c$), by measuring the intensity as a function of path difference the autocorrelation function is determined. It can be easily shown that the power spectrum is its Fourier transform, i.e.:

$$S(\omega) \equiv\mid E(\omega) \mid^2 = \int G(\tau)e^{-i\nu\tau}d\tau \quad . \tag{3.7}$$

Before characterizing the resolution and bandwidth of the spectrometer two

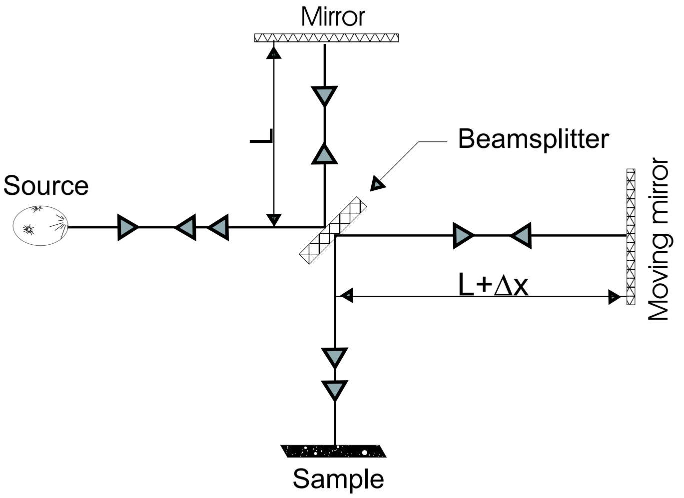

Figure 3.8: *Line diagram of the Michelson interferometer.*

quantities have to be introduced: the autocorrelation time ($\Delta\tau$) and the bandwidth ($\Delta\omega$) of the light. In both definitions the autocorrelation function of the corresponding Fourier space is used, i.e.:

$$(\Delta\tau)^2 = \frac{\int \tau^2 \mid G(\tau) \mid^2 d\tau}{\int \mid G(\tau) \mid^2 d\tau} \quad , \tag{3.8}$$

$$(\Delta\omega)^2 = \frac{\int (\omega - \omega_0)^2 \mid S(\omega) \mid^2 d\omega}{\int \mid S(\omega) \mid^2 d\omega} \quad , \tag{3.9}$$

where ω_0 is the frequency of the maximum in the power spectrum. Since $G(\tau)$ is the Fourier transform of $S(\omega)$ it is easy to show that the following reciprocal relation holds between bandwidth and correlation time:

$$\Delta\omega\Delta\tau = \sqrt{2}/2 \quad . \tag{3.10}$$

As a consequence, the lowest detectable frequency and the elementary unit of the frequency scale ($\delta\nu$) are cut off due to the maximum displacement of the moving mirror, since the time delay between the two interfering beams is limited to $\Delta\tau_{max} = 2\Delta x/c$. Thus $\delta\nu = (2\sqrt{2}\Delta x)^{-1}$ (in cm^{-1} units). Similarly, the bandwidth is reduced by the finite stepsize of the moving mirror, δ to $\Delta\nu =$

$(2\sqrt{2}\delta)^{-1}$.

Briefly summarizing, the frequency distribution of the intensity can be mapped by the spectrometer to a measurable quantity: the path dependent intensity (equivalent to the autocorrelation function of the light) whose Fourier transformation provides the frequency distribution of the intensity. The imperfectness of this mapping (it is discrete and limited to finite scale) introduces cut off both at high and low frequencies.

3.5 Optical conductivity measurements under hydrostatic pressure

Optical spectroscopy under hydrostatic pressure in the far infrared (FIR) range is not a commonly used technique. In order to measure the optical conductivity of a material placed into a pressure cell, the basic requirements are that the inserted window has to be sufficiently large, transparent and should not be damaged by high pressures.

Sufficient size means that the radius of the window is larger than both the spotsize of the incoming light and the maximal wavelength of the radiation. Otherwise the diffraction become strong as the wavelength approaches the window size. The hardness and the almost perfect transparency in the whole spectrum makes diamond to be the best candidate for such an optical window. It has only one multi-phonon absorption in MIR between 1500 and $2700\,\mathrm{cm}^{-1}$. This transparency is only valid for natural diamond because artificially grown diamonds contain nitrogen and are more absorbing. Zafir could also be an alternative by its hardness but it has absorptions in FIR, too.

A widely used equipment for high pressure optical studies is the diamond anvil cell. It can be applied up to extremely high pressures, typically several hundreds of kbar. In this device two conical shaped diamonds are pressed against each other with the pressure medium in between – forming an anvil-like shaped object as it is visualized in Fig. 3.9. However, the free surface of the diamonds (the window size) is small, it corresponds only to $100 - 150\mu\,\mathrm{m}$ in diameter, which introduces a low-frequency cutoff about $100\,\mathrm{cm}^{-1}$.

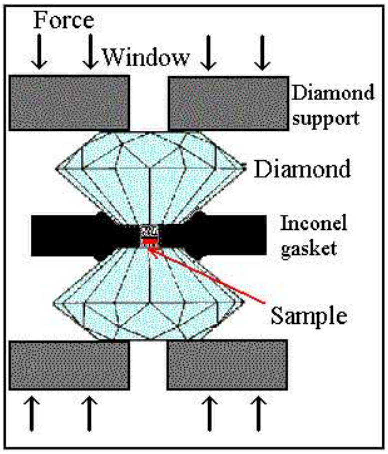

Figure 3.9: *The sketch of the so-called diamond anvil cell.*

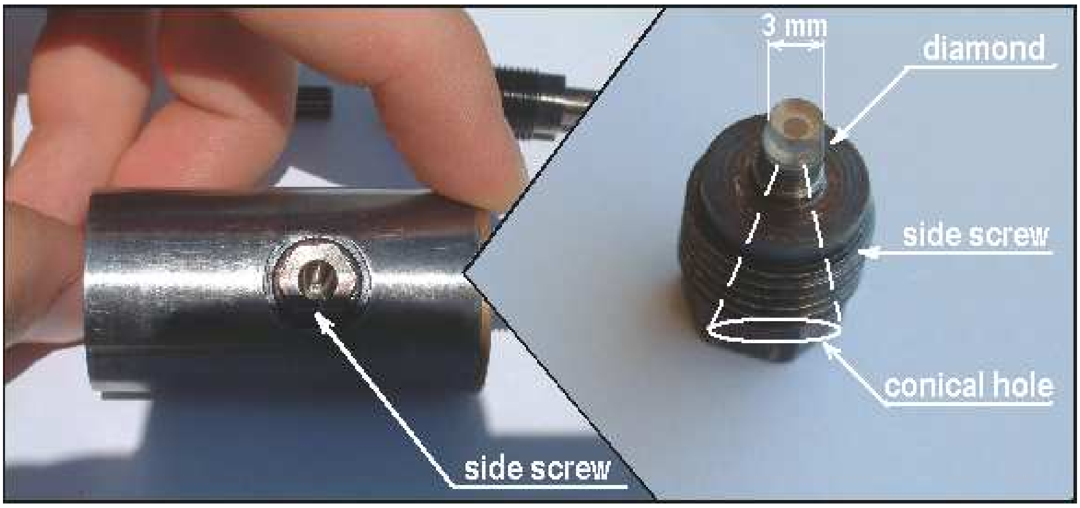

Figure 3.10: *Our self designed optical pressure cell. The window size is determined by the diameter of the conical shape boring at the top of the side screw where the diamond sits.*

We designed an optical pressure cell in which a large cylindrical shaped diamond (diameter: 3 mm, length: 2 mm) is embedded in a stainless steel body. There is a conical shaped hole through the screw, which fixes the diamond in the cell. The opening angle of the whole is 28° and its diameter is 1.5 mm at the narrow end where the diamond is placed (see Fig. 3.10). The highest pressure acts on this part of the cell. Notice, that it is only 4/3 times larger than the hydrostatic pressure inside of the cell. This means that the range of applicability of such a device is close to that of the self-clamping type pressure cells (presented in 3.2) made of the same material. We tested our design to operate safely up to 30 kbar without any deformation. In most of the correlated systems the interesting phenomena appear in this range. Compared to the diamond anvil cells we win a factor of 10 in the window size, i.e. in the low-frequency cutoff.

The sample lies on the inner face of the diamond, so it is not straightforward to find a good reference. As the window size of the cell is too small one cannot place a mirror next to the crystal. Instead, we use the light reflected back from the front surface of the diamond as a reference signal. In order to separate the reflection from the front and back surface (the latter is the diamond-sample boundary) the diamond is slightly wedged with an angle of 2° between the two faces. This small angle results in a $\sim 10^\circ$ angular deviation between the reflection from the back and the front surface due to the large refractive index of the diamond. It means that only one of the reflections can hits the spherical mirror $SM\#2$. We can switch between the images of the front and back face by a $\sim 7^\circ$ rotation of the pressure cell. It is clear that the opening angle of the cone plays crucial role in the experiment. The total angle covered by the incident and reflected light is $\alpha = 15^\circ$, as shown in Fig. 3.7. Together with the 7° rotation of the cell we end up with an opening angle of the cone at least 22°.

Fig. 3.11 shows the typical reflected intensity from the back and front surface of the window. The frequency dependence of the higher intensity, reflected from the front surface, is due to the dispersion of the optical elements including the synchrotron source. The dispersion of the beam reflected from the back surface is modified in the range of $1500 - 2700\,\mathrm{cm}^{-1}$ by the multi-phonon absorption of the diamond. Since the refractive index of the diamond is almost real and frequency independent ($n_d \approx 2.43 - 1.5/\omega(\mathrm{cm}^{-1})$) the intensity reflected from the front face:

$$R^f(\omega) = S(\omega) \left| \frac{n_d(\omega) - 1}{n_d(\omega) + 1} \right|^2 \approx 0.17 S(\omega) \quad , \tag{3.11}$$

while the reflected fraction from the diamond-sample boundary:

$$R^b(\omega) = S(\omega)(1 - R^f(\omega))^2 \left| \frac{n_s(\omega) - n_d}{n_s(\omega) + n_d} \right|^2 \approx 0.68 \left| \frac{n_s(\omega) - 2.43}{n_s(\omega) + 2.43} \right|^2 S(\omega) \quad , \tag{3.12}$$

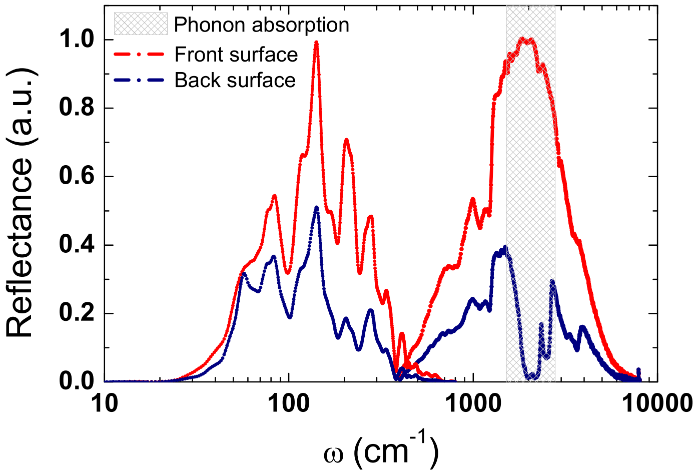

Figure 3.11: *The reflection from the front and back surface of a diamond is indicated by red and blue graph, respectively. The intensity vanishes for the light going through the diamond as it is seen in the grey patterned region.*

where n_s is the refractive index of the sample and $S(\omega)$ is the power spectra of the incident beam. Since the diamond is wedged the multiply reflections between the two faces are scattered out of the optical path: the light doubly reflected by the diamond-sample boundary is deviated with about 10° relative to the singly scattered one.

The result of the measurement is the ratio of the two quantities (R^b/R^f) which is proportional to the reflectivity of the sample relative to the diamond, $R_{s/d}(\omega) = \left|\frac{n_s(\omega)-2.43}{n_s(\omega)+2.43}\right|^2$. Instead of this we are interested in the absolute reflectivity, $R_s(\omega) = \left|\frac{n_s(\omega)-1}{n_s(\omega)+1}\right|^2$. In order to directly calculate R_s one has to know the complex n_s. Although only the real quantity, $R_{s/d}$ is measured one can determine R_s in a iterative way starting with a reasonable initial form of the real (or the imaginary) part of $n_s(\omega)$. The steps of the iteration are:

1. calculate the imaginary (or the real) part of $n_s(\omega)$ by Kramers-Kronig transformation,

2. evaluate $R_{s/d}(\omega)$ and compare it to the measured value,

3. change the real (or the imaginary) part of $n_s(\omega)$ to minimize the difference.

The iteration has to be continued till $R_{s/d}(\omega)$ is approached in a suitable manner. From the resulting $n_s(\omega)$ both reflectivity and conductivity can be directly calculated.

For the proper measurement both the sample and the reference mirror have to be in the focus when the signal is recorded. However, in the present case this criterion is cannot be held since the front and the back surface are separated by the 2 mm long diamond. The enhancement of the spotsize due to the out-of -focus position is shown in Fig. 3.12:

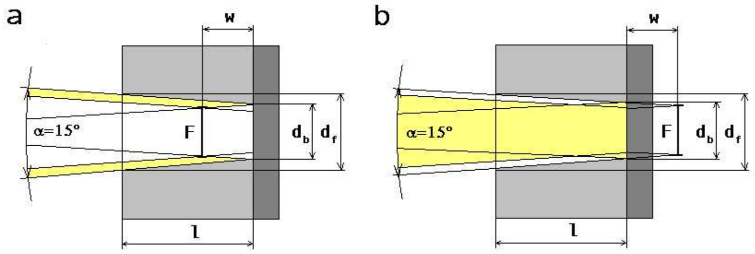

Figure 3.12: *The enlargement of the spotsize on the two reflecting surfaces due to the out-of-focus position. Left panel / right panel: the focus is between / behind the two boundaries.*

The angles and distances in the drawing describe the situation in vacuum but it applies for the diamond, as well. Though the large value of diamond refractive index results in a considerable decrease of the solid angle of the incident beam, it also increases the optical path and these two effects exactly compensate each other. The enhanced spotsize on the front and back surface is $d_f = F + (l + w) \cdot \tan\alpha$ and $d_b = F + w \cdot \tan\alpha$, respectively. The best alignment is when the focus is situated on the back face, in our case it corresponds to $D = d_f - F \approx 0.5\,\mathrm{mm}$ increase of the front reflection diameter. Thus, the spotsize has to be decreased below 1 mm by the adjustment of the first blende. In spite of the reduced beam diameter some misalignments could still lead to some reflection from the wall of the cone. This divergent contribution is cut off by the second blende having the same aperture size as the first one.

The experimental method presented above for the FIR reflectivity measurements under pressure with the application of diamond reference is somewhat idealistic. Further complications due to the liquid pressure medium (forming a thin layer between the diamond and the sample) and small change in the sample position (caused by thermal expansion) will be discussed in Chapter 8.

The measurement of the reflectivity of a crystal both relative to the vacuum and a well-known material could be a way to avoid of the Kramers-Kronig transformation. Thus, the use of a diamond reference can have a further application beyond the high pressure experiments. For the details of the method see Chapter 7.

Chapter 4

Experimental results and analysis

The experimental investigation of $BaVS_3$ has been performed in a strong research collaboration between my home laboratory under the supervision of Prof. György Mihály and Prof. László Forró's group at the EPFL. The transport measurements (resistivity and thermoelectric power) have been done in these two laboratories. The optical conductivity results have been obtained in cooperation with Prof. László Mihály in Brookhaven.

4.1 Electrical conductivity and its anisotropy

4.1.1 Ambient pressure data

The transport properties can be used to qualify $BaVS_3$ crystals. The characteristic properties of a stoichiometric $BaVS_3$ are observable in the resistivity curve of Fig. 4.1.[1] At room temperature it has a very high but metallic like resistivity which is about 35 times larger than that of the vanadium metal. It decreases almost 20% down to 140 K where it reaches a minimum and has an upturn ($d\rho/dT$ becomes negative) inside of the metallic phase. It increases up to the double of its room temperature value before going through a metal to insulator transition at $T_{MI} = 70\,\mathrm{K}$. The transition temperature is defined by the position of the sharp peak in the logarithmic derivative of the resistivity as shown for various pressure

---

[1] As a convention, a label at the top right corner of the graphs will identify the samples on which the measurements were performed.

in Fig. 4.3. The weak change of the slope at $T_s = 250\,\mathrm{K}$ indicates the onset of the structural transition. The metal-insulator transition is accompanied with a dramatic enhancement of the resistivity which changes nine order of magnitude between 70 K and 20 K.

Besides the chain (c-axis) direction, we have also measured the conductivity in the perpendicular plane ($a-b$ plane) by Montgomery method. The $c-a$ anisotropy is $\sigma_c/\sigma_a \approx 3.4$ in the metallic phase and only slightly increases in the insulating state as indicated in the lower panel of Fig. 4.1. Inside of the $a-b$ plane the conduction is isotropic.

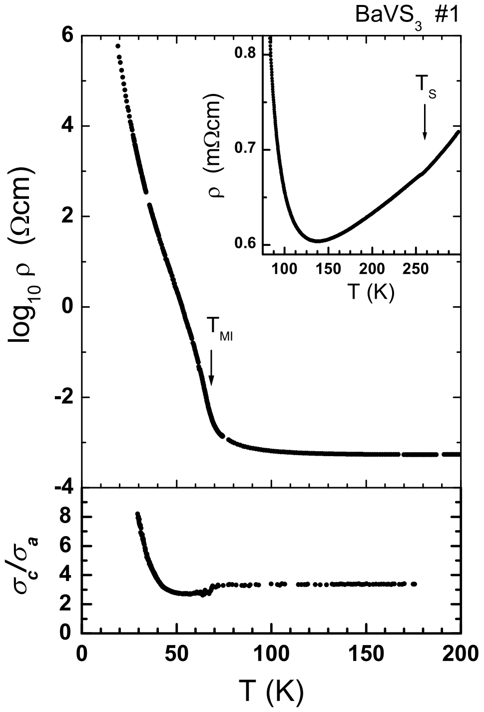

Figure 4.1: *Upper panel: the logarithmic plot of the c-axis resistivity of* $BaVS_3$*. The linear plot of the inset focuses on the metallic phase. Lower panel: the temperature dependence of the* $c-a$ *conduction anisotropy.*

Over the range previously investigated by numerous groups we have extended the resistivity measurements up to 700 K. The high-temperature part is nearly linear but the resulting zero temperature intersection is very high with the value of $R_{T=0K} \approx 0.4\,\mathrm{m\Omega cm}$.

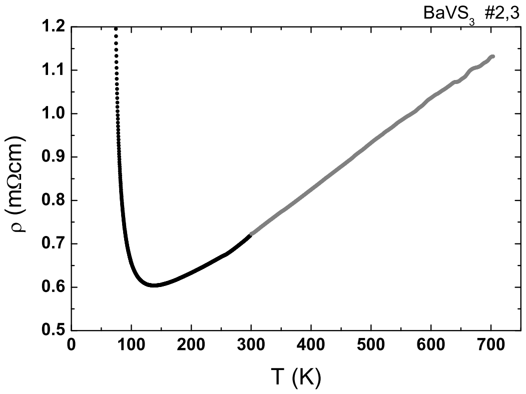

Figure 4.2: *The resistivity of $BaVS_3$ in a range extended far above room temperature.*

4.1.2 High-pressure data

The metal-insulator transition is very sensitive to the applied pressure. The higher is the pressure the metallic phase is more and more extended and the insulator is suppressed. The resistivity minimum is also shifted towards low temperatures and the anomalous metallic range (where $d\rho/dT < 0$) becomes narrower. Above a critical pressure, $p_{cr} \approx 21\,\text{kbar}$ the metal is stabilized over the whole temperature range. All these features can be followed in Fig. 4.3. Concerning the room temperature behaviour the resistivity shows gradual decrease with a diminishing rate towards higher pressures and with a total change of $\sim 25\%$ at $p = 22\,\text{kbar}$ but without any signs of pressure induced transition (see Fig. 4.4). The $c - a$ anisotropy, measured in a smaller range of pressure, decreases 30% under 10 kbar.

The evolution of the metal-insulator phase boundary can be quantitatively derived from the resistivity curves. The transition temperature is identified with the sharp peak in the logarithmic derivative as it is presented in Fig. 4.5.

The Arrhenius plot in Fig. 4.6 gives further insight into the nature of the insulating state. The resistivity is activated-like and roughly follows the form of $\rho(T) = \rho_0\, exp(\frac{\Delta_{ch}}{2k_BT})$.[2] Under hydrostatic pressure the charge gap is suppressed. The ratio, $\Delta_{ch}/k_BT_{MI} \approx 10$ is unusually large and pressure independent. Although $BaVS_3\#2$ was studied in finer steps of the pressure, $BaVS_3\#1$ was found to be cleaner in the sense that its resistivity did not show any kind of saturation at

---

[2] In our notation Δ_{ch} is the full energy separating the conduction and the valence band.

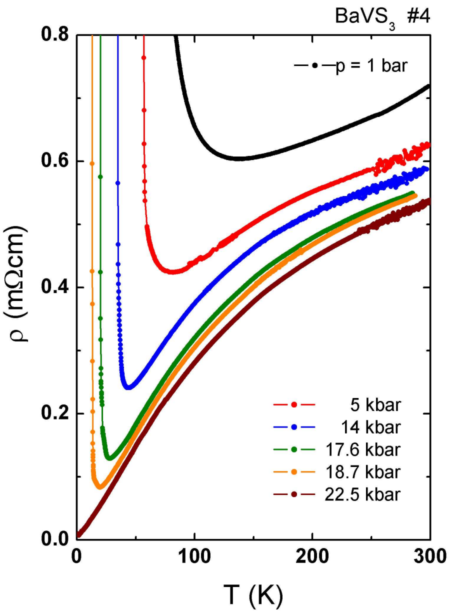

Figure 4.3: *The resistivity in the metallic phase of $BaVS_3$ under various pressures.*

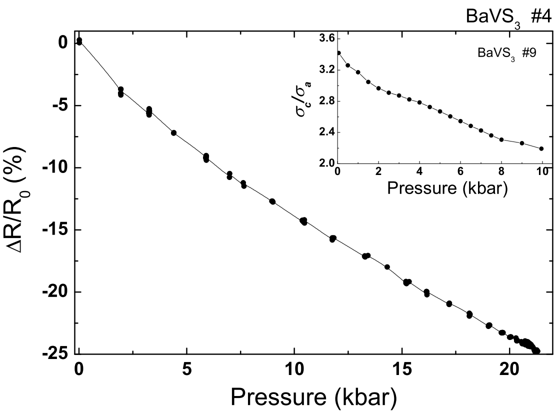

Figure 4.4: *The pressure dependence of the relative change of the resistivity at room temperature strictly reproducible from sample to sample. The inset shows the pressure dependence of the anisotropy in a smaller range of pressure.*

low temperatures related to impurity conduction. We used this sample to derive the value of the charge gap.

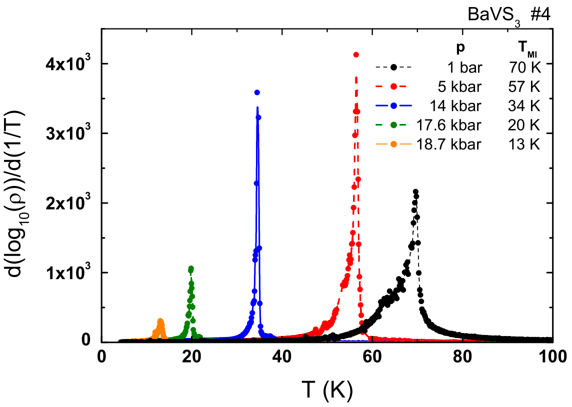

Figure 4.5: *Logarithmic derivative of the resistivity under different hydrostatic pressures.*

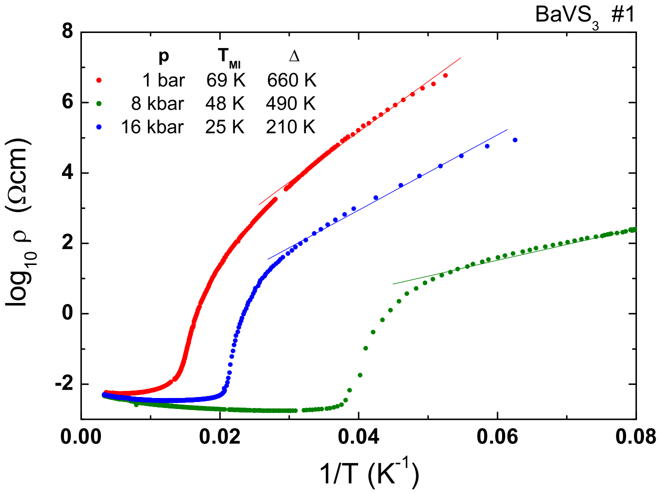

Figure 4.6: *The resistivity in the insulating phase of BaVS$_3$ under different pressures.*

4.2 Thermoelectric power

4.2.1 Ambient pressure data

In most cases, during the investigation of thermoelectric power the resistivity of the samples were simultaneously measured. Thus, the results have been obtained on qualified crystals. The overall behaviour of the TEP (shown in Fig. 4.7) between $T = 70\,\mathrm{K}$ and $670\,\mathrm{K}$ is characteristic of a metal with dominantly electron-like charge carriers. However, its absolute value ($S \approx 25\mu\,\mathrm{V/K}$ at room temperature) is remarkably higher than that of ordinary metals ($S_{Au} \approx 2\mu\,\mathrm{V/K}$, $S_{Ag} \approx 1.5\mu\,\mathrm{V/K}$ and $S_{Cu} \approx 1.8\mu\,\mathrm{V/K}$). Some anomaly is observable in the TEP around 150 K where the minimum appears in the resistivity. At the metal to insulator transition the Seebeck coefficient radically drops to zero and changes sign.

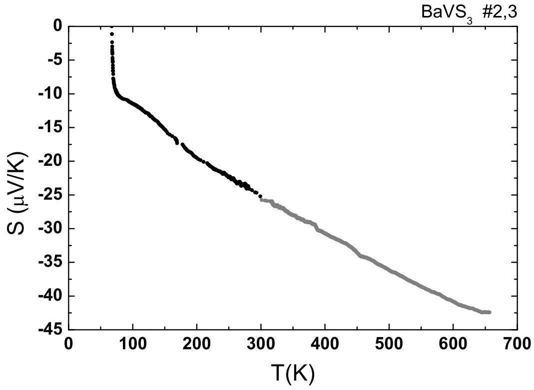

Figure 4.7: *The thermoelectric power of BaVS$_3$ in an wide range of temperature.*

4.2.2 High-pressure data

In agreement with the pressure induced enhancement of the conductivity the decrease of the TEP with increasing pressure also suggests the strengthening of the metallic character. This tendency can be followed in Fig. 4.8 where a representative set of the data are shown. The transition temperature, in this case simply identified with the temperature where the curves change sign, is gradually shifted to lower temperatures as the pressure is increased and finally suppressed above $p_c \approx 21\,\mathrm{kbar}$.

An uncertainty in the absolute value of resistivity has no effect on the gap value derived from the Arrhenius plot. In contrast, the Seebeck coefficient of an intrinsic semiconductor is proportional to the gap:

$$S(T) = \frac{k_B}{e} \cdot \frac{\mu_e - \mu_h}{\mu_e + \mu_h} \frac{\Delta_{ch}}{2k_BT} = \frac{k_B}{e} \cdot \frac{\Delta_{TEP}}{2k_BT} \quad , \tag{4.1}$$

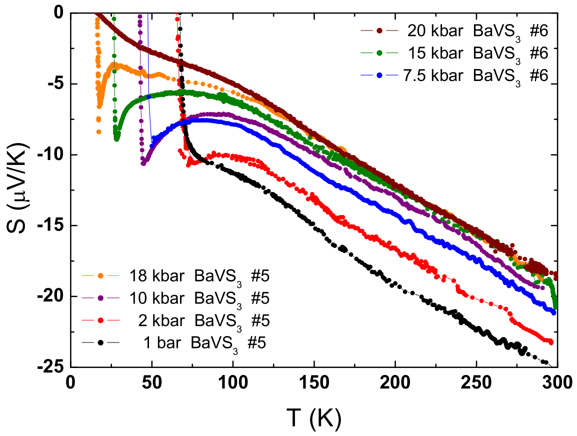

Figure 4.8: *Representative set of the thermoelectric power in the metallic phase of $BaVS_3$ under various pressures.*

where μ is the mobility. Thus a systematic error of the absolute value is transmitted from one to the other. The relative change of the TEP as a function of pressure (Fig. 4.9) is identical for all the samples, thus in order to reduce the systematic error in the absolute values we normalized the TEP of the samples at room temperature to the value obtained from the measurements performed in vacuum (see 3.3).

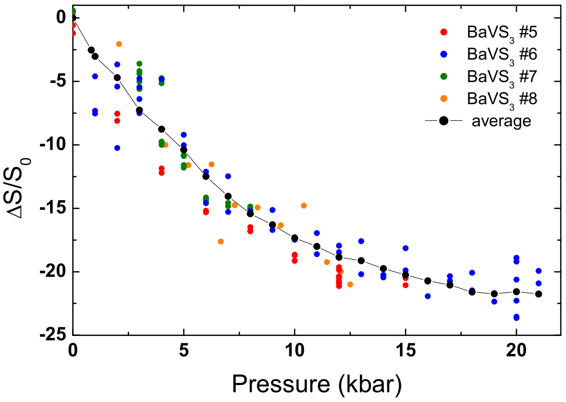

Figure 4.9: *The pressure dependence of the relative change of the thermoelectric power at room temperature for four different samples.*

According to Eq. 4.1 the TEP of a semiconductor is expected to be inversely proportional to the temperature. In our case it is valid only in a limited range of temperature at every pressure as it is visible in Fig. 4.10. (These intervals are: 65 − 44 K, 62 − 44 K, 48 − 37 K, 42 − 28 K, 27 − 20 K and 17 − 13 K for 1 bar, 2 kbar, 7.5 kbar, 10 kbar, 15 kbar and 18 kbar, respectively. Their width are all around $T_{MI}/4$.) These regions are satisfactorily wide to determine the gap value by linear fits. In contrast to the resistivity, which only sensitive to the numbers of thermally excited carriers, the Seebeck coefficient has opposite sign for electrons and holes. Therefore the gap detected by the two methods may differ and that one obtained from thermoelectric power can be necessarily smaller: $\Delta_{TEP} = \frac{\mu_e - \mu_h}{\mu_e + \mu_h} \Delta_{ch}$. However, we found that $\Delta_{TEP} \approx 2\Delta_{ch}$ which cannot be explained in the simple approach of semiconductors. In the following we consider only the pressure dependence of Δ_{TEP} and normalize its absolute value to the gap derived from resistivity measurements. (We will see in 5.2 that the gap values obtained from resistivity and optical conductivity are in agreement with each other.)

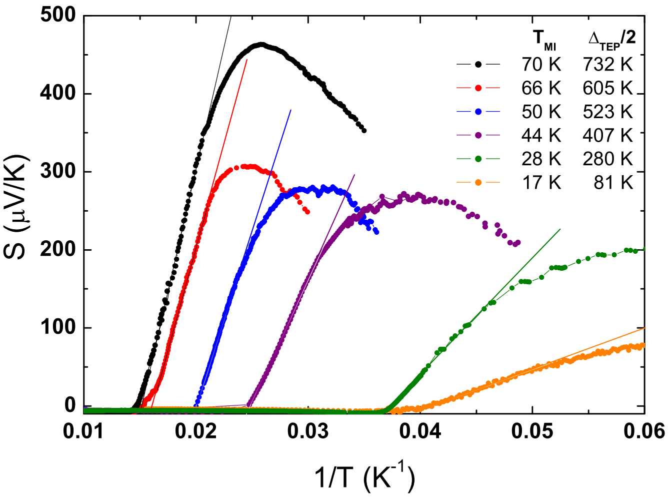

Figure 4.10: *The thermoelectric power in the insulating phase of* $BaVS_3$ *under different pressures. Notice that the* $p = 18$ *kbar graph is shifted to higher temperature by* $0.02\,K^{-1}$.

4.3 Optical conductivity in the infrared region

4.3.1 Ambient pressure data

The frequency dependent reflectivity data are shown in the left part Fig. 4.11. (As it was discussed in details in 3.4.1 in optical reflectivity studies where the wavelength of the light is comparable to the sample size, in the final step of the measurement the crystal has to be in-situ evaporated with gold in order to obtain a good reference. In our experiments this method was necessary below 100 cm^{-1}.) The curves measured at $T = 300$ K and 70 K reflects metallic behaviour at high temperatures: the reflectivity tends $R \rightarrow 1$ approaching zero frequency. At low frequencies these curves were extrapolated by the Hagen-Rubens law characteristic of metals:

$$R \approx 1 - 2\sqrt{\frac{2\epsilon_0\omega(s^{-1})}{\sigma_0}} = 1 - 2\sqrt{\frac{4\pi\omega(cm^{-1})}{Z_0\sigma_0}} \quad , \tag{4.2}$$

where $Z_0 = 377\Omega$ is the so called surface impedance and $\sigma_0 = \sigma(\omega \rightarrow 0)$. The fits fairly follow the overall shape of the curves apart from some local features like the small phonon peak at 100 cm^{-1} and the minimum around 30 cm^{-1}. (Notice, that the frequency scale is logarithmic which enlarges the low-frequency part. The reflectivity has to approach 1 infinitely far for the same reason.) The dc conductivity values obtained from the fits are $\sigma_0 = 710\,\Omega^{-1}\mathrm{cm}^{-1}$ and $\sigma_0 = 370\,\Omega^{-1}\mathrm{cm}^{-1}$ for $T = 300$ K and 70 K, respectively. It is to be noted that the polarization of the synchrotron light was arbitrary relative to the crystallographic directions, and since there is a conduction anisotropy of ($\sigma_c/\sigma_a \approx 3.4$), the above absolute values are uncertain within a factor of 3. These have to be compared to the results of the dc transport experiments measured along the chain direction: $\sigma_{dc} = 1400\,\Omega^{-1}\mathrm{cm}^{-1}$ at room temperature and $\sigma_{dc} = 700\,\Omega^{-1}\mathrm{cm}^{-1}$ just above the transition.

In the insulating phase the low-frequency reflectivity is constant and due to the vanishing electronic background the phonons sharpen out. The dominant one appears at 100 cm^{-1} but a series of smaller ones can be also recognized below 400 cm^{-1}, especially in the lowest temperature curve as indicated by arrows. Towards higher frequencies the difference between the metal and the insulator disappears and above 700 cm^{-1} all the graphs essentially go together. After the adequate low-frequency extrapolation of the reflectivity curves (Hagen-Rubens law for the metal and $R(\omega \to 0) = constant$ for the insulator), the frequency dependent conductivities were calculated by Kramers-Kronig transformation. The results are presented in the right plot of Fig. 4.11. The most remarkable observation is the complete suppression of the low-frequency spectral weight, i.e. the presence of a gap in case of the $T = 60$ K and 10 K curves. This is a direct evidence for the metal-insulator transition. Following a gradual increase the conductivity reaches a maximum at a frequency $\sim 530\,\mathrm{cm}^{-1}$ which assigns the value of the gap found to be $\Delta_{ch} = 530 cm^{-1} = 750$ K for both temperatures. (A maximum around 350 cm^{-1} may be disturbing but it is related to a sharp phonon peak.)

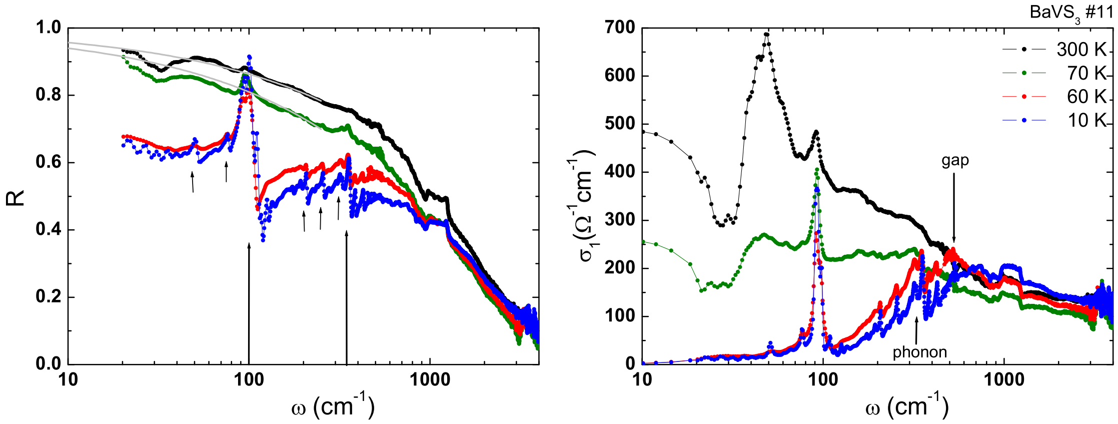

Figure 4.11: *Left panel: Infrared reflectivity of $BaVS_3$ at four different temperatures. The grey lines are the Hugen-Rubens extrapolations of the metallic curves and the arrows indicate the phonons. Right panel: Infrared conductivity of $BaVS_3$ at the same temperatures.*

4.3.2 High-pressure data

We have investigated the IR optical conductivity of $\mathrm{BaVS_3}$ up to $p = 26$ kbar. A typical set of reflectivity data measured above and below the phase transition is shown in Fig. 4.12. There is a large frequency dependent background superimposed on the data, which indicates that in spite of the application of wedged diamond window some kind of interferences still remains. The source of the interference and the procedure of its elimination from the data are discussed in details in Chapter 8. Despite the large baseline the opening of the gap below about 300 cm^{-1} spectrum.

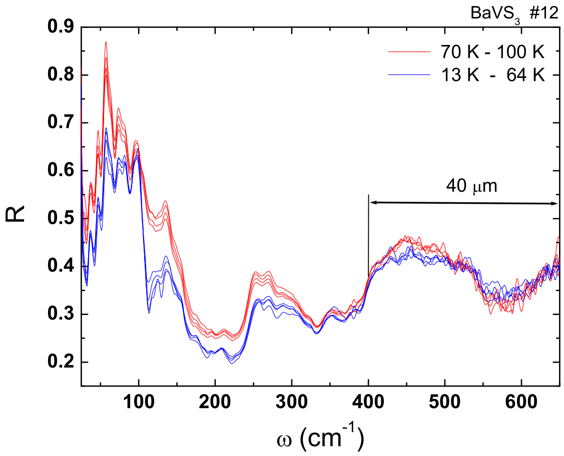

Figure 4.12: *FIR optical reflectivity of a BaVS$_3$ sample embedded in the pressure cell. The two stacks of red and blue curves are measured at various temperatures in the metallic and insulating phase, respectively. Each curve is affected by an interference related oscillation.*

Fortunately, after the elimination of the interference, the basic information of the reflectivity curves are preserved at each pressure. Fig. 4.13 shows the collection of the reflectivity results together with the conductivity curves obtained by Kramers-Kronig transformation.

The conductivity curves reflect that the region where no spectral weight is present, is shifted to lower frequencies as the pressure is increased. However, even after the baseline subtraction some oscillation is still superposed on the reflectivity curves. We smoothed out the oscillation in the reflectivity by interpolation. Fig. 4.14 shows the smoothed reflectivity together with its Kramers-Kronig transform for the data set shown in Fig. 4.12. This procedure supplies reasonable results and allows the determination of the pressure dependence of the gap. The frequencies at which the gap opens are labelled with circles on each curve of Fig. 4.15.

The raw data presented in Fig. 4.12 shows that there is no measurable difference between the reflectivity curves recorded in the insulating phase at different temperatures. This is in good agreement with the ambient pressure results where

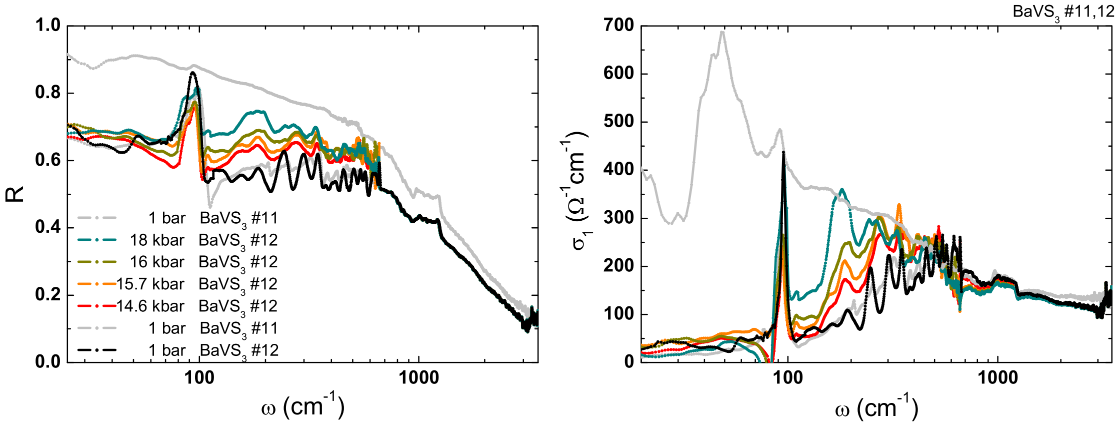

Figure 4.13: *Left panel: Reflectivity in the insulator phase of $BaVS_3$ at five different pressures. The grey lines indicate the ambient pressure data at $T = 300\,K$ and $60\,K$ previously shown in Fig. 4.11. Right panel: Conductivity of $BaVS_3$ at the same pressures.*

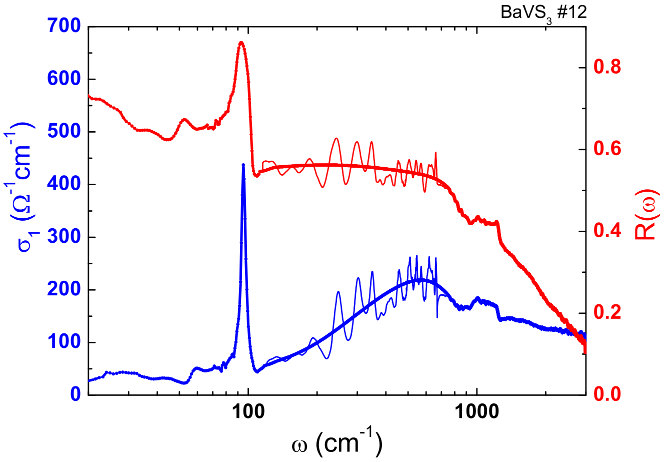

Figure 4.14: *The raw and smoothed curves of reflectivity together with their Kramers-Kronig transformed parts in the insulator phase.*

the reflectivity was found to be roughly the same at $T = 60\,\mathrm{K}$ and $10\,\mathrm{K}$ resulting in the same gap value. It is also supported by the detailed analysis for the in-cell ambient pressure data where the reflectivity is measured in fine steps of the temperature (see Fig. 4.16).

As it is seen in the figure the opening of the gap is accompanied by the sharpening of the dominant phonon in the insulating phase.

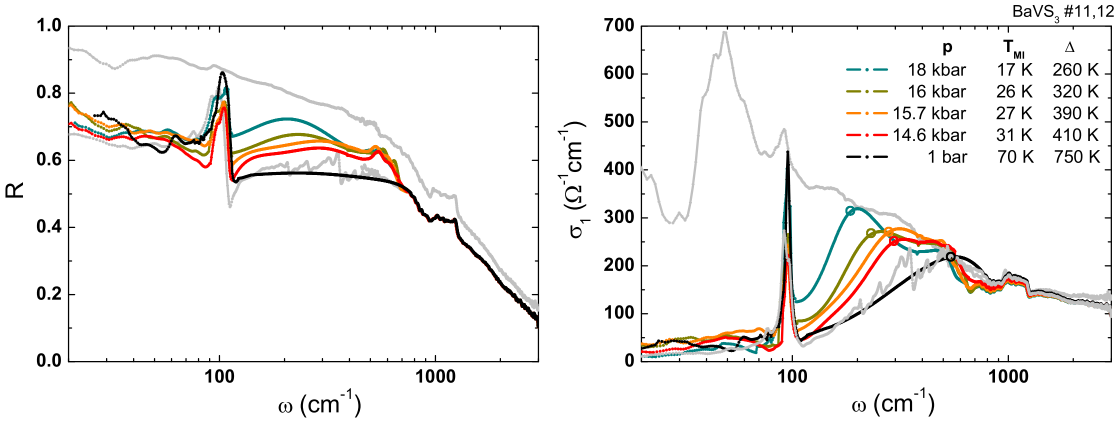

Figure 4.15: *Left panel: The smoothed reflectivity in the insulator phase of BaVS*$_3$ *at five different pressures. The grey lines indicate the ambient pressure data at* $T = 300\,K$ *and* $60\,K$*. Right panel: Conductivity of BaVS*$_3$ *at the same pressures.*

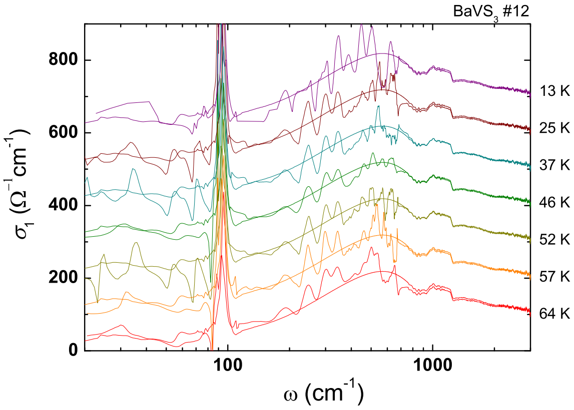

Figure 4.16: *The conductivity of the insulating phase with the smooth curve obtained for the* $T = 64\,K$ *data at several temperatures.*

Summarizing the results, we observed a sudden jump in the low-frequency part of the spectra at the transition temperature at all pressures investigated. At the highest pressure of our investigation, $p = 26\,\mathrm{kbar}$, neither the opening of the gap nor the sharpening of the phonon peak could not be observed indicating that the material remains metallic as expected from the transport studies.

4.4 Magnetotransport experiments under pressure

4.4.1 Shifting of the transition by magnetic field

We have already realized that the metal-insulator transition is quite sensitive to the applied hydrostatic pressure. Since the transition has magnetic character (as mentioned in Chapter 2) the question emerges whether the transition temperature can be equally suppressed by the magnetic field. It turns out that even a magnetic field as high as 12 T acts on a much smaller energy scale. The transition is suppressed only with $\Delta T_{MI} \approx 0.35\,\mathrm{K}$ in 12 T. We can also combine the application of pressure and magnetic field. The effect is somewhat stronger under pressure: $\Delta T_{MI} \approx 0.53, 0.7, 0.83$ and $0.9\,\mathrm{K}$ at $p = 1.4, 7.5, 12$ and 15 kbar, respectively (see Fig. 4.17). The temperature of the zero field transitions in the same order are $T_{MI} = 70, 66, 49, 39$ and 32 K.

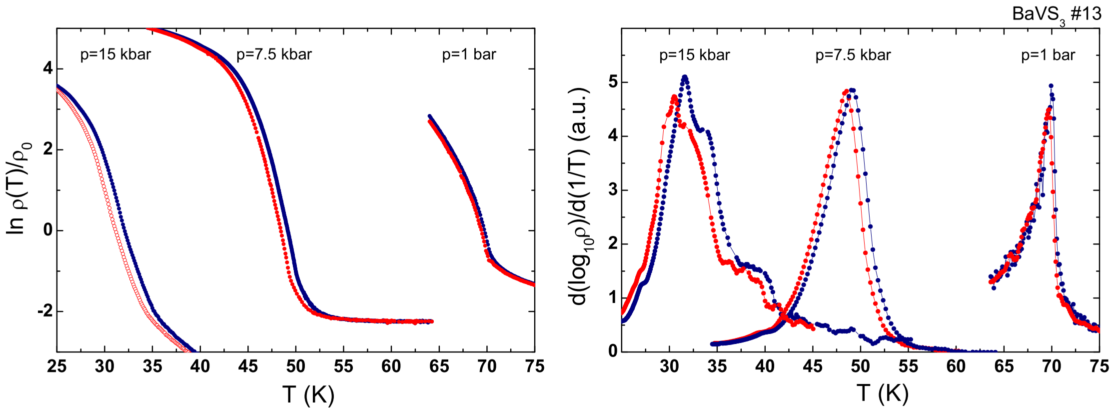

Figure 4.17: *Left side: The normalized logarithmic plot of the resistivity. The red curves, measured in 12 T, are shifted due to the magnetic field with* $\Delta T_{MI} = 0.35, 0.7, 0.9$ *K relative to the zero field ones for* $p = 1bar, 7.5kbar, 15\,kbar$*, respectively. Right side: The logarithmic derivative of the same resistivity curves with sharp peak at the phase transition.*

One can make another observation: the shape of the resistivity in a wide range of the transition is the same either with or without applied magnetic field, i.e. the 12 T curves are the shifted counterparts of the zero field ones. The other way of the investigation is the measurement the field dependence of the resistivity at various temperatures. The magnetoresistance is very weak, under the limit of detection at high temperatures (above 140 K) and becomes larger when the transition is approached, as it is evidenced by Fig. 4.18.

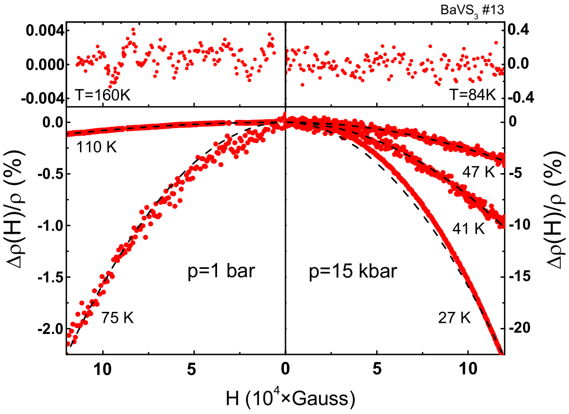

Figure 4.18: *Field dependence of the resistivity at various temperatures under the lowest and the highest pressure of the above set.*

Furthermore, it follows a purely quadratic behaviour, namely $\Delta\rho/\rho = -\alpha(T)H^2$.

In the 12 T measurements we have found that the magnetic field does not play any other role than the suppression of the transition, which results in a shift of the whole resistivity curve in the vicinity of the transition. It is a plausible assumption that any smaller field acts on the resistivity in the same way. If the resistivity depends on the magnetic field only through the transition temperature the following relation holds:

$$\rho(T, H, p) = \rho([T - T_{MI}(H, p)], p) \tag{4.3}$$

for fields up to $H_{max} = 120\,\mathrm{kG}$. The relation $\rho(T, H) = \rho[T - T_{MI}(H)]$ means that changing the magnetic field at $T = T_0$ from zero to H_0 is equivalent to the motion on $\rho(T, H = 0)$ curve from T_0 to $T_0 - \Delta T_{MI}(H_0)$. We notice it here that the changes in the transition temperature derived from the logarithmic derivatives are the same which are needed to move the resistivity curves to fit on each other. After considering the power series expansion of $\rho(T, H, p)$ at a given pressure:

$$\frac{\Delta\rho(T,H)}{\rho(T)} = \frac{1}{\rho(T)} \sum_{1}^{\infty} \frac{(-1)^n}{n!} \frac{\partial^n \rho(T)}{\partial T^n} \Delta T_{MI}^n(H) \quad , \tag{4.4}$$

a more accurate analysis can be performed. This is shown in Fig. 4.19 where $\Delta\rho(T, H_{max})/\rho(T)$ and Eq. 4.4 till second order are simultaneously plotted. For each pressure the former is simply obtained from the temperature dependence measured in H_{max} and in zero field while the latter is calculated using the zero field temperature dependence and the value of $\Delta T_{MI}(H_{max})$ determined by the logarithmic derivatives. Their correspondence is obvious.

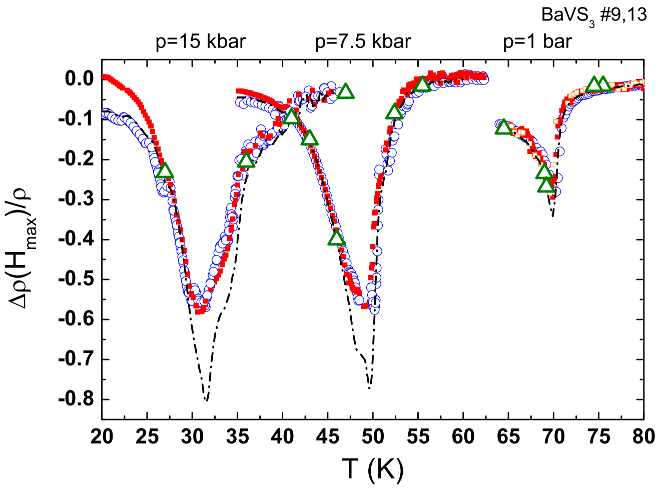

Figure 4.19: *Analysis of the temperature dependence of the relative magnetoresistance at three pressures: the directly measured* $\Delta\rho(H_{max})/\rho$ *(red curve for* $BaVS_3\#13$ *and orange for* $BaVS_3\#9$*), the results of the field sweeps (green open triangles) and the calculated* $\Delta\rho(H_{max})/\rho$ *in first and second order of* $\Delta T_{MI}(H_{max})$ *(dash dotted line and blue curve, respectively).*

The first order expansion (plotted in Fig. 4.19, too) also gives a good approximation except in the narrow vicinity of the transition. In the region where the first order approximation is valid (i.e. $\frac{\Delta\rho(T,H)}{\rho(T)} = -\frac{1}{\rho(T)}\frac{\partial\rho(T)}{\partial T}\Delta T_{MI}$) the field dependence of the transition shift is simply proportional to the field dependence of the magnetoresistance which was found to be quadratic at every temperature. Thus, the relative shift of the transition has the following form:

$$\frac{\Delta T_{MI}(H)}{T_{MI}} = \frac{\alpha(T)}{T_{MI}\frac{\partial ln\rho(T)}{\partial T}}H^2 = -\beta H^2 \quad . \tag{4.5}$$

While β is directly obtained from the measured transition temperature shifts, the analysis of the field dependencies supplies the value of α, and β can be calculated from them, too. The pressure dependence of the coefficients is given in Fig. 4.20.

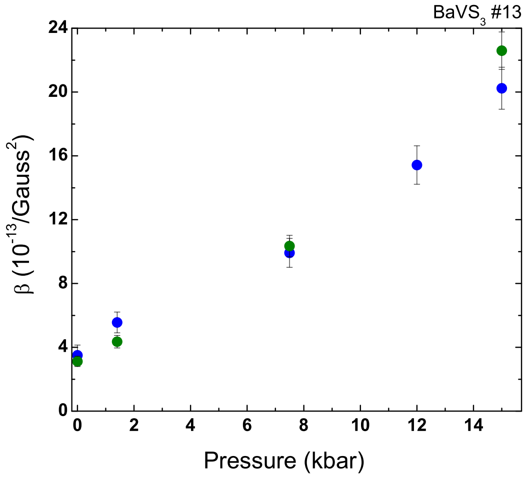

Figure 4.20: *The value of the coefficient β at five pressures. The blue symbols indicate the results obtained from the transition temperature shift in* 12 T *while the green symbols are the average of the results obtained from the field sweeps.*

The results presented above are mainly based on the transversal magnetoresistance in the chain direction (with the current flowing parallel and magnetic field pointing perpendicular to the c-axis). At ambient pressure the anisotropy of the magnetoresistance was also tested on $BaVS_3\#9$. The temperature dependence of the a direction magnetoresistance (also in perpendicular field) is also plotted in Fig. 4.19. Since the magnetoresistance is fully related to the shift of the transition we expect it to be isotropic, as it has been experimentally found.

4.4.2 Magnetoresistance in the low-temperature pressure induced metallic phase

We have found that the pressure is convenient for the coarse suppression of the metal to insulator transition while with the magnetic field we can do the fine tuning. Our purpose is to shift T_{MI} by pressure to such a low temperature that the transition can be completely suppressed by fields lower than 12 T. The Arrhenius plot in Fig. 4.21 shows the resistivity under the required circumstances. At 19.1 kbar the insulating phase is completely suppressed by a field between 4 T and 8 T. The metallic behaviour in case of $B = 8\,\mathrm{T}$ and 12 T is demonstrated in the linear plot of the inset.

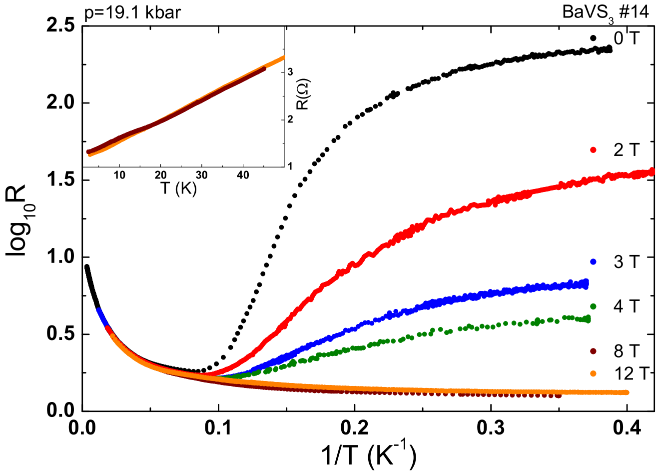

Figure 4.21: *The Arrhenius plot of the resistivity in various magnetic fields under 19.1 kbar. The inset focuses on the high-field metallic curves.*

For the $0 - 4\,\mathrm{T}$ graphs T_{MI} can be determined by the logarithmic derivative. The peak in the derivatives is diminished and gradually smeared out with increasing field as shown in Fig. 4.22.

The onset of a magnetic field induced transition is also evidenced by the magnetoresistance data measured at low temperatures. At $T = 2.6\,\mathrm{K}$ the resistivity, after a 99% drop, reaches its metallic value around $B = 6.5\,\mathrm{T}$ (see Fig. 4.23). The same can be noticed in case of the field dependence measured at $T = 4.2\,\mathrm{K}$, although the change is “only” 93% due to the lower initial value of the resistivity in the insulating phase. We have a not so dramatic but still remarkable magnetoresistance at least up to 30 K.

In order to determine the critical magnetic field where the transition takes place, we further analyze the magnetoresistance curves measured at $T = 2.6\,\mathrm{K}$. In Fig. 4.24 $\Delta R/R \cdot B$ is plotted to enlarge the high-field behaviour. It shows that

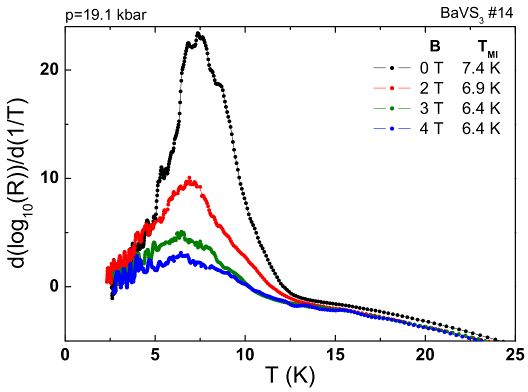

Figure 4.22: *The logarithmic derivative of the resistivity for four different fields:* $B = 0, 2, 3$ *and* $4\,T$.

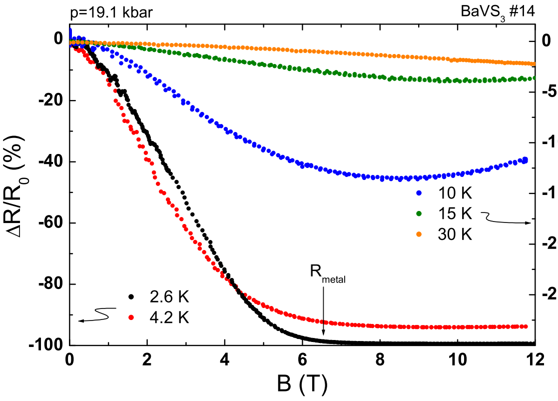

Figure 4.23: *The field dependence of the resistivity. The left scale corresponds to the data measured at* $T = 2.6\,K$ *and* $4.2\,K$ *while the right scale to the higher temperature data. The arrow indicates the field value the sample is already inside of the metallic phase.*

following a radical decrease of the resistivity, there is a break around $B = 5.8\,\mathrm{T}$ and then is saturates at the metallic value. We assign this break with the transition.

Till now, the dominant role of the magnetic field was the moving of the phase boundary. Therefore, we have not got insight into the effect of magnetic field on the scattering processes in the low-temperature metallic phase. If we stabilize the metal solely by pressure but also take care of staying in a close vicinity of the critical pressure, $p_{cr} \approx 21\,\mathrm{kbar}$, the magnetoresistnace will provide information about the scattering mechanism. Fig. 4.25 shows the competition of a negative and

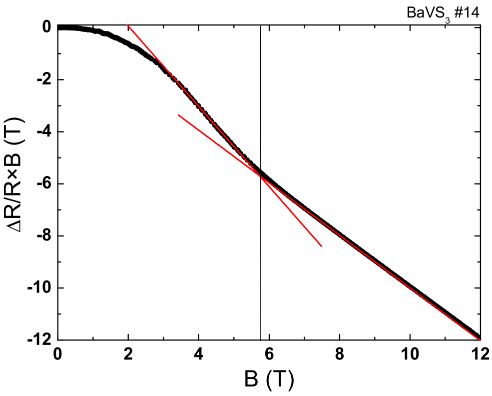

Figure 4.24: $\Delta R/R \cdot B$ *vs.* B *at* 2.6 *K. The break of the slope indicate a field induced transition, which occurs at* $B_c \approx 5.8$ *T.*

a positive term. Both of them gradually weaken as the temperature is increased and only the negative term survives above ~ 30 K. (The systematic error due to the magnetoresistance of the thermometer is lower than 0.4%.)

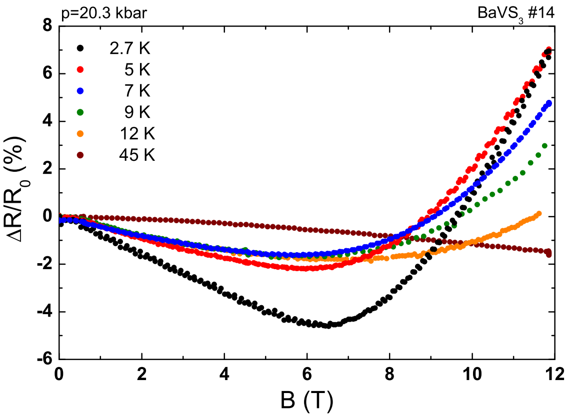

Figure 4.25: *The field dependence of the resistivity studied in a wide range of temperature.*

The large positive term appears in the same region where the zero field resistivity can be characterized by the power-law temperature dependence. This is shown in Fig. 4.26 by the double logarithmic plot of the temperature dependent resistivity measured at $p = 20.3$ kbar. The data obtained for $BaVS_3\#4$ at a slightly higher pressure, $p = 22.5$ kbar, is also presented. A power-law behaviour with an exponent, $n \approx 1.25$ is observed between 1.2 K and 40 K.

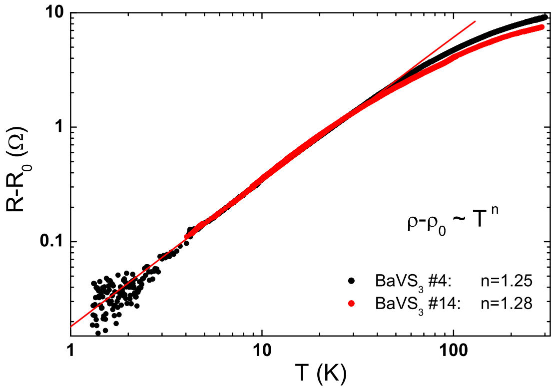

Figure 4.26: *The double logarithmic plot of the resistance of two samples. The residual resistance is subtracted in both cases.*

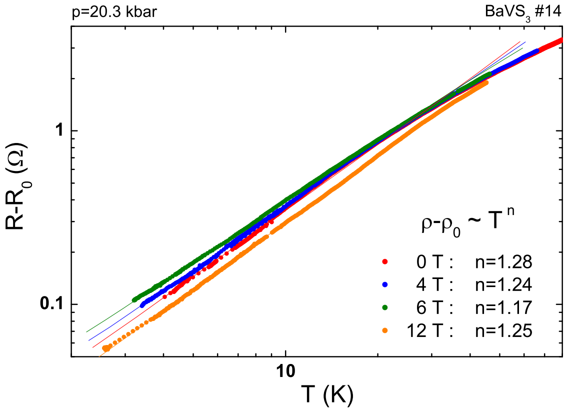

Figure 4.27: *Double logarithmic plot of the resistance for different fields. The residual resistance is subtracted in each case.*

Finally, we present the resistivity data measured in various constant magnetic fields ($B = 4, 6, 12\,\mathrm{T}$) in the same interval of temperature. After the subtraction of the residual resistance each of them follows a power-law behaviour with an exponent around $n = 1.2$. The residual resistance subtracted is slightly field dependent, it varies within 7%.

Chapter 5

Discussion

5.1 Nature of the metal-insulator transition

From phenomenologic aspect the $T_{MI} = 70\,\mathrm{K}$ phase transition is well specified: a transition from a high-temperature paramagnetic metal to a low-temperature non-magnetic insulator, which is accompanied by the significant freezing out of the spin degrees of freedom in the low-temperature state. However, there is no microscopic description for the phase transition and the ordinary order parameters are ruled out by the experiments. Based on a phase boundary analysis we point out that the transition is of second order.

The shift of the transition temperature in presence of magnetic field was found to be negative. The onset of an antiferromagnetic order below T_{MI} is not supported by the experiments instead the development of a spin gap, Δ_s was detected either by NMR or neutron scattering measurements. The magnetic field acts through the $\chi H^2/2$ term of the free energy. Since we have a large Curie-susceptibility in the metal, while the magnetic excitations are gapped in the insulator, the low-temperature phase is suppressed by the application of magnetic field. The $H-T$ phase boundary has quadratic shape in moderate magnetic fields and for pressures up to 15 kbar as we demonstrated in 4.4.1. Let us recall the form of the $H-T$ phase boundary given by Eq. 4.5:

$$\frac{\Delta T_{MI}(H,p)}{T_{MI}(p)} = -\beta H^2 \quad , \tag{5.1}$$

where β was obtained from magnetoresistance measurements at different pressures. Assuming the above form of the phase boundary is adequate also for higher magnetic fields, one can deduce the critical field ($H_c = 1/\sqrt{\beta}$), which would completely suppress the transition. The high value of the critical field, $H_c \approx 1700\,\mathrm{kG}$ at ambient pressure, is in accordance with the small shift of the transition temperature. Furthermore, the pressure dependence of the critical field scales with that of the transition temperature as it is pointed out in Fig. 5.1.

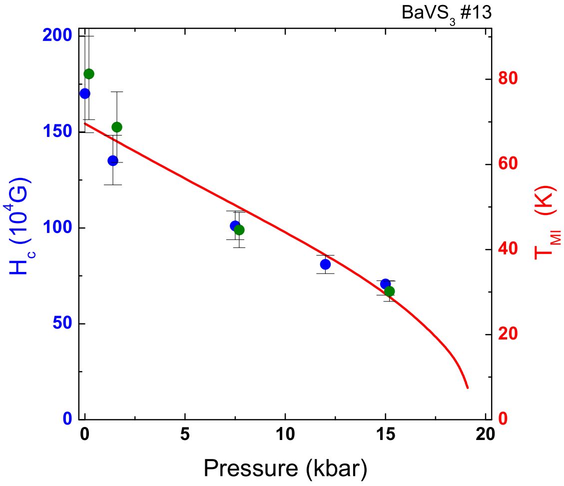

Figure 5.1: *The pressure dependence of* H_c *(blue and green symbols are used in the same sense as in Fig. 4.20). The transition temperature as a function of pressure is also presented.*

If we assume that a singlet-triplet gap has to be bridged over, then $\Delta_s = 2gS\mu_B H_c$ and we can rewrite Eq. 5.1 in a dimensionless form:[1]

$$\frac{\Delta T_{MI}(H,p)}{T_{MI}(p)} = -\left(\frac{2gS\mu_B H}{\Delta_s(p)}\right)^2 \quad . \tag{5.2}$$

The ambient pressure value of the spin gap based on this assumption, $\Delta_s \approx 250\,\mathrm{K}$ is identical with that one obtained from the NMR measurements (Knight shift and T_1 relaxation) of Ref. [8].[2] The spin gap of the insulating state scales with

---

[1] In our notation Δ_s is the entire energy needed for the excitation, not its half. This convention will be followed in case of the charge excitations, too.

[2] On the basis of their neutron scattering experiment the same group reported a single spin excitation energy what they also identified as a spin gap with a rather different value, $\Delta_s \approx$

the transition temperature according to $\Delta_s(p) = \xi \cdot k_B T_{MI}$ with $\xi \approx 3.6$, which is close to the BCS ratio.

Eq. 5.1 can be reformulated in another meaningful way:

$$\frac{\Delta T_{MI}(H,p)}{T_{MI}(p)} = -\gamma \left(\frac{g\mu_B S H}{k_B T_{MI}(p)} \right)^2 \quad . \tag{5.3}$$

The dimensionless constant is be $\gamma = 0.45 \pm 0.04$ and it is independent of pressure since the critical field scales with the transition temperature (see Fig. 5.1). The invariance of γ means that the pressure does not modify the shape of the $H-T$ phase boundary. The same relationship describes the suppression of the transition in spin-Peierls systems by a magnetic field, with very similar value of γ. From theoretical side, it was predicted to be $\gamma = 0.44$ by Bulaevskii et al. [16] and $\gamma = 0.38$ by Cross [17]. Experiments performed later verified that this $H-T$ phase boundary is universal both for organic [18] and inorganic [19] compounds with $\gamma = 0.41 \pm 0.05$.

The lowest order thermodynamic quantity which clearly shows non-analytic behaviour at the transition is the temperature derivative of the susceptibility. It has a large jump at T_{MI} as it is shown in the right panel of Fig. 5.2.

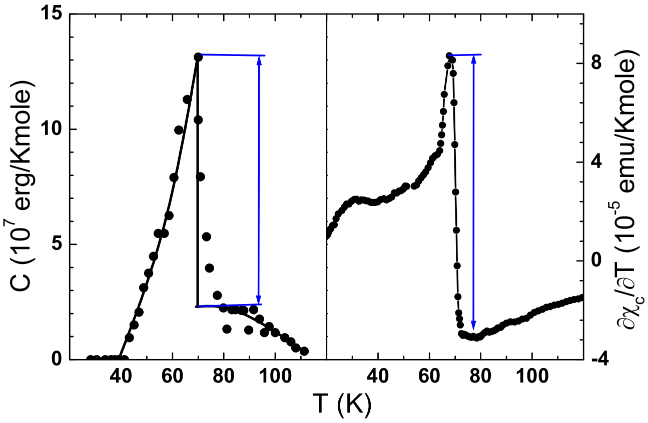

Figure 5.2: *The comparison of the specific heat and the temperature derivative of the susceptibility in the vicinity of* T_{MI} *(based on data taken from [20] and [21], respectively).*

$10 meV = 116\,\mathrm{K}$ [15].

On the basis of general thermodynamical reasoning, for a quadratic shape phase boundary one can obtain the following relationship between the discontinuities belonging to quantities of different order:[3]

$$\Delta\left(\frac{\partial\chi}{\partial T}\right) = \beta\Delta C + \frac{1}{12\beta T_{MI}}\Delta\chi^{(3)} \quad , \tag{5.4}$$

which implies that the jump of $\partial\chi/\partial T$ has to be balanced by that of the specific heat, C and the non-linear susceptibility, $\chi^{(3)}$. The phase boundary parameter, β is introduced in Eq. 5.1. Next we checked the validity of the above relation. Although the specific heat is measured with poorer temperature resolution, it is also suggestive to have a discontinuity as indicated in Fig. 5.2. The value obtained for ΔC is smaller than it could all alone keep the balance ($\beta\Delta C = (0.5\pm 0.1)\Delta(\partial\chi/\partial T)$), thus a fraction of $\Delta(\partial\chi/\partial T)$ has to be matched by $\Delta\chi^{(3)}$. The high-field magnetization data of Ref. [22] show non-linearity only in the metallic phase and the size of the discontinuity in $\chi^{(3)}$ is sufficient to satisfy Eq. 5.4.

Though the strongest indicator of the transition, $\partial\chi/\partial T$, is a third derivative of the free energy, the finite discontinuity of the specific heat in Eq. 5.4 confirms that the transition is of second order. In case of second order transitions a further relation can be derived (Eq. 9.14 in Chapter 9), which contains only the jump of the specific heat and the derivative of the linear susceptibility:

$$\beta\Delta C = \Delta(\partial\chi/\partial T)/2 \quad . \tag{5.5}$$

Though the size of the specific heat discontinuity is a bit ambiguous, our observation is close to satisfy this relation, as shown in Fig. 5.2. The quantities in Eq. 5.5 corresponds to the arrows drawn in the figure with β obtained from an independent experiment (Fig 4.20 ambient pressure).

Besides the $H-T$ phase boundary, the $p-T$ transition line is also known. Thus, one may raise the question whether the same kind of analysis can be carried out in that case, too. The corresponding phase boundary differential equation is the usual Ehrenfest relation:

---

[3] This is a phase boundary differential equation evaluated in the $H=0$, $T=T_{MI}$ point with the notation $\beta = \left.\frac{\partial^2 T_{MI}}{\partial H^2}\right|_{H=0}$. The detailed derivation of the relation is given in Chapter 9.

$$\frac{\partial T_{MI}}{\partial p} = T_{MI} V \frac{\Delta\beta_V}{\Delta C} \quad , \tag{5.6}$$

where β_V is the volume thermal expansion coefficient and V is the volume. Since the above quantities are only measured at ambient pressure, we can make the analysis at $p = 1\,\mathrm{bar}$ similarly to the previous case, where we were restricted to the $H = 0$ point. Using the value of the initial slope, $\partial T_{MI}/\partial p \approx -2.7\,\mathrm{K/kbar}$ and ΔC we would expect $\Delta\beta_V \approx -2.3 \cdot 10^{-5}\,\mathrm{K}^{-1}$. However, for the first sight the thermal expansion coefficient obtained by the derivation of the linear thermal expansion by Ref. [11] shows a high negative peak instead of discontinuity. But if we have a look at the raw data of the thermal expansion and notice that the temperature resolution is only about 2 K, we can state that the presence of the required jump in the derivative cannot be excluded (see Fig. 5.3). In case of susceptibility and specific heat the better temperature resolution makes it easier to judge, since whole jump can be localized in a $2 - 3\,\mathrm{K}$ wide range for both.

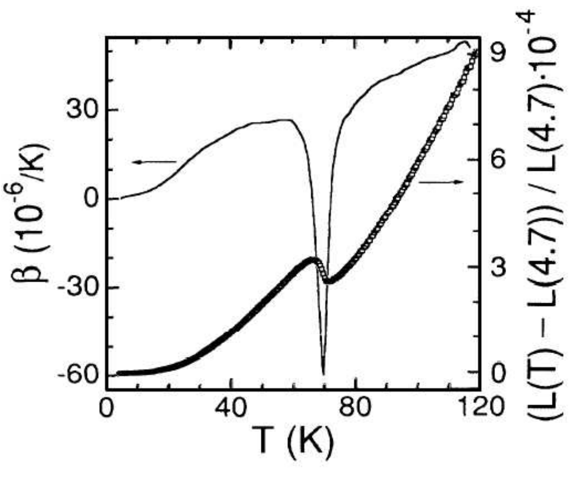

Figure 5.3: *The linear thermal expansion and the volume thermal expansion coefficient of BaVS*$_3$ *from Ref. [11].*

Our argumentation, that the metal-insulator transition is of second order, has recently got a direct verification. Inami et al. [23] found a structural character of the transition by X-ray scattering which has been believed to be absent for a long time. They observed a superlattice reflection appearing at T_{MI} and gradually developing below it, as it is typical of second order structural transitions (see Fig.

5.4). Furthermore, they found that a symmetry breaking of the lattice occurs.

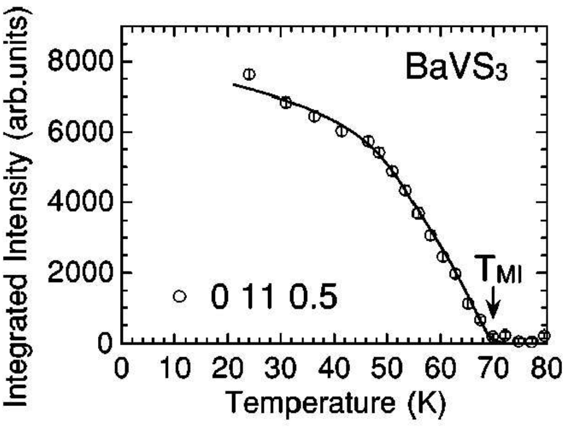

Figure 5.4: *The temperature dependence of the superlattice reflection appearing below T_{MI} from Ref. [23].*

In contrast to the high-temperature phase where all vanadiums are equivalent,[4] in the low symmetry insulating state there are two different crystallographic sites (V_A and V_B) and the vanadiums form an alternating chain along the c-axis: $V_A - V_A - V_B - V_B - V_A - V_A - V_B - V_B$.

The anomalies in the thermodynamical and transport quantities make it obvious that the transition cannot be purely crystallographic but the electron system is also involved. We will examine one by one the simplest type of electronic orderings consistent with the X-ray results.

The onset of spin-Peierls (SP) order is supported by the low-field shape of the $H - T$ phase boundary and consistent with all of the measurements. This kind of order appears in systems with quasi-1D crystal structure resulting in strong exchange coupling between neighbours along the chain, while the exchange energy (J) is negligible between sites at neighbouring chains. The transition can primarily be driven either by the lattice or by the electron system. In the first case the original Hamiltonian is usually the 1D antiferromagnetic (AF) Heisenberg model with uniform first neighbour exchange coupling, J_1. Since the exchange depends on the distance between the atoms, the structural pairing causes a modulation of

---

[4] This is in contrast with early X-ray studies where the orthorhombic distortion was attributed to inequivalent vanadium atoms forming a zigzag chain along the c direction, where the orthorhombic distortion occurs at $T_s = 250\,\mathrm{K}$.

J_1. This leads to singlet formation on the pairs. The illustration of this process is shown in Fig. 5.5.

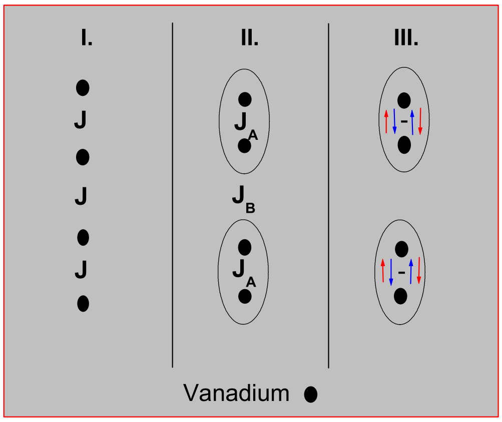

Figure 5.5: *The "steps" of the spin-Peierls transition: I. equidistant vanadium chain with uniform J, II. distorted vanadium chain with modulated J, III. distorted lattice and singlet pairs.*

The above approach would require $J_1 \approx 430\,\mathrm{K}$ for a transition which occurs at $T = 70\,\mathrm{K}$. In contrast, the susceptibility of $BaVS_3$ above T_{MI} is Curie type, i.e. the spin-spin interactions are negligible in the metallic phase. Since the exchange interaction is almost negligible in the metallic phase ($\Theta = 10\,\mathrm{K}$), we rule out that the above model is applicable for $BaVS_3$.

It was pointed out (see the references in [24]) that a relatively strong next neighbour coupling, $J_2 > 0.24J_1$ is solely enough for singlet pair formation on neighbouring sites, which is followed by the distortion of the lattice. However, this requires the next neighbour overlap to be comparable with the nearest neighbour one, which is not realistic for $BaVS_3$. Although, this model is basically different from the previous one, it results in the same ground state. In fact $CuGeO_3$, which is a good realization of the $J_1 - J_2$ model, has a rather similar phase diagram to that of other spin-Peierls systems described in the framework of the 1D AF Heisenberg model (see Fig. 5.17).

There is another way to modulate the exchange interaction. $BaVS_3$ has a twofold orbital degeneracy in the metallic phase. Since the crystal has 3 fold symmetry around the chain axis, we can choose from 6 different orbitals. Generally, systems with orbital degeneracy cannot be treated by a pure spin Hamiltonian, but orbital operators have also to be involved. However, in a mean-field approach for the orbitals one can derive an effective spin Hamiltonian, where the coefficients of the spin operators depends on the expectation value of the orbital operators. [5] Expressed by the parameters of the Hubbard model, the kinetic exchange energy has the form of $J_{kin} \propto \frac{t^2}{U}$, which depends on the overlap of the orbitals. In case of an orbital order it is not likely that the first neighbour overlaps are uniform along the chain, i.e. there is an alternation of the exchange coupling. Fig. 5.6 illustrates schematically the mechanism of this orbitally motivated spin-Peierls transition. The orbital order fundamentally changes the effective spin-spin interactions. In the metal there are localized but independent spin moments, while the low-temperature phase is a singlet insulator. Since $\Delta_s \approx 250\,\mathrm{K}$, one can estimate the exchange coupling between the singlet forming sites to be $J \sim \Delta_s/2 = 125\,\mathrm{K}$.

Note that in BaVS$_3$ indirect overlap through the p orbitals of the sulfurs dominates as indicated in Fig. 5.6. As far as the order parameter is concerned, the X-ray measurement cannot differentiate between the different form factor of A and B orbitals, but detects the accompanying distortion of the sulfur octahedra. Therefore, this kind of orbital order becomes indirectly observable in structural studies.

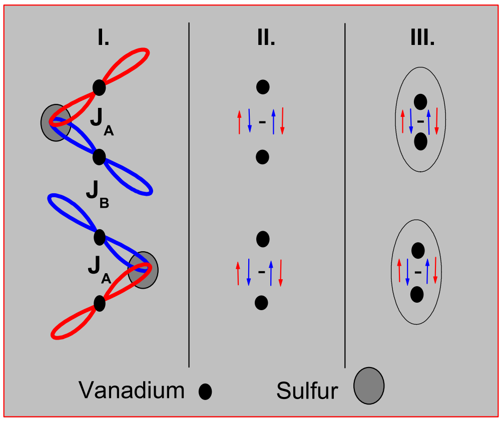

Figure 5.6: *The "steps" of the orbitally driven spin-Peierls transition: I. on an equidistant vanadium chain the orbital order leads to an alternating exchange coupling, II. formation of spin singlets on neighbouring sites, III. due to the singlet pairing the lattice becomes distorted.*

---

[5] For a detailed review of the topic see [24].

We summarize the analogies between the properties of $BaVS_3$ and the SP systems:

1. The transition is of second order and from thermodynamical aspect it is characterized by finite jumps in the specific heat and the derivative of the susceptibility.
2. The transition becomes of first order in magnetic field beyond a critical point. (This will be pointed out for $BaVS_3$ in 5.2.)
3. The low-field dimensionless $H-T$ phase boundary (when H and T is measured in units of the zero field transition temperature) is quadratic with a universal coefficient, $\gamma \approx 0.45$.
4. The gap in the spin excitation spectra, which is the order parameter of the transition, is much smaller than the charge gap. (This will be shown for $BaVS_3$ in 5.2.)
5. The transition temperature decreases rapidly with increasing pressure. The well-known example is $(TMTTF)_2PF_6$, where T_{SP} is reduced in an average rate of $\sim 2\,$K/kbar.
6. The electron system is strongly coupled to the lattice as it is clearly manifested in the structural character of the metal-insulator transition.

If the low-lying phase of $BaVS_3$ is really a SP insulator, it has certainly the highest transition temperature among the known compounds.

Two objections can be raised against the spin-Peierls scenario. The first is that neutron scattering measurements suggest the onset of $2D$ AF order below $T_x = 30\,$K with homogenous (FM) ordering along the chains. It is questionable how the SP phase can be switched to this type of ground state. However, a change in the character of the orbital order, possibly occuring at $T_x = 30\,$K may turn the antiferromagnetic exchange coupling to ferromagnetic. The second is that spin-Peierls transition usually happens between two insulating phase, while $BaVS_3$ is metallic at high temperatures. (The basic criterion is the presence of localized moments.) However, the Curie susceptibility rather indicates the presence of localized electrons and the analysis of transport properties (will be given in 5.3) also proves that the electron system is at the edge of a localized state.

Another possibility that the driving force of the transition is charge ordering and thus the two non-equivalent lattice sites are simply $V_A = V^{4+\delta}$ and $V_B = V^{4-\delta}$. If it is the case, it should be certainly partial ($\delta < 1$), because V^{5+} is nonmagnetic and therefore charge order results in a modulation of the spin density, which has not been observed by neutron scattering. This could not account for the radical freezing out of the susceptibility. Furthermore, the onset of a spin gap remains unexplained, too.

A purely orbital order is also unlikely for the same reasons. The spin degrees of freedom must be basically involved to the transition.

Summarizing, we took into account the simplest electronic orderings consistent with the structural distortion at $T_{MI} = 70\,\mathrm{K}$. We propose a picture of an orbitally driven spin-Peierls transition.[6]

5.2 Extended phase diagram

We have applied several kinds of experimental techniques in order to explore the $p - H - T$ phase diagram of the material. We have rigorously proved that the transition is of second order at ambient pressure. We believe that the phase boundary obtained from our high-pressure transport and optical measurements is the extension of the ambient pressure phenomenon, i.e. a continuous line of second order transitions as a function of pressure. The same should be valid for magnetic fields, too. The following arguments support the above assumption:

1. The peak in logarithmic derivative of the resistivity, the sign change of the thermoelectric power and the gap opening observed in the optical spectra coincide with the anomaly of thermodynamic quantities (jump in the specific heat and the susceptibility derivative) at ambient pressure and in zero field.

---

[6] We demonstrated that the electron transport is nearly isotropic and the same is valid for the susceptibility. However, these findings do not exclude the relevance of a 1D AF effective spin model. The latter only means that the coupling is almost isotropic in spin space as it is the case for SP systems. According to our knowledge no measurement has been reported about the spatial anisotropy of the exchange coupling in $BaVS_3$.

2. Under hydrostatic pressure or in magnetic field, the transition shows up in the same way in the resistivity, the thermoelectric power and the optical spectra than at ambient pressure and in zero field.

3. The ratio of the spin gap and the transition temperature is independent of pressure. (In this section we will show that the same is valid for the charge gap.)

The $p-T$ phase boundary based on our resistivity and thermoelectric power measurements is presented in Fig. 5.7. It is almost linear up to 15 kbar, above which it drops more steeply. The highest pressure, where the metal-insulator transition was established is $p = 19.1$ kbar. Above $p = 20.3$ kbar the system was found to be metallic in the whole temperature range investigated. We have just emphasized that a continuous line of second order transitions of the same kind is observed under pressure. We will come back to that point later whether this picture can be held unlimitedly.

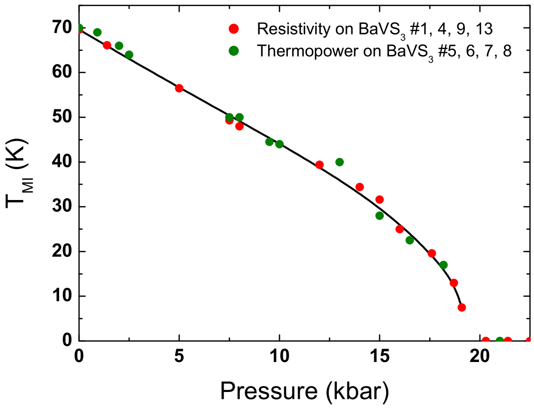

Figure 5.7: *The $p-T$ phase boundary on the basis of transport measurements.*

What happens to the character of the insulating phase while it is more and more suppressed? We could already realize the charge gap and the spin gap are very different. The ratio of the gap and the transition temperature is unusually large for the former, $\Delta_{ch}/k_BT_{MI} \approx 10$, while it is around the BCS value with $\Delta_s/k_BT_{MI} \approx 3.6$ in case of the latter. In 5.1 we have already discussed the evolution of the spin gap with pressure which scales with the transition temperature at least up to 15 kbar. Now, we will focus on the charge excitations and analyze the pressure dependence of the charge gap what we have investigated by transport and optical conductivity measurements. The results are shown in Fig. 5.8. Similarly to the spin gap, the charge gap vanishes proportionally to T_{MI}, roughly according to $\Delta_{ch}(p) \approx 10 \cdot k_B T_{MI}$. It is a central result because it justifies that the nature of the transition is invariant in the region where these scaling relations hold.

We note that the values of the charge gap determined by transport experiments and optical spectroscopy agree within 20% in BaVS$_3$.

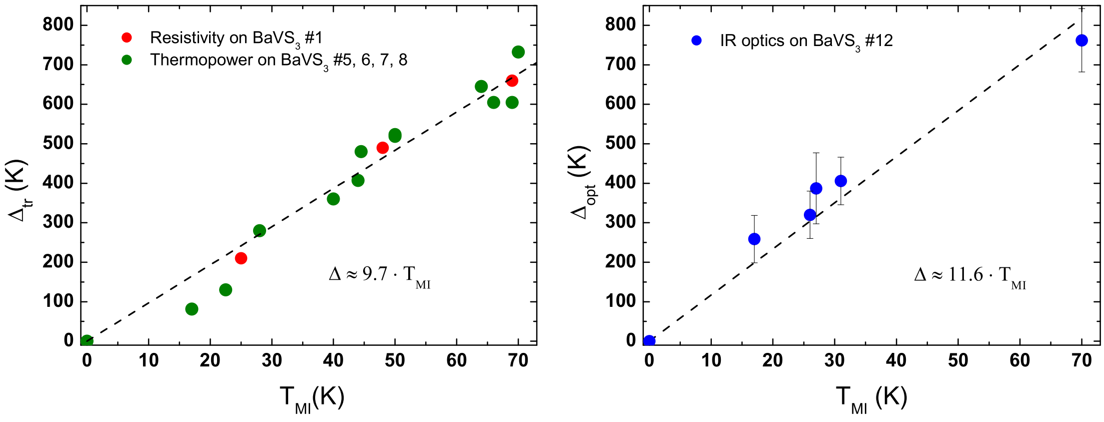

Figure 5.8: *The charge gap of the insulating phase vs. transition temperature. Left side: the gap resulting from transport experiments. Right side: the gap derived from the IR optical spectra.*

In a semiconductor the static dielectric constant is described by the following expression:

$$\varepsilon(\omega = 0) = \varepsilon_\infty + \left(\frac{\omega_p}{\Delta_{opt}}\right)^2 \quad , \tag{5.7}$$

where ε_∞ is the dielectric constant in the high-frequency limit and ω_p is the plasma frequency. A consistency check can be performed by inserting the measured value of the parameters into Eq. 5.7. The real part of the dielectric function in the insulator phase at ambient pressure is presented in Fig. 5.9. The static dielectric constant is $\varepsilon(\omega = 0) \approx 100$ and $\varepsilon_\infty \approx 1$. The plasma frequency in the metallic phase is $\omega_p \approx 5800 cm^{-1} = 8300\,\mathrm{K}$ (as it will be determined in 5.3). With these

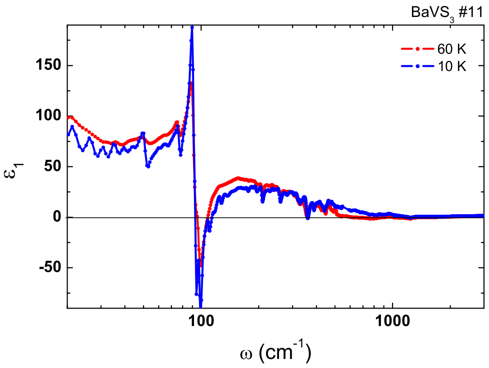

Figure 5.9: *The real part of the dielectric function of $BaVS_3$ at $T = 60\,K$ and $10\,K$.*

numbers one obtain for the charge gap $\Delta_{opt} = 830\,\mathrm{K}$, which agrees within 10% error with the value determined from the conductivity curve.

The optical measurements have pointed out that going through the phase transition the charge gap opens very sharply. At ambient pressure it reaches its zero temperature value already at $T = 64\,\mathrm{K}$ as shown in Fig. 4.16. The gap opens rapidly also at higher pressures.

Next we discuss the high-pressure part of the phase diagram. The measurements under 19.1 kbar and 20.3 kbar are the closest ones surrounding the region where the insulator phase vanishes. In order to fine scan the intermediate range, we applied magnetic field. The critical field, which could completely suppress the transition, is $B_c = 170\,\mathrm{T}$ at ambient pressure. Furthermore, we showed that B_c decreases proportionally to T_{MI} with increasing pressure. Thus, at $p = 19.1\,\mathrm{kbar}$ where the transition is pushed down to $T_{MI} = 7.5\,\mathrm{K}$, we would expect a critical field $B_c \approx 18\,\mathrm{T}$, if the shape of the $H - T$ phase boundary does not vary dramatically. However, it does. The smooth decrease of the transition temperature with magnetic field is broken around $B = 5.8\,\mathrm{T}$ and it suddenly drops down to zero which suggests that the character of the transition changes at this point as shown in Fig. 5.10.

This is a further similarity to spin-Peierls systems, where it was found that the dimer phase boundary in low fields is of second order, but above a critical point, (H^*, T^*) it becomes of first order and the transition temperature sharply drops to zero. Fig. 5.17, presented at the end of this Chapter, summarizes the

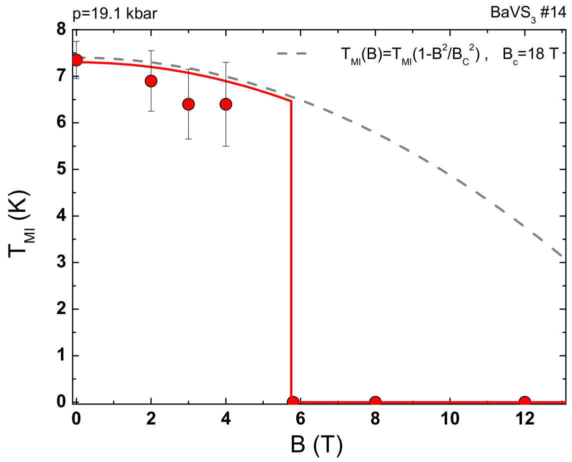

Figure 5.10: *The* $H-T$ *phase boundary in the vicinity of* $p_{cr} \approx 20$ *kbar. The gray line shows the behaviour expected from the low-field extrapolations. The red line shows how the transition occurs presumably.*

theoretical predictions and also shows experimental results obtained for several SP compounds.

Concerning Cross's theoretical predictions, which fairly agrees with the experimental results on several SP compounds, the location of the critical point can be related to the zero field transition temperature, $T_{SP}(0)$ according to the following relations: $T^* = 0.77T_{SP}(0)$ and $\mu_B H^* = 0.69k_B T_{SP}(0)$. [7] In BaVS$_3$ at $p = 19.1\,\mathrm{kbar}$ the transition occurs at $T_{MI} = 7.5 \pm 0.4\,\mathrm{K}$ without magnetic field, thus the corresponding location of the critical point should be at $H^* = 7.2 \pm 0.4 \cdot 10^4 G$ and $T^* = 5.8 \pm 0.3\,\mathrm{K}$, which is very close to our observation.

Furthermore, in high-field magnetization measurement performed at ambient pressure, Shiga et al. [27] observed a metamagnetic transition (a positive jump in the magnetization) around 50 T, which is only 25% lower than what would be expected from Cross's theory. They measured the magnetization between 4.2 K and 40 K at different temperatures and found that the field, where the transition takes place, is independent of temperature. They emphasized that the transition is accompanied by a ~ 10 T wide hysteresis, i.e. it is of first order. All these

---

[7] It also gives a good description of $CuGe_3$, although the mechanism of the spin-Peierls transition is rather different in this compound.

results support a spin-Peierls-like transition.

This scenario explains the collapse of the second order phase boundary in presence of magnetic fields but still allows that the transition can be suppressed to any infinitesimal temperature by the applied pressure. The complete $p-T$ phase diagram looks like as it is presented in Fig. 5.11.

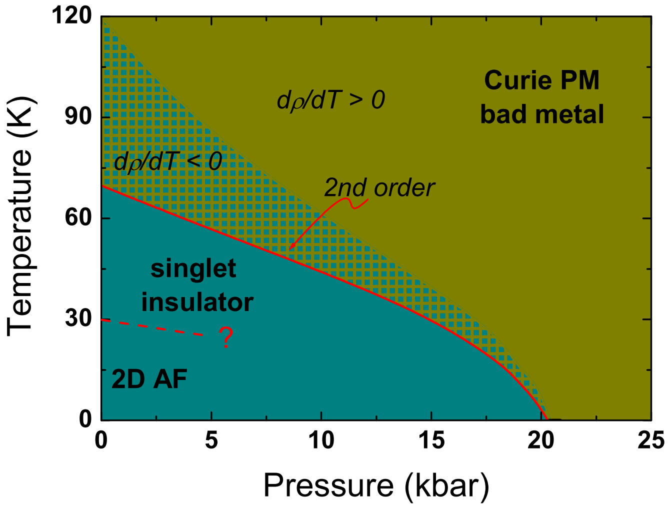

Figure 5.11: *The $p-T$ phase diagram of BaVS$_3$. It can be divided into four regions: the normal part of the metallic phase ($\partial\rho/\partial T > 0$), the precursor region, the singlet insulator and the underlying 2D antiferromagnet. The phase boundary between the last two states is not known.*

Since we also have explored the effect of magnetic field on the transition, we can construct the whole $p-H-T$ phase diagram of the system. It has to be note that we rely on the low-field behaviour and the higher field regions are obtained by extrapolation. In the pressure range of $p = 0-15\,\mathrm{kbar}$ the ratio of the highest applied field and the critical field moves between 7% and 17%. However, in spin-Peierls systems the low-field quadratic behaviour gives a good approximation of the phase boundary up to the critical point as it is shown in Fig. 5.17 in case of CuGeO$_3$. [8] The critical line in Fig. 5.12, along which the transition becomes of first order, corresponds to the criterion of Cross, $\mu_B H^* = 0.69 k_B T_{SP}(0,p)$, where

---

[8] This also verify the validity of the relation what we used to derive the spin gap, $\Delta_s = 2gS\mu_B H$. In their notation the phase boundary has the form $\frac{\Delta T_{MI}(H)}{T_{MI}} = -\gamma\left(\frac{g\mu_B H}{\Delta_s}\right)^2$ with $\gamma = 0.384$. Taking into account that $\Delta_s/k_B T_{MI} \approx 3.52$, this is equivalent to Eq.5.3.

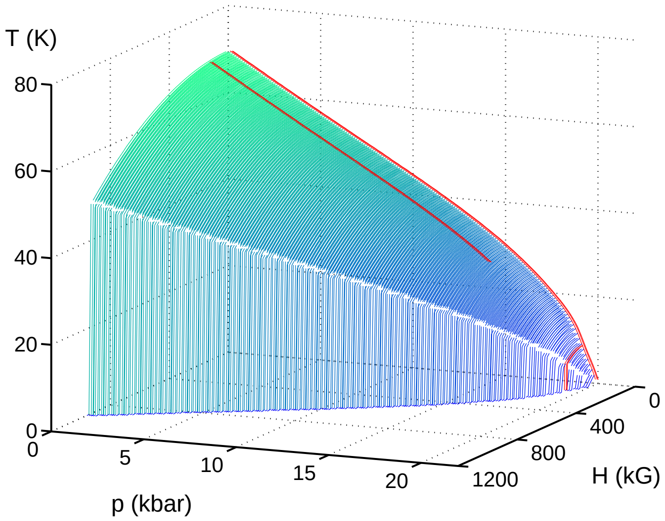

Figure 5.12: *The $H-p-T$ phase boundary of the singlet insulator state in $BaVS_3$. The red lines show the region of the measurements.*

$T_{SP}(0.p)$ is the zero field transition temperature as a function of pressure.

5.3 "Bad metal" phase

The contradiction between the metallic transport and the Curie-like susceptibility (characteristic of localized moments) in the high-temperature phase of BaVS$_3$ has not been solved so far. If someone was impressed by the shape of the susceptibility and the resistivity upturn (below $T_{min} = 140\,\mathrm{K}\ \partial\rho/\partial T < 0$), and thus was sceptic whether the high-temperature phase would be a real metal at all, the results of the optical conductivity measurements should convince him.

Above T_{MI} the reflectivity tends $R \rightarrow 1$ approaching zero frequency as expected for metals. The low-frequency range was fitted by the Hagen-Rubens law ($R \approx 1 - 2\sqrt{\frac{4\pi\omega(cm^{-1})}{Z_0\sigma_0}}$) both at room temperature and $T = 70\,\mathrm{K}$. The results were consistent with the dc conductivity obtained from transport experiments.[9] We can try whether the entire shape of the reflectivity can be interpreted in the simple Drude model. Fig. 5.13 shows the Drude fits for both temperatures.

---

[9] The optical measurements have been performed with arbitrary polarization in the $a-c$ plane, therefore the optical conductivity is a mixture of the conductivity along and perpendicular to the chain direction.

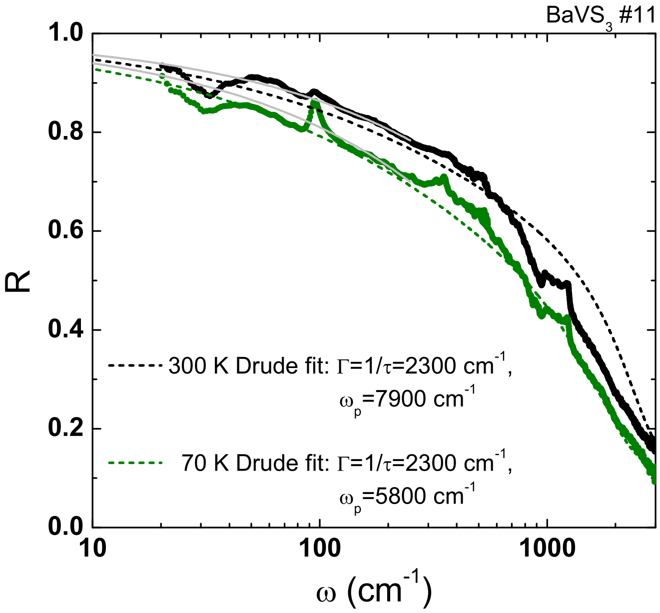

Figure 5.13: *The frequency dependence of the reflectivity in the metallic phase of BaVS*$_3$ *at* $T = 70$ *and* $300\,K$. *The dashed lines indicate the result of the Drude fits. The gray lines are the low-frequency Hagen-Rubens fits.*

The relaxation time, found to be $\tau \approx 2.3 \cdot 10^{-15}\,\mathrm{s}$ at both temperature, is one order of magnitude shorter than in normal metals like Cu, Ag, etc. The plasma frequency is different in the two cases, $\omega_p \approx 1.5 \cdot 10^{15}\,\mathrm{s}^{-1}$ and $1.1 \cdot 10^{15}\,\mathrm{s}^{-1}$ at $T = 300\,\mathrm{K}$ and $70\,\mathrm{K}$, respectively. The resulting dc conductivity values ($\sigma_0 = \omega_p^2\tau/4\pi$) are about 70% of those determined by the Hagen-Rubens law since the Drude fits underestimate the low-frequency reflectivity. Assuming that the charge carrier density is one electron per site ($n = 4.5 \cdot 10^{21}\,\mathrm{cm}^{-3}$), one can also derive the effective mass in the Drude model ($\omega_p^2 = 4\pi n e^2/m^*$) and finds $m^* \approx 7 m_{e-}$ at room temperature.[10] Although the Drude model gives only a rough description of the metallic phase of BaVS$_3$, the obtained small relaxation time and large effective mass indicate that correlations are important not only in the insulating phase but also in the metallic state.

---

[10] The carrier density could be determined from the conductivity sum rule, but in our case the investigated frequency range is too narrow for this purpose, since the reflectivity is still as high as $R \approx 0.2$ at the highest frequency of the measurement.

The overall shape of the temperature dependence of the Seebeck coefficient[11] suggests the presence of propagating electrons. In a quasi-free electron model one would expect the Seebeck coefficient linearly increasing with temperature:

$$\Pi = -\frac{\pi^2}{3}\frac{k_B}{e}\frac{T}{T_F} \quad , \tag{5.8}$$

where the Fermi temperature is related to the effective mass and the density of the carriers, $k_BT_F = \epsilon_F = \frac{\hbar^2}{2m^*}(3\pi^2 n)^{2/3}$. For a quasi-free electron gas the one-electron entropy has a quite similar form, $S = \frac{\pi^2}{2}k_B\frac{T}{T_F}$.
In contrast with the above limit, in case of strong electron-electron interactions (at temperatures $U \gg k_BT \gg t$), Chaikin and Beni [28] derived that the thermoelectric power is constant, since it measures the configurational entropy per carrier (the single carrier entropy corresponding to the actual band filling) which is saturated.

$BaVS_3$ does not give a good realization either of the quasi-free electron picture or a completely localized system. Fig. 5.14 gives a comparison of the entropy (measured by H. Imai et al. [20]), the magnetic susceptibility (from Ref. [21]) and the transport properties in the metallic phase of $BaVS_3$.

Though the entropy increases above T_{MI} its temperature dependence is not linear. It is far from $S = Rln4$ even at $T = 300\,\mathrm{K}$ (which would correspond to total liberation of the spin and orbital degrees of freedom), suggesting that in a metallic picture the temperature is well below the bandwidth.

The magnetic susceptibility implies the localized character of the carriers. The Curie constant is $C = 0.25\,\mathrm{emu/mole}$ at room temperature. The spin only value of the susceptibility[12] with one electron per site would be $C_s = 0.37\,\mathrm{emu/mole}$, which means that localized moments are present at about 70% of the vanadium sites. (If we assume that each vanadium carries uniform magnetic moment, we obtain $p_{eff} \approx 1.4$ effective Bohr magneton number, instead of $p_{eff} \approx 1.73$ corresponding to the spin only value.)

If we enforce a metallic interpretation of the Seebeck coefficient, since it is

---

[11] From now on the thermoelectric power is marked by Π and S is reserved for the entropy.

[12] Although it is a good approximation in many $3d$-systems, since the orbital moment is quenched by the crystal field, it is undoubtedly a rough estimation in $BaVS_3$, where the low-lying $e(t_{2g})$ doublet carries orbital momentum.

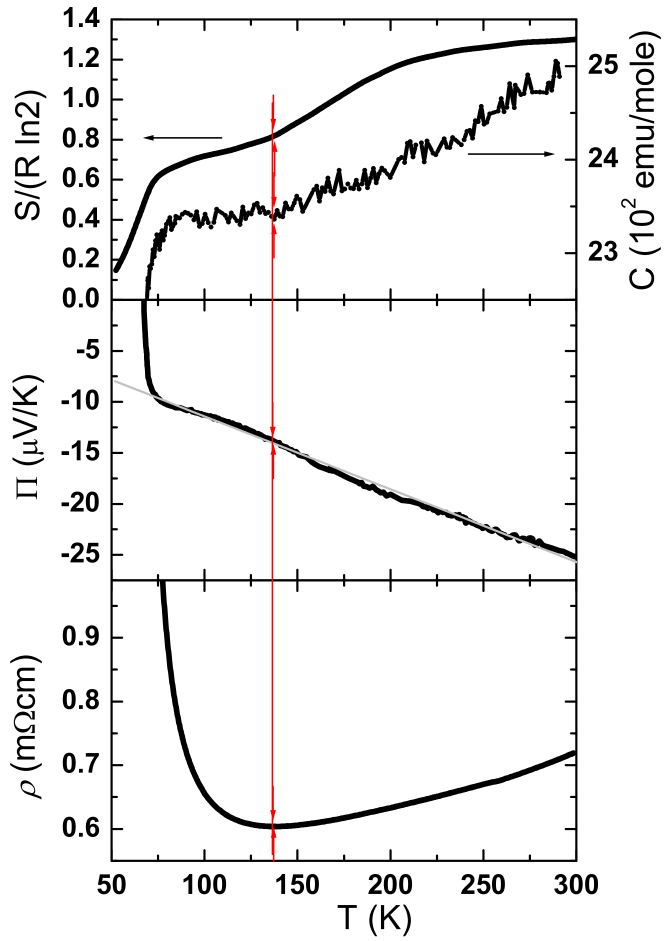

Figure 5.14: *Temperature dependence of the entropy, the Curie constant, the thermoelectric power and the resistivity in the metallic phase of $BaVS_3$. The first two are based on the data from Ref. [20] and [21].*

roughly linear up to $T = 700\,\mathrm{K}$ (as shown in Fig. 4.7), we obtain $T_F \approx 4000\,\mathrm{K}$. The linear fit shown in Fig. 5.14 fairly approximates the data at higher temperature, too. This value is one order of magnitude smaller than in good metals, like alkali metals. The effective mass derived in this model is $m_{eff} = 3m_{e^-}$. This is 2 times smaller than what we obtained from the Drude fit.

Finally, we turn to the analysis of the resistivity. Above 140 K $\partial\rho/\partial T > 0$ and the resistivity is almost linear in a wide range of temperature as it can be checked in Fig. 4.2. However, a simple high-temperature electron-phonon scattering fails to explain this behaviour since the corresponding residual resistivity would be extremely high, $\rho_0 \approx 0.45\,\mathrm{m\Omega cm}$, which can be excluded by the high-pressure measurements. On the other hand, the absolute value of the resistivity is very large; it is about 35 times larger than that of the vanadium metal at $T = 300\,\mathrm{K}$ and it is close to the Ioffe-Regel limit at $T = 700\,\mathrm{K}$, i.e. the mean free path is reduced to the range of the lattice constant. (The Ioffe-Regel criterion, $\rho = \frac{\hbar a}{e^2}$ gives $1.5\,\mathrm{m\Omega cm}$ minimal metallic resistivity with an average lattice constant of $a = 5\,\mathrm{\AA}$. This has to be compared to the resistivity at 700 K, which is $\rho = 1.15\,\mathrm{m\Omega cm}$.)

Below 140 K there is an anomalous metallic region, where $\partial\rho/\partial T < 0$. Fig. 5.14 points out that this anomaly is reflected in all of the measured quantities. The enhancement inside of the metallic phase, which is present both in the entropy and the Curie constant, suggests the appearance of additional degrees of freedom. One possible explanation is that, the effective band occupancy changes in this temperature range. (The increase of the entropy shows up also in the thermoelectric power, since it depends on the band occupancy for strong correlations.) This is supported also by our observation that the plasma frequency is smaller at $T = 70\,\mathrm{K}$ than at room temperature, which corresponds to a factor of 2 decrease in the carrier concentration.

Summarizing our results about the metallic phase of $\mathrm{BAVS_3}$, we can conclude that the system is situated at the edge of the metallic state with strong tendency towards localization. The susceptibility perceives localized carriers while transport and the optical properties imply that the electrons have anomalously short lifetime (or mean free path) and large effective mass. We have already mentioned in 2.6 that the on-site Coulomb repulsion for d orbitals is $U \approx 1\,\mathrm{eV}$. With the approximated bandwidth,[13] $W_{eff} \approx 4000K = 0.34\,\mathrm{eV}$ the relative strength of the correlation, U/W_{eff} is around unity in $\mathrm{BaVS_3}$.

5.4 Quantum critical phenomena

Phase transition usually occurs when the thermal fluctuations are strong enough to destroy the order of the low-temperature state. However, phase transitions can also be induced at zero temperature by tuning some parameter (let us call it s)

---

[13] Which is half of the value predicted by band structure calculations [4].

of the Hamiltonian by the application of pressure, magnetic field or by changing the composition of the compound. In these kinds of transitions the disappearance of the collective order is caused by quantum fluctuations and therefore they are called quantum phase transitions. The observation of this phenomenon is not restricted to absolute zero temperature. As far as the characteristic energy of the quantum fluctuations is larger than the temperature they have noticeable influence on macroscopic properties. Similarly to second order phase transitions, the thermodynamical properties satisfy scaling relations. Close to the critical value of the control parameter (s_{cr}), where the quantum phase transition occurs, these quantities show power-law dependence on the temperature, while at zero temperature they depend in the same way on the reduced control parameter, $(s - s_{cr})/s_{cr}$. This part of the phase diagram is called quantum critical region. Not only thermodynamic properties but the conductivity is also predicted to follow a scaling relationship by Ref. [29]:

$$\sigma(T, s) = \xi(s)^{-\mu/\nu} f(T\tau(s)) \quad , \tag{5.9}$$

where $\xi(s)$ is the correlation length and $\tau(s)$ is the relaxation time, both diverging at the quantum phase transition according to $\xi(s) \propto (s - s_{cr})^{-\nu}$ and $\tau(s) \propto (s - s_{cr})^{-z\nu}$. The dynamical exponent, z, which controls the critical slowing down may vary but $\mu = 1$ has been found to be universal for many systems. At zero temperature Eq. 5.9 becomes simpler:

$$\sigma(s) \propto (s - s_{cr})^{\mu} \quad . \tag{5.10}$$

In some cases this scaling with the control parameter was directly observed at very low temperatures (typically below 100 mK) [30, 31]. Usually the power-law behaviour of the conductivity with a non-conventional exponent is the only indicator for the presence of quantum critical fluctuations in a region where the transition was sufficiently suppressed. In a Fermi-liquid the electron-electron interaction results in a quadratic temperature dependence of the resistivity:

$$\rho(T) = \rho_0 + AT^2 \quad , \tag{5.11}$$

where ρ_0 is the residual resistivity due to impurity scattering and A is the electron-electron scattering amplitude which is constant at low temperatures. This expression can remain valid in case of strong correlations, though A is enhanced similarly to the effective mass. In the vicinity of a quantum critical point the scattering is stronger due to the quantum fluctuations and therefore $\rho(T)-\rho_0 = \Delta\rho \propto T^n$ with an exponent $1 \leqslant n < 2$ over $1-2$ decades of the temperature as found in several f-electron systems like $CePd_2Si_2$ [32], $CeCu_2Si_2$ [33], $CeNi_2Ge_2$ [33], $YbRh_2Si_2$ [34], and the d-electron system $CaRuO_3$ [35].

In the above nearly antiferromagnetic systems the closeness of the antiferromagnetic quantum critical point is thought to be responsible for the anomalous scattering. In most cases either the susceptibility or the specific heat were also measured and found to follow a power-law behaviour predicted theoretically. There are also several examples for nearly ferromagnetic systems ($LiHoF_4$ [31], MnSi [36]) which can be driven through a ferromagnetic quantum critical point. As far as we know, quantum phase transition has not been observed yet from a singlet insulator state to a paramagnetic metal.

We have demonstrated that the singlet insulator phase of $BaVS_3$ can be suppressed by hydrostatic pressure and we have explored the $p-T$ phase boundary. The highest pressure where the onset of the metal to insulator transition was observed is $p = 19.1\,\mathrm{kbar}$ with the corresponding transition temperature, $T_{MI} = 7.5\,\mathrm{K}$. Under $p = 20.3\,\mathrm{kbar}$ the transition, if exists at finite temperature, takes place below 2 K. On the other hand, the measurement at $p = 22.5\,\mathrm{kbar}$ was certainly above the critical pressure. We do not have an insight into the pressure dependence of the low-temperature resistivity in the vicinity of the critical point, but we can analyze the temperature dependent resistivity at the two nearest pressures. In 4.4.2, the double logarithmic plot of the temperature dependence of the resistivity showed that at the highest pressure the resistivity follows power-law behaviour from 1 K to 40 K with an exponent $n \approx 1.25$, while at $p = 20.3\,\mathrm{kbar}$ the exponent shows a slight magnetic field dependence. A more accurate analysis can be carried out if we directly determine the temperature dependence of the exponent in the different cases. Fig. 5.15 shows the exponent as a function of temperature for the higher pressure and for the lower pressure both in zero field and 12 T.

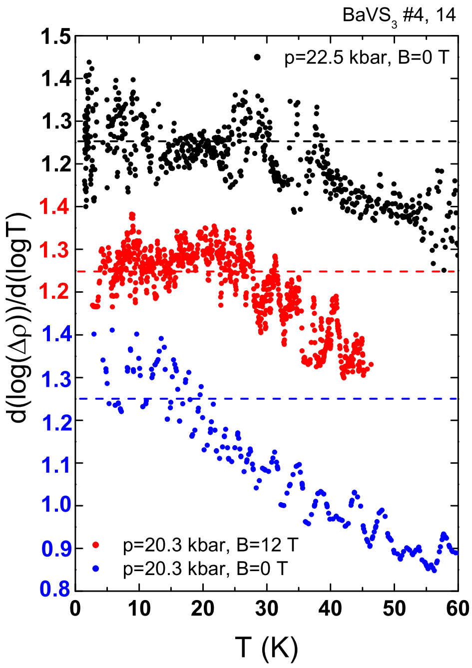

Figure 5.15: *The exponent of the power-law behaviour characteristic of the low-temperature resistivity vs. temperature. The dashed line corresponds to* $n = 1.25$ *in each case.*

The resistivity at $p = 22.5\,\mathrm{kbar}$ clearly follows $\Delta\rho \propto T^{1.25}$ up to 40 K. In case of the lower pressure, it turns out that the right description is not a slightly changing exponent for different magnetic fields. Instead the exponent of the power-law remains constant and the validity of this behaviour is restricted to different range of temperature depending on the magnetic field. With increasing field the region gradually extends and in $B = 12\,\mathrm{T}$ it is almost as wide as in case of $p = 22.5\,\mathrm{kbar}$. The field dependence of the low-temperature magnetoresistance under $p = 20.3\,\mathrm{kbar}$, shown in Fig. 4.25, is composed of two terms. The low-field negative contribution indicates that the metal to insulator transition is not completely suppressed by the pressure (although it is below the range covered by the experiment) and can be further suppressed by magnetic field. At higher fields a positive term dominates which can be related to the enhanced scattering amplitude approaching the critical point. This is supported by the fact that this contribution only exists on the scale where the power-law behaviour holds.

We can finally conclude that the critical pressure is very close to 22.5 kbar in $BaVS_3$. The transition from the singlet insulator to the paramagnetic metal ground state is accompanied by quantum critical fluctuations in an extended range of temperature in the vicinity of p_{cr}. The magnetic field can also play the role of the control parameter and the combined application of pressure and magnetic field gives the opportunity to fine scan this region.

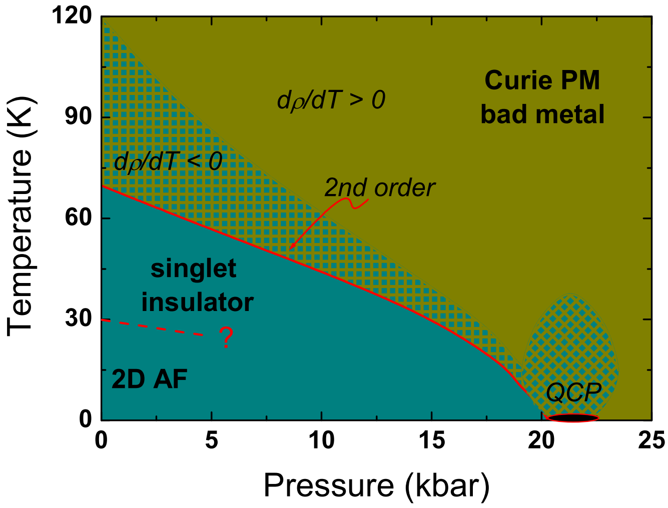

Figure 5.16: *The $p-T$ phase diagram of $BaVS_3$ indicating schematically the quantum critical region between the singlet insulator and the paramagnetic metal.*

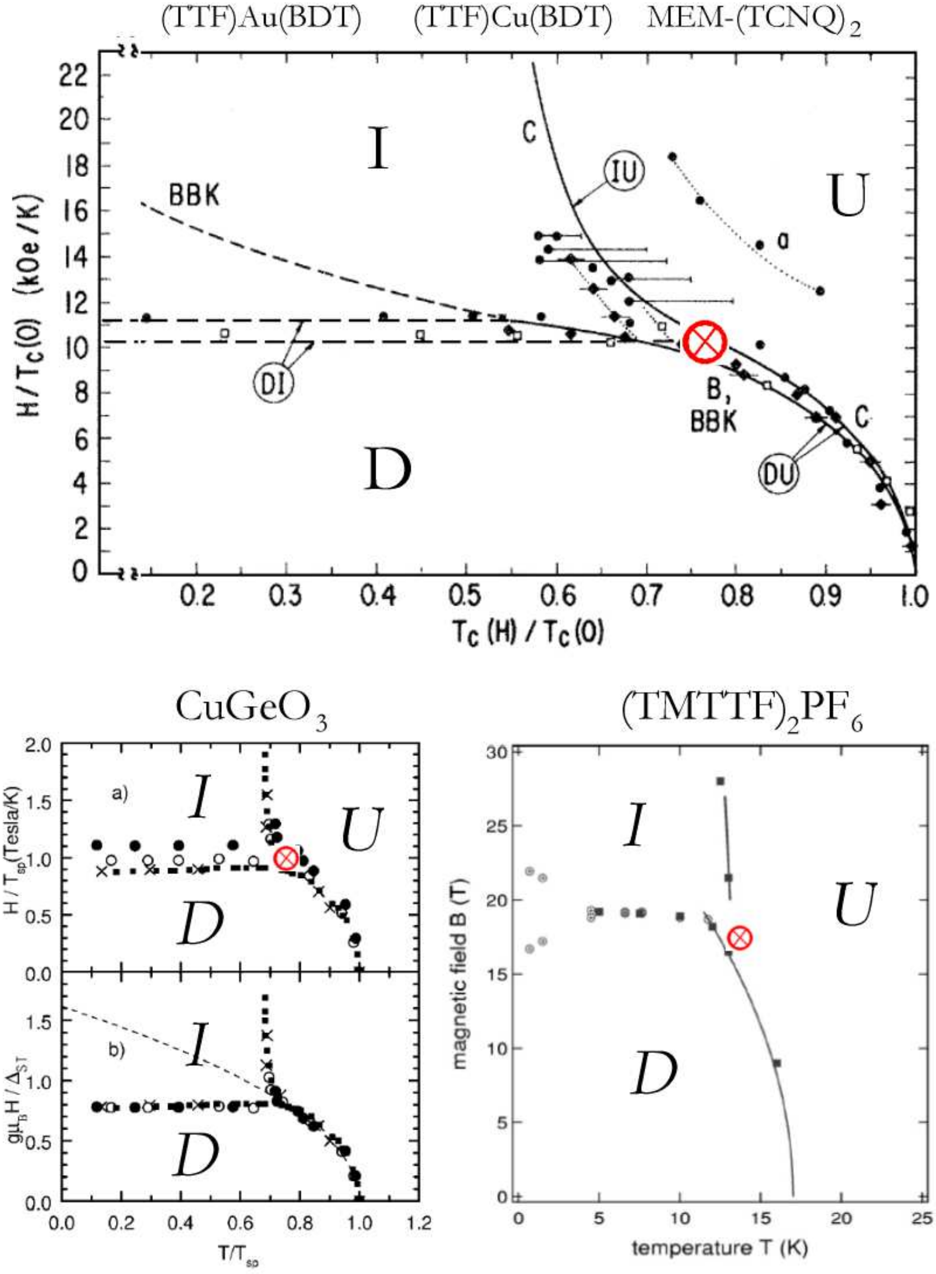

Figure 5.17: *Upper graph: Universal phase diagram of spin-Peierls systems [18]. D, I, U denote the dimer, the intermediate and the uniform phases. The lines labelled with C, B and BBK are the theoretical curves of Cross, Bray and Bulaevskii et al. The experimental data are obtained for TTF-AuS$_4$C$_4$(CF$_3$)$_4$, TTF-CuS$_4$C$_4$(CF$_3$)$_4$ and MEM-(TCNQ)$_2$. Left lower panel: The phase boundary of CuGeO$_3$ [25]. The dashed line shows the extrapolation of the low-field quadratic behaviour. Right lower plot: The phase boundary of (TMTTF)$_2$PF$_6$ compound [26]. Red cross corresponds to the location of the critical point concerning Cross.*

Chapter 6

Conclusion

6.1 Summary

The aim of my Ph.D. research was to explore the "magnetic field – pressure – temperature" ($H - p - T$) phase diagram of a vanadium based correlated d-electron compound, the BaVS$_3$. To determine the phase boundary and characterize the phases I used various experimental techniques, namely dc transport measurements (resistivity, magnetoresistivity, conduction anisotropy, thermoelectric power) and infrared spectroscopy. All of these methods have also been applied under hydrostatic pressure, typically in the range of $p = 0 - 25\,\mathrm{kbar}$. The main results are summarized in the following thesis points:

1. On the basis of the resistivity, thermoelectric power and infrared spectroscopy measurements performed at the ambient pressure in the high-temperature phase of BaVS$_3$, I have demonstrated that the system is situated at the edge of the metallic state with a strong tendency towards localization. Transport and optical properties demonstrate that the electrons have anomalously short lifetime (the mean free path is very close to the lattice constant) and large effective mass ($m^* \approx 7m_{e^-}$) [1, 2]. Conduction anisotropy measurements have shown that the transport mechanism is nearly isotropic [1]. Based on the results of the thermoelectric power experiments I estimated the bandwidth to be $W_{eff} \approx 4000\,\mathrm{K} = 0.34\,\mathrm{eV}$. The on-site Coulomb repulsion for d orbitals is $U \approx 1\,\mathrm{eV}$. Thus the relative strength of

the correlation, U/W_{eff} in $\mathrm{BaVS_3}$ is close to unity.

2. I have shown that the metal to insulator transition, which occurs at $T_{MI} = 70\,\mathrm{K}$, is of second order at ambient pressure [3]. The argumentation is based on the analysis of the low-field $H-T$ phase boundary determined by magnetoresistance measurements and the comparison of the magnetic susceptibility and specific heat anomalies reported in the literature. This statement has recently got direct evidence by the observation of the structural component of the transition in X-ray experiments.

3. I have explored the $p-T$ phase boundary both by transport and infrared conductivity experiments [4, 5]. For the optical studies I have developed a pressure cell which is applicable up to 30 kbar and allows investigations also in the long wavelength, far-infrared region. The metal-insulator transition is suppressed under hydrostatic pressure with a rate of $\sim 3.5\,\mathrm{K/kbar}$. The second order transition line extends up to at least $p = 19\,\mathrm{kbar}$, where the transition temperature is reduced to $T_{MI} = 7.5\,\mathrm{K}$.

4. I have proposed that the metal-insulator transition is an orbitally driven spin-Peierls-like transition. The reduced $H-T$ phase boundary of the singlet insulator (when H and T are measured in the units of the zero field transition temperature) is independent of pressure and agrees well with the universal phase diagram of the spin-Peierls systems [3]. The spin gap, which is the order parameter of the singlet insulator, is derived from magnetoresistance measurements as a function of pressure in the range of $p = 0 - 15\,\mathrm{kbar}$ [3]. Its is $\Delta_s \approx 250\,\mathrm{K}$ at ambient pressure and satisfies a scaling relationship: $\Delta_s(p) \approx 3.6 \cdot k_B T_{MI}(p)$, where the scaling factor is close to the BCS value.

5. I have determined the charge gap of the insulating phase both by dc transport and infrared conductivity measurements at various pressures up to $p = 18\,\mathrm{kbar}$ [5]. It is $\Delta_{ch} \approx 750\,\mathrm{K}$ at ambient pressure and it also scales with the transition temperature according to $\Delta_{ch}(p) \approx 10 \cdot k_B T_{MI}(p)$. The charge excitations are of much higher energy than the spin excitations. Their scale is related to the on-site Coulomb repulsion, since they are accompanied with a double occupation on the vanadium sites. In contrast, the energy needed

to break up of singlet pairs, which does not necessarily result in double occupancy, is determined by the exchange coupling.

6. At high pressures, when the transition temperature is sufficiently reduced, I have observed the magnetic field induced collapse of the second order phase boundary. At $p = 19\,\mathrm{kbar}$, the metal to insulator transition becomes first order at a critical magnetic field of $B_c \approx 6\,\mathrm{T}$. The appearance of a first order phase boundary in the presence of a magnetic field is characteristic of spin-Peierls systems.

7. The insulating phase is completely suppressed at $p = 22.5\,\mathrm{kbar}$ and the metallic state extends to zero temperature. At a certain pressure between $p = 19\,\mathrm{kbar}$ and $22.5\,\mathrm{kbar}$, a quantum phase transition occurs at zero temperature from the singlet insulator to the paramagnetic metal [4, 6]. The quantum fluctuations become strong enough to destroy the singlet phase. In the vicinity of the critical pressure, the fluctuations enhance the electron-electron scattering over an extended range of temperature. This results in a power-law behaviour of the resistivity $\rho \propto T^\alpha$ with an unusual exponent $\alpha < 2$. In our case $\alpha \approx 1.25$ and the power-law holds from $T = 1\,\mathrm{K}$ to $40\,\mathrm{K}$. Such a phenomenon has been known to be present in systems close a ferromagnetic or antiferromagnetic critical point, but not in a singlet insulator.

6.2 Related publications

[1] G. Mihály, I. Kézsmárki, F. Zámborszky, M. Miljak, K. Penc, P. Fazekas, H. Berger, and L. Forró
Orbitally driven spin pairing in the 3d non-magnetic Mott insulator $BaVS_3$*: evidence from single crystal studies*
Phys. Rev. B, Rapid Communications **61**, 7831 (2000)

[2] G.Mihály, I. Kézsmárki, P. Fazekas, C. Homes, L. Mihály, H. Berger, N. Barišić, R. Gaál, L. Forró
Optical and transport properties in the bad metal phase of $BaVS_3$
to be published

[3] I. Kézsmárki, Sz. Csonka, H. Berger, L. Forró, P. Fazekas, and G. Mihály
Pressure dependence of the spin gap in BaVS$_3$
Phys. Rev. B, Rapid Communications **63**, 81106 (2001)

[4] L. Forró, R. Gaál, H. Berger, P. Fazekas, K. Penc, I. Kézsmárki, and G. Mihály
Pressure induced quantum critical point and non-Fermi-liquid behaviour in BaVS$_3$
Phys. Rev. Lett. **85**, 1938 (2000)

[5] I. Kézsmárki, R. Gaál, C. Homes, G. Mihály, H. Berger, N. Barišić, L. Forró, and L. Mihály
Pressure induced suppression of the singlet insulator phase in BaVS$_3$*: infrared optical study*
to be published

[6] P. Fazekas, K. Penc, H. Berger, L. Forró, Sz. Csonka, I. Kézsmárki, and G. Mihály
BaVS$_3$*: from spin gap insulator to non Fermi liquid*
Physica B **312**, 694 (2002)

6.3 Additional publications

[1] Z. V. Popovic, G. Mihály, I. Kézsmárki, H. Berger, L. Forró, and V. V. Moshchalkov
Phonon and spin dynamics in BaVS$_3$ *single crystals*
Phys. Rev. B **65**, 132301 (2002)

[2] N. Barišić, R.Gaál, I. Kézsmárki, G. Mihály, and L. Forró
Pressure dependence of the thermoelectric power of single-walled carbon nanotubes
Phys. Rev. B **65**, 241403 (2002)

[3] J. Balogh, L. F. Kiss, A. Halbritter, I. Kézsmárki, and G. Mihály
Magnetoresistance of Ag/Fe/Ag and Cr/Fe/Cr trilayers

Solid State Commun. **122**, 59 (2002)

[4] J. Balogh, I. Vincze, D. Kaptás, T. Kemény, T. Pusztai, L.F. Kiss, E. Szilágyi, Z. Zolnai, I. Kézsmárki, A. Halbritter, and G. Mihály
Interface magnetoresistance of Fe/Ag multilayers Physica Status Solidi A **183**, 621 (2002)

[5] F. Zámborszky, I. Kézsmárki, L.K. Montgomery, and G. Mihály
Pressure induced crossover in the electronic states of $(TMTTF)_2Br$
Ferroelectrics **249**, 57 (2001)

[6] G. Mihály, I. Kézsmárki, F. Zámborszky, and L. Forró
Hall effect and conduction anisotropy in the organic conductor $(TMTSF)_2PF_6$
Phys. Rev. Lett. **84**, 2670 (2000)

[7] G. Kriza, G. Szeghy, I. Kézsmárki, and G. Mihály
Field scaling and exponential temperature dependence of the magnetoresistance in $(TMTSF)_2PF_6$
Phys. Rev. B, Rapid Communications **60**, 8434 (1999)

[8] G. Mihály, F. Zámborszky, I. Kézsmárki, and L. Forró
Dimensional crossover, electronic confinement and charge localization in organic metals
in Open Problems in Srongly Correlated Systems, Ed. J. Bonca, pp. 263-271
Kluwer Academic Publishers (2001)

[9] J. Balogh, A. Gábor, D. Kaptás, L.F. Kiss, M. Csontos, A. Halbritter, I. Kézsmárki, and G. Mihály
GMR of a single interface: magnetoresistance of Ag/Fe/Ag trilayers
in "Kondo Effect and Dephasing in Low-Dimensional Metallic Systems", Ed. C. Van Haesendonck, Kluwer Academic Publishers (2001)

[10] G. Kriza, G. Szeghy, I. Kézsmárki, and G. Mihály
Power law field dependence of the 2D magnetoresistance in (TMTSF)2PF6
Journal de Physique IV France **9**, Pr10-235 (1999)

[11] I. Kézsmárki, F. Zámborszky, L.K. Montgomery, and G. Mihály
Conduction anisotropy of the Bechgaard salts
Journal de Physique IV France **9**, Pr10-263 (1999)

6.4 Acknowledgment

My first acknowledgement must go to my supervisor, Prof. György Mihály for his coordination during my whole Ph.D. research. He has given the motivation indispensable to perform fundamental research, acquainted me with several experimental methods and guided me in writing the thesis.

I also acknowledge Prof. László Forró for attracting our attention to this material. The continuous collaboration with his group, including frequent invitations to perform mutual experiments in his laboratory, has greatly promoted these studies.

I would also like to thank Prof. László Mihály to acquaint me with infrared spectroscopy and coordinating the optical measurements performed in the Brookhaven National Laboratory.

I would like to express my gratitude to Prof. Patrik Fazekas for teaching me the basics of magnetism and orbital physics and for the useful theoretical discussions during my whole Ph.D. work.

I would like to thank Neven Barišić, Richard Gaál and Szabolcs Csonka for performing fruitful mutual experiments from which I have learned much.

I am grateful to László Demkó for creating the right computational background and the continuous software development.

Chapter 7

Appendix A

7.1 Relative and absolute reflectivity measurement

The reflectivity of a sample relative to a transparent reference material can be determined by placing it behind a slightly wedged block of the reference crystal. Concerning Eq. 3.11 and 3.12 the relative reflectivity can be written as:

$$R_{s/d}(\omega) \triangleq \left|\frac{n_s(\omega) - n_m(\omega)}{n_s(\omega) + n_m(\omega)}\right|^2 = \frac{R^b(\omega)}{R^f(\omega)} \cdot \frac{R_m(\omega)}{(1 - R_m(\omega))^2} \quad , \tag{7.1}$$

where n_s and n_m the refractive index of the sample and the reference material and R_m is the reflectivity of the reference. R^b and R^f are the measured reflectance of the back surface (reference-sample) and the front surface (vacuum-reference). Together with the absolute reflectivity of the sample ($R_s(\omega) = \left|\frac{n_s(\omega)-1}{n_s(\omega)+1}\right|^2$) two independent optical quantities are experimentally obtained, i.e. each optical property is fully determined.

Chapter 8

Appendix B

8.1 Detailed analysis of the IR reflectivity measured under pressure

At first we still focus on ambient pressure studies but with the sample already embedded in the pressure cell, behind a diamond window. This results in a stack of complications, as we will see soon. We emphasized in 3.5 how important was the application of wedged diamond window in order to eliminate the interference effects. In spite of our efforts the reflectivity data are influenced by multiply reflections as it is obvious from Fig. 8.1. The distance corresponding to the period of the oscillation varied in the $20-40\mu$ m range for the experiments performed at different pressures. This means that the sample and the diamond do not strictly touch each other but there is a space between them. From now on, we have to accept, that we do not directly measure the reflectivity of the sample relative to the diamond as it would follow in ideal case from Eqs. 3.11, 3.12 but an extra frequency dependence of the back face scattering, $S^{extra}(\omega)$ comes into the picture which cannot be eliminated by the front face reference. Since we determined the complex dielectric function (or which is equal, the absolute refractive index, n) by the previous out of cell measurement, the reflectivity relative to the diamond, $R_{BaVS_3/d} = \left|\frac{n-2.43}{n+2.43}\right|^2$ can be easily calculated. Fig. 8.2 gives a comparison of the measured and calculated data.

The only way to eliminate $S^{extra}(\omega)$ and proceed in the evaluation is to take

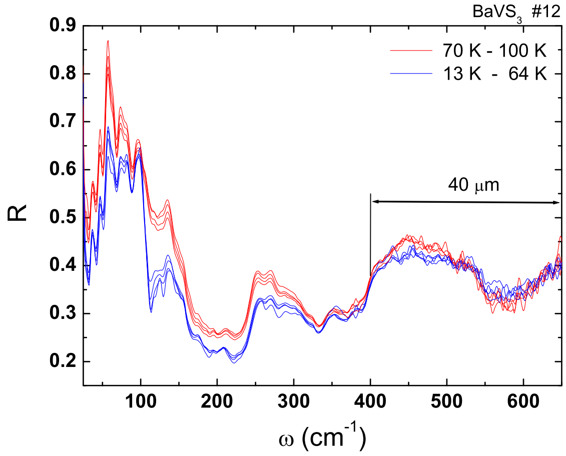

Figure 8.1: *FIR optical reflectivity of a* $BaVS_3$ *sample embedded in the pressure cell. The two stacks of red and blue curves are measured in the metallic and the insulating phase, respectively. Each graph is affected by an interference related oscillation.*

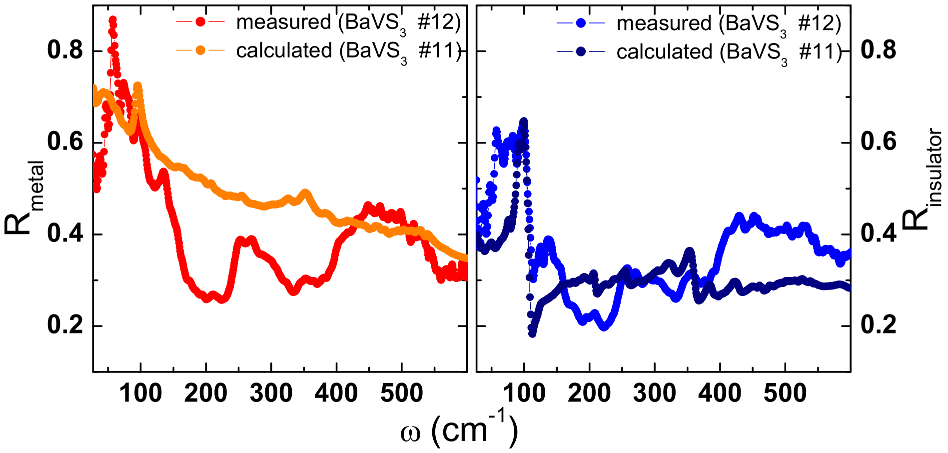

Figure 8.2: *The reflectivity relative to the diamond in ideal case and obtained by the measurement for both phases of the material.*

the ratio of the reflectivity measured in the metallic and insulating phase. In order to check whether it is enough to become free of any systematic error we can compare it to the ratio of the calculated values. Fig. 8.3 shows these two quantities together with the same ratio for the absolute (out cell measured) reflectivities. All the curves have the same shape but we can draw the conclusion that we loose a

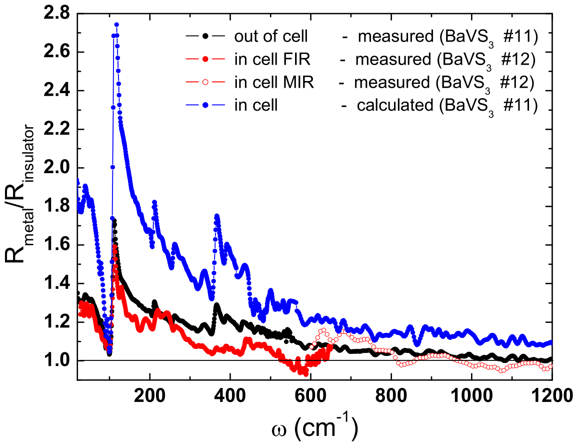

Figure 8.3: *The ratios of the metallic and insulating reflectivity in and out of the cell.*

part of the intensity in the measurement of the metallic phase. The possible reason is the following: in order to have a large enough sample we prepared a mosaic of characterized crystals. This mosaic was enclosed in a block of paraffin and finally polished to have a plain surface. As it is usual in case of mosaics, despite our efforts, we end up with free space among the small parts. The paraffin itself among the plaquettes does reflect some portion of the light, which gives a non-expected baseline for the measurement. Its reflectivity, since it is insulator, is smaller than that of the metallic BaVS$_3$, so we experience the decrease of the ratio. ($\frac{R_{metal}+R_{paraffin}}{R_{insulator}+R_{paraffin}}$ is necessarily smaller than $\frac{R_{metal}}{R_{insulator}}$.) Two more complications have to be mentioned here. First, with the application of pressure the sample can slightly move relative to the diamond, i.e. $S^{extra}(\omega)$ can change from pressure to pressure. Thus, the only information can be picked up from the experiment is the $R_{metal}/R_{insulator}$ ratio which is shown in Fig. 8.4 for each pressure investigated. The ambient pressure in cell ratio are scaled to the out cell ratio and this scaling factor was applied to the high-pressure data, too. Notice, that the in cell ratio differs from its calculated value and is rather identical with the out cell measured one so this step resulted no more than 10% correction of the data at any frequency.

On the other hand due to thermal expansion of the sample holder the sample can move perpendicular to the beam and its overlap with the light spot may vary. The estimation for the change in the sample position between room and low

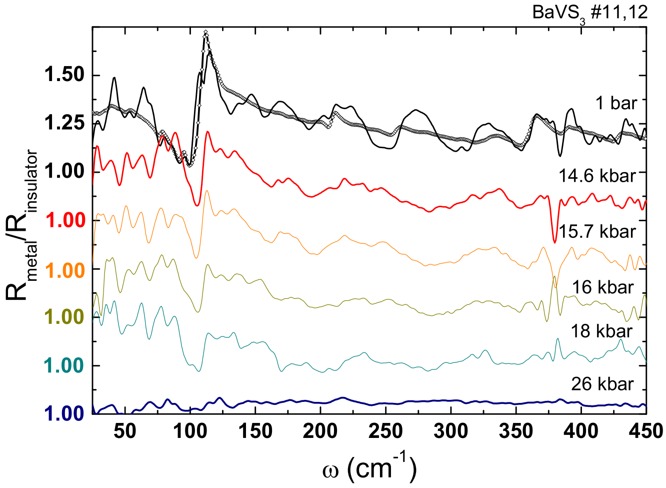

Figure 8.4: *The ratio of the metallic and insulating reflectivity for different pressures. At ambient pressure both out and in cell data are presented. For the experiment under* 26 *kbar the ratio of the data measured at* $T = 10$ *K and* 40 *K is shown.*

temperatures is 0.5 mm. This can be easily tested by the reproducibility of the front face reflection which should be otherwise temperature independent. After having a look at Fig. 8.5 we can conclude that the spectra are only reproducible below 100 K where the thermal expansion is negligible.

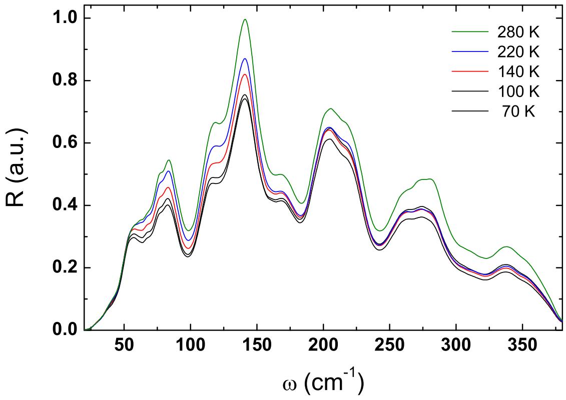

Figure 8.5: *The evolution of the intensity of the front face reflection with temperature.*

Thus, we are restricted to temperatures below 100 K and (due to the uncertainty of the detected reflectivity discussed above) we are able to observe only robust changes of the spectra like the opening of a gap. After all, the goal which we try to score is the determination of the gap as a function of pressure. As we have already seen the reflectivity of the metallic phase does not change more than 10% between room temperature and T_{MI} at any frequency and its shape is rather invariant without the appearance of sharp features. It can also be noticed in Fig. 8.1, where the transition is accompanied with a jump of the spectrum, but hardly anything happens in the $70 - 100\,\mathrm{K}$ range. This observation remains valid for the high-pressure data, too. On the other hand the dc conductivity increases also monotonously with increasing pressure, about 25% under $p = 20\,\mathrm{kbar}$. Based on these facts we take the following consideration: at any pressure the reflectivity of the metallic phase can be replaced with that of the ambient pressure metal and using the current value of the $R_{metal}/R_{insulator}$ ratio (shown in Fig. 8.4) the reflectivity of the insulator can be obtained for each pressure. The results are nicer than we would expect after so much trouble: the reflectivity of the insulator goes through a tendentious variation from pressure to pressure as it is visualized in Fig. 8.6.

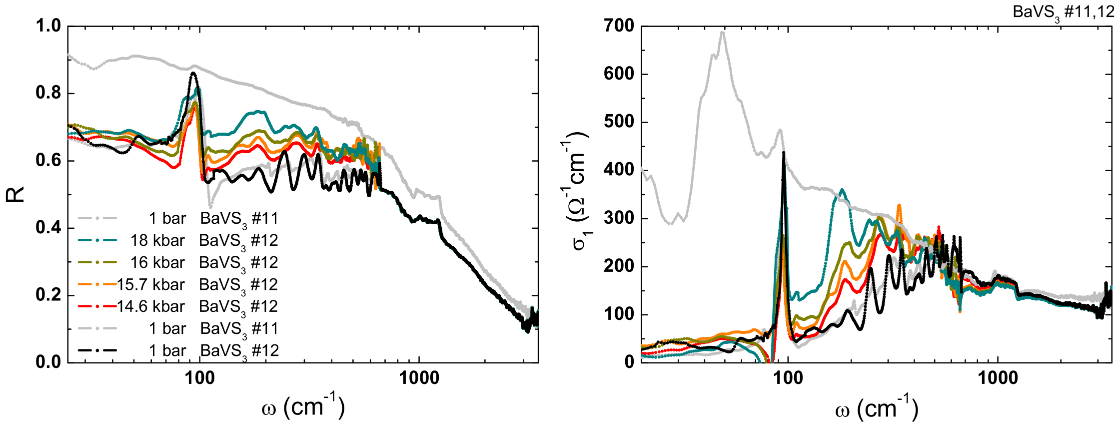

Figure 8.6: *Left panel: Reflectivity of* $BaVS_3$ *at five different pressures. The grey lines indicate the out cell results at* $T = 300$ *K and* 60 *K. Right panel: Conductivity of* $BaVS_3$ *at the same pressures.*

As it was mentioned we normalized the metallic reflectivity at each pressure to the ambient pressure out cell measured one to obtain the insulating reflectivity. For this purpose we used above the $T = 70\,\mathrm{K}$ data of the out cell experiment. However, we went through the same method using the $T = 300\,\mathrm{K}$ data. The test verified our consideration the sharp features (in our case the gap and the phonon at $100\,\mathrm{cm}^{-1}$) do not change, only the absolute value of the conductivity increased corresponding to the difference between the two reflectivities.

Chapter 9

Appendix C

9.1 Differential equations of $H-T$ phase boundary

The free energy is an analytic function of its variable on the whole $H-T$ plane except the phase boundary and continuous even on the phase boundary, i.e.:

$$\Delta f(H(s), T_{MI}(H(s))) \equiv 0 \quad , \tag{9.1}$$

where s is the length parameter of the transition line. The above equation is valid for phase transitions of any kind. For first order transitions this is the sole relation. Since $\Delta f \equiv 0$ on the phase boundary all of its s derivatives have to be zero along the curve. In the case of quadratic field dependence of the transition temperature ($T_{MI}(H) = T^0_{MI} - \alpha H^2$) we show it is equivalent to the vanishing of the field derivatives:

$$\Delta \frac{d^n f}{ds^n}(H(s), T_{MI}(H(s))) = 0 \Leftrightarrow \Delta \frac{d^n f}{dH^n}(H, T_{MI}(H)) = 0 \quad . \tag{9.2}$$

Parameter transformation for the above quadratic curve:

$$\begin{aligned} dT_{MI} &= -2\alpha H dH \\ ds &= \sqrt{dH^2 + dT^2_{MI}} = \sqrt{1 + 4\alpha^2 H^2} dH \end{aligned}$$

$$\frac{\partial H}{\partial s} = \frac{1}{\sqrt{1+4\alpha^2 H^2}} \neq 0 \ \forall s$$

The equivalence claimed in Eq. 9.2 can be easily checked for any n. For $n = 1$ it goes as:

$$0 = \Delta \left.\frac{df}{ds}\right|_{\gamma} = \Delta \left.\frac{df}{dH}\right|_{\gamma} \frac{\partial H}{\partial s} \ \mathit{and} \ \frac{\partial H}{\partial s} \neq 0 \ \forall s$$

$$\Rightarrow \Delta \left.\frac{df}{dH}\right|_{\gamma} = 0 \quad .$$

For $n = 2$:

$$0 = \Delta \left.\frac{d^2 f}{ds^2}\right|_{\gamma} = \Delta \left.\frac{d^2 f}{dH^2}\right|_{\gamma} \left(\frac{\partial H}{\partial s}\right)^2 + \Delta \left.\frac{df}{dH}\right|_{\gamma} \frac{\partial^2 H}{\partial s^2} \quad ,$$

$$\Delta \left.\frac{df}{dH}\right|_{\gamma} = 0 \ \mathit{and} \ \frac{\partial H}{\partial s} \neq 0 \ \forall s$$

$$\Rightarrow \Delta \left.\frac{d^2 f}{dH^2}\right|_{\gamma} = 0 \quad .$$

For any given n:

$$0 = \Delta \left.\frac{d^n f}{ds^n}\right|_{\gamma} = a_n \Delta \left.\frac{d^n f}{dH^n}\right|_{\gamma} + a_{n-1} \Delta \left.\frac{d^{n-1} f}{dH^{n-1}}\right|_{\gamma} + a_1 \Delta \left.\frac{df}{dH}\right|_{\gamma} \qquad ,$$

$$i < n : \ \Delta \left.\frac{d^i f}{dH^i}\right|_{\gamma} = 0 \ \mathit{and} \ \frac{\partial H}{\partial s} \neq 0 \ \forall s$$

$$\Rightarrow \Delta \left.\frac{d^n f}{dH^n}\right|_{\gamma} = 0.$$

In this notation a_i contains the product of $\frac{\partial^j H}{\partial s^j}$-type derivatives. These are finite in the present case. (The above argument remains valid in general when $\frac{\partial H}{\partial s} \neq 0 \ \forall s$ and $\frac{\partial^j H}{\partial s^j}$ is finite for $j < n$, i.e. in the case of regular parameter transformation.)

Detailed form of the phase boundary differential equations

From the continuity of the free energy in first order one can derive the well-known Clausius-Clapeyron equation:

$$\Delta \frac{\partial f}{\partial H}\bigg|_{\gamma} + \Delta \frac{\partial f}{\partial T}\bigg|_{\gamma} \frac{\partial T_{MI}}{\partial H} = 0 \quad . \tag{9.3}$$

In second order:

$$\Delta \frac{\partial^2 f}{\partial H^2}\bigg|_{\gamma} + 2\,\Delta \frac{\partial^2 f}{\partial T \partial H}\bigg|_{\gamma} \frac{\partial T_{MI}}{\partial H} + \Delta \frac{\partial^2 f}{\partial T^2}\bigg|_{\gamma} \left(\frac{\partial T_{MI}}{\partial H}\right)^2 + \Delta \frac{\partial f}{\partial T}\bigg|_{\gamma} \frac{\partial^2 T_{MI}}{\partial H^2} = 0 \quad . \tag{9.4}$$

In third order:

$$\begin{aligned} &\Delta \frac{\partial^3 f}{\partial H^3}\bigg|_{\gamma} + 3\,\Delta \frac{\partial^3 f}{\partial T \partial H^2}\bigg|_{\gamma} \frac{\partial T_{MI}}{\partial H} + 3\,\Delta \frac{\partial^2 f}{\partial T \partial H}\bigg|_{\gamma} \left(\frac{\partial^2 T_{MI}}{\partial H^2}\right)^2 + 3\,\Delta \frac{\partial^3 f}{\partial T^2 \partial H}\bigg|_{\gamma} \left(\frac{\partial T_{MI}}{\partial H}\right)^2 + \\ &\qquad 3\,\Delta \frac{\partial^2 f}{\partial T^2}\bigg|_{\gamma} \frac{\partial^2 T_{MI}}{\partial H^2} \frac{\partial T_{MI}}{\partial H} + \Delta \frac{\partial^3 f}{\partial T^3}\bigg|_{\gamma} \left(\frac{\partial T_{MI}}{\partial H}\right)^3 + \Delta \frac{\partial f}{\partial T}\bigg|_{\gamma} \frac{\partial^3 T_{MI}}{\partial H^3} = 0 \end{aligned} \tag{9.5}$$

Finally in 4^{th} order:

$$\begin{aligned} &\Delta \frac{\partial^4 f}{\partial H^4}\bigg|_{\gamma} + 4\,\Delta \frac{\partial^4 f}{\partial T \partial H^3}\bigg|_{\gamma} \frac{\partial T_{MI}}{\partial H} + 6\,\Delta \frac{\partial^4 f}{\partial T^2 \partial H^2}\bigg|_{\gamma} \left(\frac{\partial T_{MI}}{\partial H}\right)^2 + 6\,\Delta \frac{\partial^3 f}{\partial T \partial H^2}\bigg|_{\gamma} \frac{\partial^2 T_{MI}}{\partial H^2} + \\ &\quad 12\,\Delta \frac{\partial^3 f}{\partial^2 T \partial H}\bigg|_{\gamma} \frac{\partial^2 T_{MI}}{\partial H^2} \frac{\partial T_{MI}}{\partial H} + 4\,\Delta \frac{\partial^2 f}{\partial T \partial H}\bigg|_{\gamma} \frac{\partial^3 T_{MI}}{\partial H^3} + 4\,\Delta \frac{\partial^4 f}{\partial T^3 \partial H}\bigg|_{\gamma} \left(\frac{\partial T_{MI}}{\partial H}\right)^3 + \\ &\quad 6\,\Delta \frac{\partial^3 f}{\partial T^3}\bigg|_{\gamma} \frac{\partial^2 T_{MI}}{\partial H^2} \left(\frac{\partial T_{MI}}{\partial H}\right)^2 + 3\,\Delta \frac{\partial^2 f}{\partial T^2}\bigg|_{\gamma} \left(\frac{\partial^2 T_{MI}}{\partial H^2}\right)^2 + 4\,\Delta \frac{\partial^2 f}{\partial T^2}\bigg|_{\gamma} \frac{\partial^3 T_{MI}}{\partial H^3} \frac{\partial T_{MI}}{\partial H} + \\ &\qquad \Delta \frac{\partial^4 f}{\partial^4 T}\bigg|_{\gamma} \left(\frac{\partial T_{MI}}{\partial H}\right)^4 + \Delta \frac{\partial f}{\partial T}\bigg|_{\gamma} \frac{\partial^4 T_{MI}}{\partial H^4} = 0 \end{aligned} \tag{9.6}$$

Eqs. 9.3-9.6 relate discontinuities of different thermodynamical properties to each other through the shape of the phase boundary. (Since they are valid for any kind of phase transition with continuous transition line they allow the order of the transition to change along the phase boundary. In the case of second or higher order phase transitions one can derive similar equations from the continuity of the corresponding thermodynamical properties (entropy, magnetization, etc.) which further specify the relations between the discontinuities.)

Quadratic phase boundary

From now on the usual notation of the partial derivatives of the free energy is used. The ratio of their jumps will be determined at $H = 0$ point of the phase boundary ($\frac{\Delta T_{MI}(H)}{T^0_{MI}} = -\beta H^2$).

$$\Delta M(0, T^0_{MI}) = 0 \tag{9.7}$$

$$\Delta\chi^{(1)}(0, T^0_{MI}) - 2\beta T^0_{MI}\Delta S(0, T^0_{MI}) = 0 \tag{9.8}$$

$$\Delta\frac{\partial\chi^{(1)}}{\partial H}(0, T^0_{MI}) - 6\beta T^0_{MI}\Delta\frac{\partial M}{\partial T}(0, T^0_{MI}) = 0 \tag{9.9}$$

$$\Delta\chi^{(3)}(0, T^0_{MI}) - 12\beta T^0_{MI}\Delta\frac{\partial\chi^{(1)}}{\partial T}(0, T^0_{MI}) + 12\beta^2 T^0_{MI}\Delta C(0, T^0_{MI}) = 0 \tag{9.10}$$

Due to the quadratic shape of $T_{MI}(H)$ different order derivatives of the free energy simultaneously appear in Eqs. 9.8-9.10.

If the system shows second order phase transition in an extended part of the $H - T$ plane two more thermodynamical quantities are continuous at the phase boundary thus the relations between the discontinuities become further determined, i.e.:

$$\Delta S(H, T_{MI}(H)) \equiv 0 \tag{9.11}$$

$$\Delta M(H, T_{MI}(H)) \equiv 0 \tag{9.12}$$

Following the same treatment than for the free energy one obtains from Eq. 9.11 up to third order:

$$\Delta\frac{\partial M}{\partial T}(0, T^0_{MI}) = 0 \tag{9.13}$$

$$\Delta\frac{\partial\chi^{(1)}}{\partial T}(0, T^0_{MI}) - 2\beta\Delta C(0, T^0_{MI}) = 0 \tag{9.14}$$

$$-6\beta T_{MI}^0 \Delta \frac{\partial^2 M}{\partial T^2}(0, T_{MI}^0) + \Delta \frac{\partial^2 \chi}{\partial T \partial H}(0, T_{MI}^0) = 0 \tag{9.15}$$

And from the continuity of the magnetization:

$$\Delta \chi^{(1)}(0, T_{MI}^0) = 0 \tag{9.16}$$

$$\Delta \frac{\partial \chi^{(1)}}{\partial H}(0, T_{MI}^0) - 2\beta T_{MI}^0 \Delta \frac{\partial M}{\partial T}(0, T_{MI}^0) = 0 \tag{9.17}$$

$$-6\beta T_{MI}^0 \Delta \frac{\partial \chi^{(1)}}{\partial T}(0, T_{MI}^0) + \Delta \chi^{(3)}(0, T_{MI}^0) = 0 \tag{9.18}$$

Summary

The higher order analysis of the phase boundary can help to identify the nature of transitions when only higher order derivatives of the free energy (higher than the expected order of the transition) and the shape of the phase boundary are determined experimentally. This method is appropriate when the first derivative of the boundary line is zero thus the Ehrenfest-like-relations are zero statements. In this case - as we noticed - the related quantities are not of the same order.

References

[1] R. A. Gardner, M. Vlasse, and A. Wold, Acta Crystallogr., Sect. B: Struct. Crystallogr. Cryst. Chem. **B25**, 781 (1969)

[2] M. Ghedira, M. Anne, J. Chenavas, M. Marezio, and F. Sayetat, J. Phys. C **19**, 6489 (1986)

[3] F. Sayetat, M. Ghedira, J. Chenavas, and M. Marezio, J. Phys. C **15**, 1627 (1982)

[4] L. F. Mattheis, Solid State Commun. **93**, 791 (1995)

[5] R. Itti, K. Matsuura, T. Itoh, K. Ikeda, H.Yamauchi, N. Koshizuka, and S. Tanaka, Phys. Rev. B **44**, 2306 (1991)

[6] O. Massenet, R. Buder, J. J. Since, C. Schlenker, J. Mercier, J. Kelber and D. G. Stucky, Mat. Res. Bul. **B13**, 187 (1978)

[7] H. Nishihara and M. Takano, J. Phys. Soc. Jpn. **50**, 426 (1981)

[8] H. Nakamura, H. Imai, and M. Shiga, Phys. Rev. Lett. **79**, 3779 (1997)

[9] A. Heidemann and M. Takano, Phys. Stat. Sol. (b) **100**, 343 (1980)

[10] M. Nakamura, A. Sekiyama, H. Namatame, A. Fujimori, H. Yoshihara, T. Ohtani, A. Misu, and M. Takano, Phys. Rev. B, **49**, 16191 (1994)

[11] T. Graf, D. Mandrus, J. M. Lawrence, J. D. Thompson, P. Canfield, Phys. Rev. B **51**, 2037 (1995)

[12] H. C. Montgomery, J. Appl. Phys. **42**, 2971 (1971)

[13] R. D. Barnard, Thermoelectricity in metals and alloys, (1972) Taylor Francis Ltd.

[14] F. J. Blatt, P. A. Schroeder, C. L. Folies and D. Greig, Thermoelectric power of metals, Plenum Press, New York London

[15] H. Nakamura, T. Yamasaki, S. Giri, H. Imai, M. Shiga, K. Kojima, M. Nishi, K. Kakurai, and N. Metoki, J. Phys. Soc. Jpn. **69**, 2763 (2000)

[16] L. N. Bulaevskii, A. I. Buzdin, and D. I. Khomskii, Solid State Commun. **27**, 5 (1978)

[17] M. C. Cross, Phys. Rev. B **20**, 4606 (1979)

[18] J. A. Northby, H. A. Groenendijk, L. J. de Jongh, J. C. Bonner, I. S. Jacobs, and L. V. Interrate, Phys. Rev. B **25**, 3215 (1982)

[19] M. Hase, I. Terasaki, and K. Uchinokura, Phys. Rev. Lett. **70**, 3651 (1993)

[20] H. Imai, H. Wada, and M. Shiga, J. Phys. Soc. Jpn. **65**, 3460 (1996)

[21] G. Mihály, I. Kézsmárki, F. Zámborszky, M. Miljak, K. Penc, P. Fazekas, H. Berger, and L. Forró, Phys. Rev. B **61**, R7831 (2000)

[22] C. H. Booth, E. Figureoa, J. M. Lawrence, M. F. Hundley, and J. D. Thompson, Phys. Rev. B **60**, 14852 (1999)

[23] T. Inami, K. Ohwadw, K. Imura, M. Watanabe, Y. Noda, H. Nakamura, T. Yamasaki, M. Shiga, N. Ikeda, and Y. Murakami, Phys. Rev. B **66**, 73108 (2002)

[24] P. Fazekas, Lecture notes on electron correlation and magnetism, Series in Modern Condensed Matter Physics: Vol. 5, World Scientific (1999)

[25] J. Zeman, G. Martinez, P. H. M. van Loosdrecht, G. Dhalenne, and A. Revcolevschi, Phys. Rev. Lett. **83**, 2648 (1999)

[26] S. E. Brown, W. G. Clark, B. Alavi, D. Hall, M. J. Naughton, D. J. Tantillo, and C. A. Merlic, Phys. Rev. B. **60**, 6270 (1999)

[27] M. Shiga, H. Imai, H. Mitamura, and T. Goto, Physica B **294**, 149 (2001)

[28] P. M. Chaikin and G. Beni, Phys. Rev. B **13**, 647 (1976)

[29] E. Abrahams, G. Kotliar, Science **274**, 1853 (1996)

[30] A. Hussmann, D. S. Jin, Y. V. Zastavker, T. F. Rosenbaum, X. Yao, and J. M. Honig, Science **274**, 1874 (1996)

[31] D. Bitko, T. F. Rosenbaum, and G. Aeppli, Phys. Rev. Lett. **77**, 940 (1996)

[32] N. D. Mathur, F. M. Grosche, S. R. Julian, I. R. Walker, D. M. Freye, R. K. W. Haselwimmer, and G. G. Lonzarich, Nature **394**, 39 (1998)

[33] F. Steiglich, P. Gegenwart, C. Geibel, P. Hinze, M. Lang, C. Langhammer, G. Sparn, and O. Trovarelli, Physica B **280**, 349 (2000)

[34] P. Gegenwart, J. Custers, K. Neumaier, T. Tayama, K. Tenya, O. Trovarelli, and F. Steglich, Phys. Rev. Lett. **89**, 56402 (2002)

[35] L. Klein, L. Antognazza, T. H. Gabrielle, M. R. Beasley, and A. Kapitulnik, Phys. Rev. B **60**, 1448 (1999)

[36] C. Pfleiderer, S. R. Julian, G. G. Lonzarich, Nature **414**, 427 (2001)

[37] to be published

[38] to be published

[39] K. Matsuura, T. Wada, T. Nakazimo, H. Yamauchi, and S. Tanaka, Phys. Rev. B **43**, 13118 (1991)